이학박사학위논문

Hydrogen Bond Network Measurement of Confined Water Using Tip-enhanced Raman Spectroscopy

팁-증강 라만 효과를 이용한 나노컨파인드 물의 수소결합 구조 측정

2023 년 2 월

서울대학교 대학원

물리천문학부

황 종 근

Hydrogen Bond Network Measurement of Confined Water Using Tip-enhanced Raman Spectroscopy

팁-증강 라만 효과를 이용한 나노컨파인드 물의 수소결합 구조 측정

지도교수 제 원 호

이 논문을 이학박사 학위논문으로 제출함

2023 년 1 월

서울대학교 대학원

물리천문학부 물리학전공

황 종 근

황종근의 이학박사 학위논문을 인준함

2023 년 1 월

위 원 장	홍승훈	(인)
부위원장	제원호	(인)
위 원	박건식	(인)
위 원	백용주	(인)
위 원	손창윤	(인)

Abstract

Jonggeun Hwang

Department of Physics and Astronomy

The Graduate School

Seoul National University

Confinement change interfacial energy and entropy of molecule within by reducing degrees of freedom. The properties of confined water are also changed like any other molecules. For example, macroscopic properties of confined water such as elastic modulus, friction coefficient, viscosity, and dielectric constant are changed with respect to bulk water. The origin of the peculiar properties of confined water has been thought to be closely related to the hydrogen bond (HB) network since the unique properties of water are mainly attributed to the HB network. Many simulation studies and spectroscopy study report that nanoscale confined water has a different HB network from the bulk phase. However, experimental demonstration of the HB network of confined water found in simulation is not achieved yet. In the spectroscopy study, the fine control of the confinement is difficult and demonstration of the correlation of the HB network with the macroscopic properties is not easy. Meanwhile, experiments to measure changes in the mechanical properties of confined water were mainly conducted

using atomic force microscopy (AFM) or a surface force apparatus (SFA), but these force-measuring instruments could not observe the HB network.

To simultaneously measure both the HB network and the mechanical property of confined water, we establish tip-enhanced Raman spectroscopy (TERS) by combining the quartz tuning forks (QTF) based AFM and the confocal Raman spectroscopy. TERS is the near-field optical technique that realizes to overcome optical diffraction limits by the enhanced local field at the apex of the metallic tip. The enhancement factor (EF) of TERS, indicating the amount of signal magnification compared to micro-Raman, is achieved up to 10^6 in ambient conditions. Thus, employment of the TERS is essential to investigate a very small amount of water molecules because of the small scattering cross-section of a water molecule. we establish stable nano-confined water by creating a capillary condensed nano-meniscus between the tip and the substrate. As a result, confined water at weak confinement behaves like supercooled water, while confined water at strong confinement has the same HB structure as ice-VII, a high-pressure ice phase at room temperature. We also observe the correlation between the Raman signal and the mechanical relaxation time of confined water, which strongly indicates that the enhanced solidity of confined water near the substrate is caused by the increased portion of ice-VII within confined water.

Water is the most important liquid on earth that is closely involved in many atmospheric processes and biochemical reactions. Furthermore, confined water plays a major role in initial cloud formation or DNA-protein interaction rather than bulk water. In this study, we investigate the physical and chemical prop-

erties of confined water. In particular, we focused on the HB network because it gives the unique features of water. Our result will help to understand the origin of the peculiar properties of confined water such as sluggish behaviour and will provide experimental evidence of the unique HB structure under confinement.

Keywords: Tip-enhanced Raman Spectroscopy, Raman Spectroscopy, Atomic Force Microscopy, Water, Confined Water, Hydrogen Bond Network, Ice-VII, Confinement, Phase Transition

Student Number: 2014-21349

Contents

Chapter 1

Introduction

1.1 Motivation

For low-dimensional water in confined geometry, its entropy and interfacial energy are changed due to the lowered degrees of freedom of water molecules. It has been expected and examined that the resulting change of the physical, chemical, and biological interactions can be associated with the molecular structural change of water [1–3].

For example, the confined water within a hydrophobic one-dimensional channel such as carbon nanotubes (CNTs) has a very different friction nature and transport properties [4,5] with respect to its bulk counterparts. The absorption spectrum of water within single wall carbon nanotubes (SWCNTs) with a diameter of less than 2 nm is significantly different from that of bulk water [6]. The proportion in the absorption spectrum of water without hydrogen bonding

(free-OH) remains high regardless of the CNT diameter, and this is because the carbon molecule in CNT does not have a hydrogen bonding with water. The reason for the ultrafast transport property of confined water within CNTs may be closely related to the peculiar hydrogen bonding network of water.

In two-dimensional confinement, many physical and chemical properties of confined water are also changed as in one-dimensional confinement. It has been reported that the dielectric constant of water confined between hexagonal boron nitride (hBN) and graphene is 40 times smaller than that of bulk water [7]. The existence of the electrical dead water layer was predicted by molecular dynamics simulations [8, 9]. Moreover, the mechanical properties of water are also changed in the confinement. The viscosity of confined water at the mica surface increased significantly [10, 11], and similar changes are observed at the graphene surface [12]. It is reported that the water trapped between proteins or DNAs also shows sluggish dynamics [13] but the role of confined sluggish water in the biological process is still needed to understand.

In addition, the mapping of the Raman signal of a diameter of a few hundred micrometer droplets using surface-enhanced Raman spectroscopy (SERS) reveals pH at the center of the droplet is about 10.6 [14], which is higher than the bulk water pH of 7. And it has been reported that the self-dissociation process of water is enhanced by confinement [15] and the intracellular biological water has slightly lower pH than bulk water [16, 17]. However, the water pH in nanoconfinement is very poorly understood.

Evidence of the ordered structure in confined water has been reported in the previous nano-confined water studies using atomic force microscopy (AFM)

[18–20] and surface force apparatus (SFA) [21]; the molecular layered structure of water and the increased mechanical relaxation time with respect to the bulk water indicating the enhanced solidity. However, there is an intrinsic limitation on the force-measurement methods in identifying the exact structure of water because force measurement alone cannot address the HB structure which is the critical feature to determine the ordered nature of water under confinement.

Meanwhile, in the most recent first-principle MD simulations, water confined within nanoslits is expected to exhibit a new ice phase of superionic phase [22] and bilayer ice-VII [23] at room temperature, but not the hexagonal ice structure, which has not been investigated via quantitative experiment yet.

It is natural to think that the hydrogen bond network of confined water may be closely related to these unique properties of confined water since the most peculiar properties of bulk water such as density, boiling point, and surface tension originated from the hydrogen bonding. However, it is extremely challenging to investigate the molecular structure of small confined water. This is because such a study requires quantitative confinement control in the degree of confinement and the nature of spectroscopic properties of water molecules such as the small Raman cross-section and the large bandwidth of the OH-stretching band of water. Many *in situ* spectroscopic methods for confined water have been reported such as the surface-enhanced Raman spectroscopy [24, 25], sum-frequency generation spectroscopy [26], X-ray spectroscopy [27], and ensemble measurement [6,28]. However, the spectroscopic techniques alone are insufficient to obtain a holistic understanding of the structure-property relations for water under confinement. To simultaneously obtain the structural information and the

mechanical properties of confined water, we establish tip-enhanced Raman spectroscopy (TERS) which combines atomic force microscopy with confocal Raman spectroscopy. TERS is a near-field optical platform that probes the confinement-dependent molecular structure of small quantities of molecules [29, 30], which is much more sensitive than the traditional micro-Raman methods.

1.2 Outline of this work

This thesis proceeds as follows. The basic principle of the Raman scattering is explained in Chapter 2. Subsequently, Surface-enhanced Raman spectroscopy (SERS) and Tip-enhanced Raman spectroscopy (TERS) are introduced including their enhancement mechanisms and the degree of enhancement. Chapter 3 gives a description of the experimental setup. A detailed description of the quartz tuning forks (QTF) based TERS setup, electrical circuits, calibration methods, tip fabrication methods, and sample preparation methods are given in this Chapter since we built our experimental setup from the scratch. In Chapter 4, the experimental procedure and results are described. To confirm that the measured Raman signal represents the entire nano-meniscus, the profile of the water meniscus is theoretically calculated by solving Young-Laplace equation [31] and it is compared with 'hotspot' size which is numerically calculated by finite-difference time-domain (FDTD) simulations. And then the HB network of the confined water is presented with a measured Raman signal and the corresponding mechanical response data of the confined water at room temperature. After the peak assignment of the measured Raman signal with the

help of the spectral uniqueness and the meniscus model, the phase behavior of confined water depends on confinement is studied. Finally, this thesis concludes with a summary in Chapter 5.

Chapter 2

Theoretical background

2.1 Capillary condensation

Capillary condensation is the first-order phase transition into a liquid from gas in confined geometry. Condensation of water is especially important because it is involved in many processes and it usually occurs in porous media and granular media and it strongly changes properties such as friction, adhesion, and lubrication [32–34]. For water, when two hydrophilic surfaces become closer to less than a few nanometers, a confined water capillary is formed due to the strong Van der Waals interactions between molecules inside confined geometry.

This phenomenon is explained by the Kelvin equation which expresses the vapor pressure difference across the curved interface. And the shape of the capillary is described by the Young-Laplace equation which expresses the pressure difference across the curved interface.

In our experiment, this phenomenon is used to create nano confined water. At given relative humidity, water nano meniscus is formed by capillary condensation between the tip and the hydrophilic substrate (e.g. mica) when the tip-mica distance is reached the critical distance d_c.

2.1.1 Kelvin equation

The stability of condensed liquid is expressed following the Kelvin equation.

$$\ln \frac{p_e}{p_0} = \frac{\sigma v_l}{k_{\mathrm{B}} T R} \tag{2.1}$$

Here, p_e is the equilibrium vapor pressure, p_0 is the saturation vapor pressure, σ is a surface tension of a liquid, v_l is a molar volume of a liquid, k_{B} is the Boltzmann constant, T is temperature, and R is a mean radius of curvature of a capillary. The mean radius of curvature is defined as $1/R = 1/r_1 + 1/r_2$, where r_1 and r_2 are the two principal radii of curvature of the capillary. For the spherical droplet, $r_1 = r_2 = r > 0$, so $1/R = 2/r$. For the meniscus, $r_1 < 0$, $r_2 > 0$, and generally $|r_1| < |r_2|$, so the mean radius of curvature $1/R$ is negative.

2.1.2 Young-Laplace equation

The Young-Laplace equation describes the pressure difference at a liquid-air interface with curvature. At a concave surface, the pressure is higher than the atmospheric pressure, and at a convex surface, the pressure is lower than the atmospheric pressure (figure 2.1).

$$\Delta P = \gamma \left(\frac{1}{R_1} + \frac{1}{R_2} \right) \tag{2.2}$$

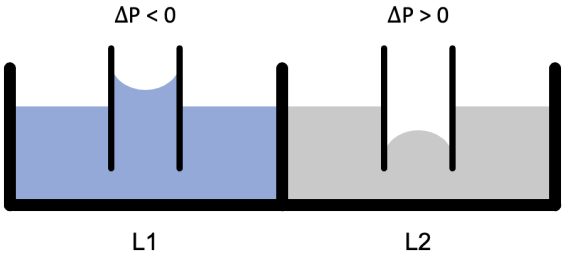

Figure 2.1: Pressure difference at the curved liquid-air interface. (left) liquid with negative pressure difference (e.g. water). (right) liquid with positive pressure difference (e.g. mercury).

where ΔP is the pressure difference across the liquid-gas interface which is called Laplace pressure, γ is an interfacial tension, and R_1, R_2 is a principal radii of curvature of the interface.

2.2 Atomic force microscopy

Atomic force microscopy (AFM) is developed in 1986 [35], and is widely used to study surfaces in chemistry, biology, and material science as an imaging and analyzing tool [36–38]. AFM is one of the scanning probe microscopy using atomic force to analyze the surface using a probe with a tip diameter of several nanometers to tens of nanometers. Therefore, it is possible to observe beyond the optical diffraction limit $\sim \lambda/2$ of about hundreds of nanometers which is the typical resolution limit of optical instruments with visible light. It is also possible to measure the physical properties of the surface from tip-sample interaction. Depending on what kind of tip-sample interaction is used, various applications are available such as Kelvin probe microscopy [39, 40], scanning

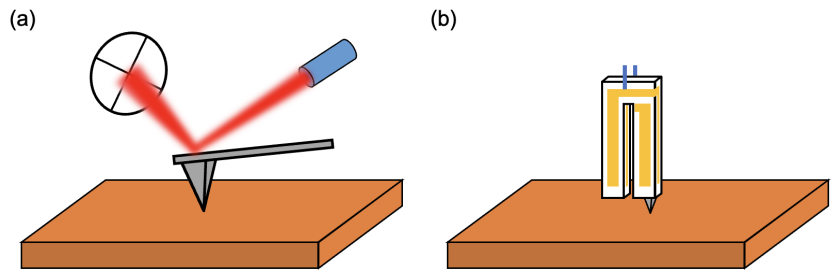

Figure 2.2: Two types of AFM. (a) AFM with cantilever probe. (b) AFM with QTF operating in shear mode.

capacitance microscopy [7,41], conductive probe AFM [42,43], electrostatic force microscopy [44], magnetic force microscopy [45,46], and lateral force microscopy [47].

There are two types of AFM probes, cantilever and quartz tuning fork (QTF), and their operating mechanism are largely different. (figure 2.2) The cantilever probe is widely used for most commercial AFM because of its expandability of the cantilever probe. The cantilever has a length of several hundred micrometers and a thickness of several micrometers, and its stiffness lies between $0.01 \sim 100$ N/m. The cantilever with suitable stiffness has to be chosen depending on what sample to be measured. Softer cantilever should be used for biological samples, especially in contact mode [48]. The tip-sample interaction is measured through the bending of the cantilever, and it can be measured using a reflected laser by the reflection side of the cantilever. The laser is aligned to the center of the quadrant photodiode, and the position of the beam on the photodiode is deviated depending on the direction and the magnitude of the

force exerted on the probe.

QTF is a force sensor with a resonance frequency near 32.7 kHz and a stiffness of about $10^3 \sim 10^4$ N/m. It also has a high-quality factor of $10^3 \sim 10^6$. When QTF oscillates, periodic charge difference across the prong of the QTF occurs since QTF is made of piezoelectric materials. The oscillating charge difference can be detected as an electrical signal through the electrodes attached on both sides of the two prongs, it is unnecessary to use an optical system to detect the deflection signal of the sensor [49]. QTF can measure force in both the normal and the shear direction according to the vibration direction. However, the two prongs of the QTF are coupled, and the effect of stray capacitance should be removed to quantitatively measure force especially when the QTF is electrically driven [50]. The effect of stray capacitance can be removed by using an equivalent circuit of a quartz crystal resonator [51] or by mechanically driving QTF to avoid the effect of stray capacitance [48, 52]. Another modified QTF probe is qPlus sensor [53]. In qPlus sensor, one of the prongs is fixed to hard support and vibrates another prong to use QTF as if using a cantilever made of quartz.

2.2.1 Operating modes of AFM

There are two operating modes for AFM, static mode and dynamic mode. The static mode is often referred to as the contact mode. A probe with low stiffness (< 1 N/m) is used for static mode since the cantilever deformation should be greater than the sample deformation. The tip-sample interaction is measured through the degree of cantilever bending when the probe approaches

the substrate. The interpretations of tip-sample interaction are quite simple in the static mode because the deflection of the cantilever beam and tip-sample forces are in a linear relationship while it is vulnerable to external noise [52].

In addition, in static mode, the elasticity of the soft sample such as a cell or a polymer can be analyzed using contact mechanics that predict the contact force depending on the sample type [36]. The basic contact models commonly used in contact mechanics are Hertz [54], Derjaguin-Muller-Toporov (DMT) [55], and Johnson-Kendall-Roberts (JKR) [56] models. The sample is assumed to be purely elastic in these models. No surface forces such as adhesion and long-range force are not considered in the Hertz model, whereas surface forces are considered in the other two models. The DMT model is valid for stiff materials and when the sample exhibits weak adhesions, and the JKR model is valid for materials with stronger adhesions.

In dynamic mode, the probe vibrates near its resonance frequency. AFM is controlled by using the response of the probe according to the tip-sample interaction. The dynamic mode is often referred to as the non-contact mode. In general, tip-sample interactions are attractive over long-range and repulsive when close to the atom. To control the response of the probe according to these interactions, the Amplitude-modulation (AM) operation [57, 58] or the Frequency-modulation (FM) operation [59] can be achieved.

In AM-AFM, both driving frequency and driving amplitude are fixed, and most commercial AFMs are operated in AM mode as well. The driving frequency is usually slightly lower than its resonance frequency so that the probe can react monotonically to the tip-sample interaction. The amplitude and phase

signal of the probe, which changes with tip-sample interaction as a response of the probe, is used to control AM-AFM. However, the response of the probe according to the tip-sample interaction is delayed by the probe response time, which time interval needed to transit from one state to another. The time scale of response time is $\tau \sim 2Q/f_0$ [48], and for QTF with a high quality factor of $10^3 \sim 10^4$ and a resonance frequency of 32.7kHz has a large response time of order of several hundred milliseconds. It limits the vacuum application of AM-AFM with a high quality factor probe [60]. Meanwhile, for the ultrafast imaging with AM-AFM at ambient conditions, the probes which have a quality factor of about 1.5 and a resonance frequency of 100 kHz or more are used, so that the response time is less than several tens of μs [61, 62].

The operation mechanism of FM-AFM is much more complicated than AM-AFM. The phase-locked-loop (PLL) circuit is used to fix the amplitude and keep the probe always operating at the resonance frequency [48,59,60]. The frequency shift from the resonance frequency and the amplitude attenuation compared to the free amplitude are measured and used to control AFM in FM operation mode. The frequency shift corresponds to non-dissipative interaction and the amplitude attenuation corresponds to dissipative interaction. In addition, since the frequency shift caused by tip-sample interaction is continuously tracked in the feedback loop including the PLL circuit, FM-AFM is free from time delay problems between each data point.

2.3 Raman spectroscopy

Raman spectroscopy has been widely used in physics, chemistry, and biology for about 100 years since its discovery by C. V. Raman and K. S. Krishnan in 1928 [63]. Most of the light interacting with matter is elastically scattered which is referred to as Rayleigh scattering. Meanwhile, inelastic scattering which is referred to as Raman scattering is a rare event. The energy transferred through Raman scattering excites the vibrational energy state of the molecule, which can be categorized into Stokes Raman scattering and anti-Stokes Raman scattering. Stokes Raman scattering is a process in which molecules are excited from the ground state and fall into the excited state. In this process, the molecule absorbs energy and emits red-shifted light with a wavelength longer than the incident light. On the other hand, in anti-Stokes Raman scattering, molecules in the excited state are excited by incident light and fall to the ground state. At this time, blue-shifted light with a wavelength shorter than the incident light is emitted. Although the difference in wavelength of light emitted in the two processes is the same, the intensity of the Stokes Raman is much more than the intensity of the anti-Stokes Raman because the ratio of the number of molecules in the energy states follows the Boltzmann distribution, so the number of molecules in the ground state is much more than the number of molecules in the excited states. Also, by observing the ratio of Stokes Raman and anti-Stokes Raman intensities, the temperature of the system can be deduced.

2.3.1 Classical picture of Raman scattering

The Raman scattering process can be understood classically from the classical perspective of light-matter interaction. the electrons of a molecule are perturbed by the external electric field, which induces a dipole moment. In experiments, the molecules are usually excited by the laser. Unlike a quantum mechanical interpretation in which the bound electron has quantized energy states, the molecule has a continuous induced dipole moment $\vec{p}$ which has a proportionality factor α between the external electric field and the induced dipole moment. Under the linear relation assumption, $\vec{p}$ can be expressed as follows.

$$\vec{p} = \alpha \vec{E} \tag{2.3}$$

When the external electric field has the incident intensity E_0 and is the monochromatic plane wave with frequency ω_0, the induced dipole moment is

$$\vec{p} = \alpha \vec{E_0} \cos(\omega_0 t) \tag{2.4}$$

Here α is the molecular polarizability tensor. Changing the nuclear positions will modify the polarizability as the electrons are rearranged to minimize the energy of the system. The nuclear coordinate dependence on α makes it also depends on the molecular vibrational modes.

Now let's consider the system with one molecule which is free to vibrate but not allowed to rotate. So, their nuclei can vibrate about their equilibrium positions. The polarizability tensor can be expanded in a Taylor series with

respect to the normal coordinates of vibration.

$$\alpha_{\rho\sigma} = (\alpha_{\rho\sigma})_0 + \sum_k \left(\frac{\partial \alpha_{\rho\sigma}}{\partial Q_k}\right)_0 Q_k + \frac{1}{2}\sum_{k,l}\left(\frac{\partial^2 \alpha_{\rho\sigma}}{\partial Q_k \partial Q_l}\right)_0 Q_k Q_l + \ldots \qquad (2.5)$$

where $(\alpha_{\rho\sigma})_0$ is the equilibrium value of $\alpha_{\rho\sigma}$, Q_k, Q_l are normal coordinates of vibration with regard to the molecular vibrational frequencies ω_K, ω_l. The equation (2.5) can be expressed in a simple form by considering one normal mode of vibration.

$$(\alpha_{\rho\sigma})_k = (\alpha_{\rho\sigma})_0 + \left(\frac{\partial \alpha_{\rho\sigma}}{\partial Q_k}\right)_0 Q_k + \ldots \qquad (2.6)$$

By assuming the simple harmonic motion for the vibration, the Q_k is given by

$$Q_k = Q_{k0}\cos(\omega_k t + \delta_k) \qquad (2.7)$$

where Q_{k0} is the amplitude of the vibrational motion and δ_k is a phase. then,

$$(\alpha_{\rho\sigma})_k = (\alpha_{\rho\sigma})_0 + \left(\frac{\partial \alpha_{\rho\sigma}}{\partial Q_k}\right)_0 Q_{k0}\cos(\omega_k t + \delta_k) + \ldots \qquad (2.8)$$

Combining equation (2.8) with equation (2.4), the time dependence of the induced dipole moment is given by,

$$\vec{p} = (\alpha_{\rho\sigma})_0 \vec{E_0}\cos(\omega_0 t) + \left(\frac{\partial \alpha_{\rho\sigma}}{\partial Q_k}\right)_0 Q_{k0}\cos(\omega_k t + \delta_k)\vec{E_0}\cos(\omega_0 t) + \ldots \qquad (2.9)$$

Using the trigonometric identity,

$$\begin{aligned}\vec{p} \cong (\alpha_{\rho\sigma})_0 \vec{E_0}\cos(\omega_0 t) &+ \frac{1}{2}\left(\frac{\partial \alpha_{\rho\sigma}}{\partial Q_k}\right)_0 Q_{k0}\vec{E_0}\cos[(\omega_0 - \omega_k)t - \delta_k] \\ &+ \frac{1}{2}\left(\frac{\partial \alpha_{\rho\sigma}}{\partial Q_k}\right)_0 Q_{k0}\vec{E_0}\cos[(\omega_0 + \omega_k)t + \delta_k] \qquad (2.10)\end{aligned}$$

or simply,

$$\begin{aligned}\vec{p} \cong & \vec{p}_{\text{Rayleigh}} \cos(\omega_0 t) \\ & + \vec{p}_{\text{Raman}} \cos[(\omega_0 - \omega_k)t - \delta_k] \\ & + \vec{p}_{\text{Raman}} \cos[(\omega_0 + \omega_k)t + \delta_k]\end{aligned} \tag{2.11}$$

with

$$\vec{p}_{\text{Rayleigh}} = (\alpha_{\rho\sigma})_0 \vec{E}_0 \tag{2.12}$$

$$\vec{p}_{\text{Raman}} = \frac{1}{2}\left(\frac{\partial \alpha_{\rho\sigma}}{\partial Q_k}\right)_0 Q_{k0} \vec{E}_0 \tag{2.13}$$

Here, $\vec{p}_{\text{Rayleigh}}$ is the zeroth-order induced electric dipole moment, and $\vec{p}_{\text{Raman}}$ is the first-order induced electric dipole moment. Therefore, in the equation (2.11), the first term oscillates at the same frequency as the external field, and the scattered light from the induced dipole moment also oscillates at that frequency, that is the elastic Rayleigh scattering term. The Rayleigh scattered light is an elastically scattered light and contains no information about the vibrational modes of the molecule. The scattered light from the induced dipole moment of the second term and the third term are inelastically scattered light and contain the molecular vibrational modes information. The scattered light by the induced dipole moment at the frequency of $\omega_0 - \omega_k$ is red-shifted compared to the external field, which is Stokes Raman scattered light. Similarly, a scattered light at the frequency of $\omega_0 + \omega_k$ is blue-shifted with respect to the external field which is an anti-Stokes Raman scattered light.

2.3.2 Intensity of Raman scattering

If a molecule excited by an external field is considered as an oscillating induced dipole, the total intensity of the Stokes Raman scattered light can be explained through dipole radiation. The total intensity of dipole radiation is given by [64]

$$I = \frac{2}{3c^3}\ddot{p}^{\,2} \tag{2.14}$$

To obtain the total intensity, substitute the second term in equation (2.11) to equation (2.14) with temporal average. The total intensity of Stokes Raman scattered light is

$$I_{\text{Stokes}} = \frac{1}{12c^3}\left(\frac{\partial\alpha_{\rho\sigma}}{\partial Q_k}\right)_0^2 Q_{k0}^2 E_0^2 \left(\omega_0 - \omega_k\right)^4 \tag{2.15}$$

2.3.3 Selection rules

According to the equation (2.11), $(\alpha_{\rho\sigma})_0$ be non-zero for Rayleigh scattering to occur. For most molecules, the equilibrium polarizability tensor may have at least one non-zero component, so Rayleigh scattering almost always occurs. Meanwhile, $(\partial\alpha_{\rho\sigma}/\partial Q_k)_0$ be non-zero to occur Raman scattering. This gives an intuitive understanding of Raman activity or the 'selection rule' of Raman scattering in a classical form which is useful for discriminating Raman scattering from the infrared (IR) absorption. The information from IR spectroscopy and Raman spectroscopy is similar but they give different spectra because of different selection rules.

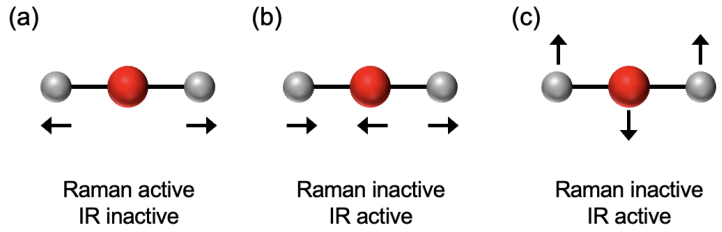

Figure 2.3: (a)-(c) vibrational modes of linear triatomic molecule.

Diatomic molecules

let's consider the diatomic molecule A_2, which has only one vibrational mode. In this case, there is no permanent dipole due to symmetry, and the dipole moment will not change during vibration. Therefore, it is infrared (IR) inactive. meanwhile, the molecule can be considered to have non-zero polarizability. When the distance between two atoms is infinitely far, it has the polarizability of two atoms with half mass, while when the distance is zero, it will have the value of a single atom. As is already known, the polarizability of two atoms is greater than one [65]. Therefore, it has monotonically increasing polarizability with distance, and its derivative will also be non-zero at equilibrium. Therefore, this molecule is Raman active. The molecule AB composed of different atoms A and B is IR active and also Raman active because the symmetry is broken.

Triatomic molecules

Let's consider the linear molecule ABA, which is composed of two different atoms, A and B. As a first-order approximation, the dipole moment and polarizability of this molecule can be calculated as the sum of the dipole moments of two diatomic molecules and the sum of the polarizabilities of two diatomic molecules, respectively. However, the vibrational modes are more complex than those of diatomic molecules. The linear triatomic molecule ABA has three vibration modes, symmetric stretching mode Q_1, anti-symmetric stretching mode Q_2, and bending mode Q_3. (see figure 2.3.(a)-(c)) Although this molecule does not have a permanent dipole moment due to symmetry, the change of dipole moment while oscillation varies depending on the vibration mode.

For symmetric stretching mode Q_1, it is IR inactive and Raman active by symmetry. Since the polarizability of the normal coordinate is monotonically increased similar to that of the diatomic molecule, the polarizability derivative at equilibrium is non-zero. However, the situation for anti-symmetric stretching mode Q_2 is slightly different. When one AB bond is stretched, the other AB bond is compressed. Therefore, the symmetry is broken and this mode is IR active. The polarizability according to the normal coordinate is canceled at anti-symmetric oscillation, resulting in a form similar to a U-shaped quadratic curve, and the polarizability derivative at equilibrium is zero, so this mode is Raman inactive. For the bending mode Q_3, it is IR active since the dipole moment change is obviously non-zero. The polarizability of the bending mode also has a quadratic curve shape when considered as the sum of two dipoles,

so the polarizability derivative at equilibrium under the small displacement condition is 0, so it is Raman inactive.

2.4 Surface-enhanced Raman spectroscopy

In 1974, the first surface-enhanced Raman spectroscopy (SERS) is demonstrated at a silver electrode [66]. Since then, SERS has been widely used as a promising analysis tool in chemistry and biology [67–69]. Generally, SERS signals are observed for molecules adsorbed on metallic nanostructures such as nano-particles and nano-rugged surfaces made of noble metals. Silver and gold are the most widely used noble metals. In addition, the emitted Raman signal intensity per molecule in SERS is increased by $10^{11} \sim 10^{13}$ compared with normal Raman intensity [70, 71]. With such a high enhancement factor, single molecule detection is possible in SERS [71].

2.4.1 Enhancement mechanism

The intensity of Raman scattering described in classical theory is proportional to the square of the polarizability derivative and the square of the electric field. Therefore, the enhancement mechanism can also be divided into two ways. A main enhancement mechanism is an electromagnetic enhancement due to the enhancement of the electric field intensity. Field intensity is enhanced by plasmonic resonance near the metallic nanostructures. The detailed mechanism is described and discussed in the following sections. In addition, not only the incident wave is enhanced by the metallic nanostructures, but also the Raman scattered light radiated from the molecule is enhanced by the

same nanostructure. Therefore, it serves as a receiver from far-field to near-field and a transmitter from near-field to far-field at the same time. Also, $EF_{\text{total}} = EF_{\text{receiver}} \times EF_{\text{transmitter}}$. If the enhancement factor (EF) is defined as the ratio of the enhanced intensity and the incident intensity, the total EF is as follows because the incident frequency and Raman frequency are close to each other.

$$EF_{\text{total}} \approx \frac{|E_{\text{LSP}}(\omega_0)|^2}{|E(\omega_0)|^2} \cdot \frac{|E_{\text{LSP}}(\omega_{\text{Raman}})|^2}{|E(\omega_{\text{Raman}})|^2} \approx \frac{|E_{\text{LSP}}(\omega_{\text{Raman}})|^4}{|E(\omega_0)|^4} \tag{2.16}$$

Another enhancement mechanism is a chemical enhancement which enhances Raman signal less than electromagnetic enhancement. The chemical enhancement can be explained by the interplay of field enhancement and metal-molecule charge-transfer [72–74]. When molecules are adsorbed on the metal surface, a metal-molecule system is formed and charge-transfer between metal and molecules becomes possible. Therefore, when the energy of the localized surface plasmon (LSP) matches the difference between the Fermi level of metal and the lowest unoccupied molecular orbital (LUMO) of the molecule, excitation to the LUMO of the molecule resonantly occurs [74].

Plasmonic resonance

The optical properties of metals are frequency-dependent. It is because electrons inside metals, especially noble metals, behave like plasma. If the electron cloud inside the neutral noble metal placed between the two parallel plates is considered as free electrons and there is a displacement of z in the electron

cloud, they will follow the equation of motion below.

$$m_e \ddot{z} = -\frac{ne^2}{\epsilon_0} z \tag{2.17}$$

Here, n is the electron density, m_e and e are the mass of electrons and elementary charge, respectively. So, they have the resonance frequency at plasma frequency ω_p which is defined as

$$\omega_p = \sqrt{\frac{ne^2}{m\epsilon_0}} \tag{2.18}$$

In a realistic metal model, there is a damping due to electron-lattice interaction and not all electrons are free electrons. Hence, there is a restoring force from the response of bound electrons. So the dielectric function of noble metals has frequency-dependent with a resonance. The equation of motion for excited bound electrons in the classical picture is

$$m_e \frac{\partial^2 r}{\partial t^2} + m_e \Gamma \frac{\partial r}{\partial t} + \alpha r = e E_0 e^{-i\omega t} \tag{2.19}$$

where m_e is the effective mass of bound electrons, Γ is the damping term, α is a spring constant, and E_0, ω is the amplitude and frequency of excitation field. Using $r = r_0 e^{-i\omega t}$ as the ansatz, the macroscopic polarization P of this system is

$$P = ner_0 = \frac{ne^2 z E_0}{m\omega^2 + \alpha - im\omega\Gamma} \tag{2.20}$$

And polarization is $P = \epsilon_o \chi_e(\omega) E(\omega)$, and displacement field is $D(\omega) = \epsilon_0 \epsilon E(\omega) = \epsilon_0 E(\omega) + P(\omega)$. So,

$$\epsilon(\omega) = 1 + \frac{\omega_p^2}{(\omega_0^2 - \omega^2) - i\Gamma\omega} \tag{2.21}$$

This can be divided into the real part and the imaginary part.

$$\epsilon_{re}(\omega) = 1 + \frac{\omega_p^2(\omega_0^2 - \omega^2)}{(\omega_0^2 - \omega^2)^2 + \gamma^2\omega^2} \tag{2.22}$$

$$\epsilon_{im}(\omega) = \frac{\gamma\omega_p^2\omega}{(\omega_0^2 - \omega^2)^2 + \gamma^2\omega^2} \tag{2.23}$$

Field enhancement for spherical particle

When the monochromatic plane wave with the amplitude E_0 and the frequency ω is applied to the small spherical metal particle with radius a, there is an enhancement due to the plasmonic resonance. The Laplace equation in spherical coordinates is

$$\frac{1}{r^2 \sin\theta}\left[\sin\theta\frac{\partial}{\partial r}\left(r^2\frac{\partial}{\partial r}\right) + \frac{\partial}{\partial\theta}\left(\sin\theta\frac{\partial}{\partial\theta}\right) + \frac{1}{\sin\theta}\frac{\partial^2}{\partial\phi^2}\right]\Phi(r,\theta,\phi) = 0 \tag{2.24}$$

The general solution has the following form.

$$\Phi(r,\theta,\phi) = \sum_{l,m}\Phi_{l,m}(r,\theta,\phi) \tag{2.25}$$

with

$$\Phi_{l,m} = R_l(r)Y_{l,m}(\theta,\phi) \tag{2.26}$$

with

$$R_l(r) = A_l r^l + B_l r^{-(l+1)} \tag{2.27}$$

and,

$$Y_{l,m}(\theta,\phi) = C_{l,m}P_l^m(\cos\theta)e^{im\phi} \tag{2.28}$$

Here, P_l^m is associated Legendre function. A_l, B_l, and $C_{l,m}$ is the coefficient of each solution which is determined by the boundary condition. From the continuity condition, the field inside the particle and the field outside the particle

should be the same at $r = a$. So,

$$\left[\frac{\partial \Phi_i}{\partial \theta}\right]_{r=a} = \left[\frac{\partial \Phi_o}{\partial \theta}\right]_{r=a} \tag{2.29}$$

$$\epsilon_i \left[\frac{\partial \Phi_i}{\partial r}\right]_{r=a} = \epsilon_o \left[\frac{\partial \Phi_o}{\partial r}\right]_{r=a} \tag{2.30}$$

Where Φ_i, Φ_o is the potential at the inside of the particle and at the outside of the particle, respectively. ϵ_i, ϵ_o a dielectric constant at the inside of the particle and at the outside of the particle. If the incident wave propagates along the z-axis, $\Phi_0 = -E_0 z = -E_0 r\cos\theta$ Find the solution using the boundary condition $r \to \infty$ and $r \to 0$.

$$\Phi_i = -E_0 \frac{3\epsilon_o}{\epsilon_i + 2\epsilon_o} r\cos\theta \tag{2.31}$$

$$\Phi_o = -E_0 r\cos\theta + E_0 \frac{\epsilon_i - \epsilon_o}{\epsilon_i + 2\epsilon_o} \frac{\cos\theta}{r^2} a^3 \tag{2.32}$$

So, the electric field $\vec{E} = -\nabla\Phi$ is

$$\vec{E_i} = E_0 \frac{3\epsilon_o}{\epsilon_i + 2\epsilon_o} \hat{n}_z \tag{2.33}$$

$$\vec{E_o} = E_0 \hat{n}_z + E_0 \frac{a^3}{r^3} \frac{\epsilon_i - \epsilon_o}{\epsilon_i + 2\epsilon_o} (2\cos\theta \hat{n}_r + \sin\theta \hat{n}_\theta) \tag{2.34}$$

The scattered field intensity near the surface of the metal particles is,

$$|\vec{E_0}|^2_{r\approx a} = E_0^2 \left|\frac{\epsilon_i - \epsilon_o}{\epsilon_i + 2\epsilon_o}\right|^2 (1 + 3\cos\theta) \tag{2.35}$$

We can define g associated with the field enhancement.

$$g = \left|\frac{\epsilon_i - \epsilon_o}{\epsilon_i + 2\epsilon_o}\right| \tag{2.36}$$

If the medium around the particle does not have frequency-dependent, ϵ_o can be considered as a constant without an imaginary part. Because the dielectric

function of a metal depends on the wavelength, the gain becomes very high under the condition that $Re(\epsilon_i) \approx -2\epsilon_o$ and $Im(\epsilon_i) << 1$. Also, since the field intensity decreases in proportion to r^{-3}, field enhancement only occurs near the particle usually within a few nanometers.

2.5 Tip-enhanced Raman spectroscopy

Tip-enhanced Raman spectroscopy (TERS) is a near-field optical instrument that combines Raman spectroscopy and scanning probe microscopy (SPM) with a metallic probe, which enhances the electromagnetic field near the apex of the probe. Therefore, TERS has both advantages of SPM and SERS. It has been reported that the enhancement factor of TERS is slightly lower than that of SERS, but TERS has much higher spatial resolution than SERS [75–77], and sophisticated system control is also possible in TERS. The enhancement mechanism is the same as that of SERS. But since the probe geometry is quite different from the metallic nanostructure used in SERS, the enhancement phenomenon that occurs in tip geometry is called the lightning-rod effect. The idea of TERS was first proposed in 1985 [78] but it was experimentally realized in 2000 [79–82]. It has been reported to have an enhancement factor of TERS is lower than 10^9 [30, 76] which is lower than the known enhancement factor of SERS 10^{11} to 10^{13}, but in recent studies using high vacuum TERS with CO terminated probe, it was possible to obtain an enhancement factor of 10^{12} and perform chemical mapping of the single molecule [29, 83].

2.5.1 Enhancement factor

The enhancement factor is a parameter that quantifies the degree of enhancement and is defined as the ratio of enhanced Raman signal intensity per molecule and the intensity of the normal micro-Raman signal per molecule. An enhancement factor can be defined as follows in general.

$$\mathrm{EF} = \frac{I_{\mathrm{NF}}}{I_{\mathrm{FF}}} \cdot \frac{V_{\mathrm{FF}}}{V_{\mathrm{NF}}} \tag{2.37}$$

where I_{NF} is the intensity of the near-field, I_{FF} is the intensity of the far-field, V_{FF} is the focal volume of the far-field, and V_{NF} is the volume of the near-field. In TERS experiments, the target molecules are generally absorbed to the surface of the substrate, so the beam spot at the surface may need to be considered, instead of the total focal volume of the field. In addition, unlike the SERS experiment, TERS can measure the near-field signal and the far-field signal in the same experimental circumstance through the 'tip-in' signal and 'tip-out' signal according to the tip-sample distance. And, since I_{NF} is the difference between the 'tip-in' signal and the 'tip-out' signal, EF in TERS can be approximated as follows.

$$\mathrm{EF} \approx \frac{I_{\text{tip-in}} - I_{\text{tip-out}}}{I_{\text{tip-out}}} \cdot \frac{A_{\mathrm{FF}}}{A_{\mathrm{NF}}} \tag{2.38}$$

where $I_{\text{tip-in}}$ is the intensity of the 'tip-in' signal, $I_{\text{tip-out}}$ is the intensity of the 'tip-out' signal, A_{FF} is the area of the far-field beam spot, and A_{NF} is the area of the near-field beam spot. The far-field beam spot size can be measured by scanning the beam across a knife edge, and the near-field beam spot size can be calculated through finite-difference time-domain (FDTD) simulation.

$I_{\text{tip-in}}$ and $I_{\text{tip-out}}$ can be easily obtained experimentally, but beam spot sizes are not. Therefore, a more practical quantity for EF expressed only with $I_{\text{tip-in}}$ and $I_{\text{tip-out}}$ is introduced, which is called Contrast and can be defined as follows.

$$C_{\text{TERS}} = \frac{I_{\text{NF}}}{I_{\text{FF}}} = \frac{I_{\text{tip-in}}}{I_{\text{tip-out}}} - 1 \tag{2.39}$$

Chapter 3

Experimental setup

3.1 System overview

The schematics of our experimental setup and the actual photo of TERS is shown in figure 3.1 and in figure 3.2, respectively. A quartz tuning fork (QTF) is electrically driven by a function generator. (33120A, Agilent) The resonance frequency of canned QTF is 32764 Hz. After opening QTF, the resonance frequency is decreased to 32758 $\pm$ 4 Hz due to the interaction with air. The resonance frequency of tip-attached QTF is decreased again depending on the mass of the attached tip.

When the QTF oscillates, the oscillating current is generated (deflection current), and the deflection current from electrically excited QTF has to be converted into voltage by the current-to-voltage converter (preamplifier or transimpedance amplifier, TIA) in small amplitude AFM. Our preamplifier is com-

posed of an OPAMP (OPA657, Texas instruments) and a feedback resistor of 1 GΩ. We also examined several types of preamplifiers including T-network TIA. QTF and preamplifier are attached to the AFM head.

The signal from the preamplifier fed into the lock-in amplifier (7265, EG&G instruments). The amplitude and the phase signal are extracted from the lock-in amplifier and recorded by the LabVIEW DAQ module. Because our AFM is amplitude-modulation (AM) AFM, QTF is not contained in a closed feedback loop. The computer communicates with the function generator and the lock-in amplifier using GPIB protocol.

There are three-axis piezoelectric transducers (PZT) (PI) for AFM sample scanning and a picomotor (Newport) for a z-axis coarse movement of AFM head. PZT is controlled by a homebuilt high voltage amplifier (HVA) with a gain of -22. Long-term stability and low noise intensity are also checked.

Our QTF is operated in shear mode. Because QTF laterally oscillates to the substrate, tip-substrate distance is almost fixed during measurement. And tip-substrate distance-dependent force is not detected and only shear direction force from the nano-meniscus are detected.

AFM head made of Invar, nickel–iron alloy which has an extremely low thermal expansion coefficient ($\alpha \sim 1.2 \times 10^{-6} K^{-1}$ at room temperature) is attached to a z-axis moving plate on manual stainless steel stage (Newport). And sample scanning PZT is glued to the same manual stage, but on the x- and y-axis moving plate. The sample holder with an aperture is glued to PZT with vacuum epoxy (Torr seal). So, there is no relative motion between the sample holder and the AFM head when the x-, and y-axis stage is moving. But there

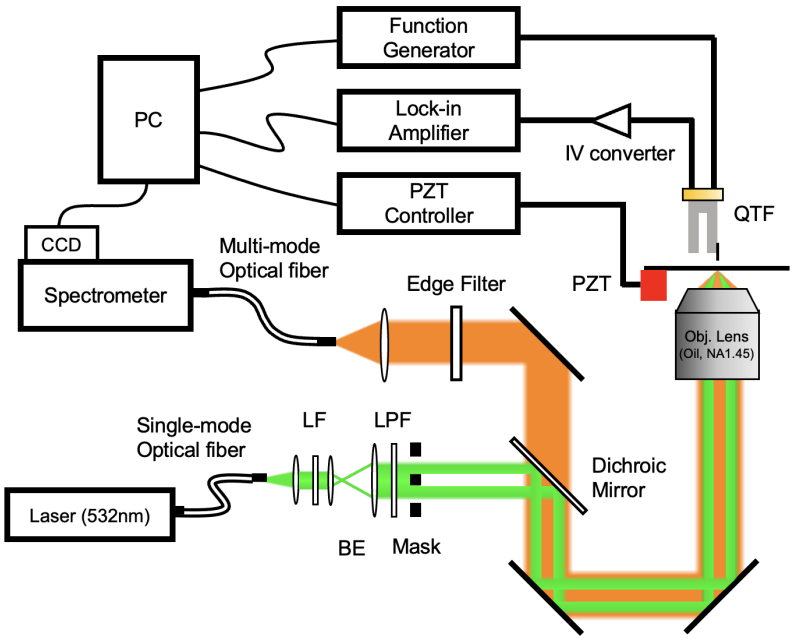

Figure 3.1: Scheme of the homebuilt TERS setup. BE; beam expander, LF; line filter for 532 nm laser, LPF; linear polarizer filter, PZT; piezoelectric transducer, an objective lens with NA = 1.45.

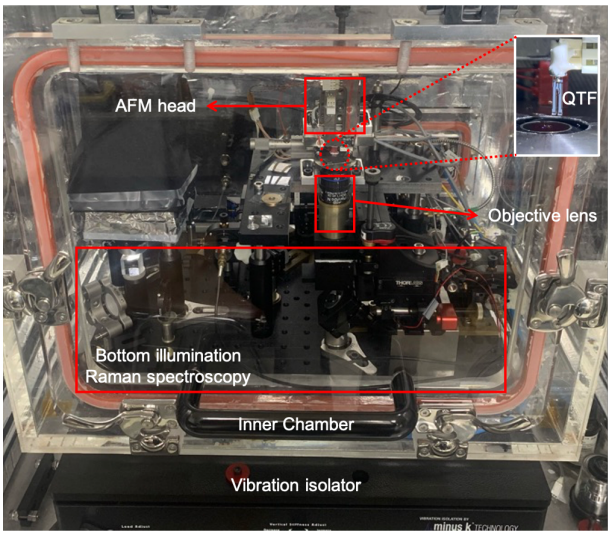

Figure 3.2: Photo of experimental setup

is relative motion between them when the z-axis stage is moving. A picomotor is attached at the z-axis manual stage instead of the micrometer.

For Raman spectroscopy, a 532 nm laser beam is used for excitation, which is expanded to 12 mm diameter using two lenses after collimation. To reduce the unwanted background signals, we use only the large NA (> 1) component of the laser beam by blocking its small NA (< 1) part with an optical mask [84]. High NA objectives are employed for high excitation/detection efficiency (PlanApo, 60×, 1.45NA, Olympus). The backscattered Raman signal is collected by the same objective, passed through a cut-off filter to block the Rayleigh scattering signal and detected by a fiber-coupled spectrometer (UHTS 300 VIS, 600lines/mm, Witec) with an EMCCD camera (DU970P, Andor).

The entire TERS setup is enclosed in the airtight humidity-controlled chamber.

3.2 QTF-based atomic force microscopy

3.2.1 AFM controller

DC supply

There are two kinds of power supply to convert AC to DC, a linear power supply and a switching power supply (or switching-mode power supply, SMPS). The linear power supply has a heavy power transformer right after input, and its structure is quite simple. Its energy efficiency is not good because of the loss at the transformer, but the noise level is low because it has no additional noise source. However, the switching power supply has a rectifier right after input, followed by the switch and the high-frequency transformer. Because of the switch, the noise level is higher than the linear power supply but it is lighter, cheaper, and smaller than the linear power supply due to the absence of a heavy power transformer.

Our AFM controller has three DC supplies, $\pm$ 15 V, $\pm$ 5 V, $\pm$ 250 V. We use the linear power supply (Goldbox, Acopian) because a stable and a low-noise supply is needed in our AFM controller. For a unity gain OPAMP, DC supply noise is attenuated by the power-supply rejection ratio (PSRR) and applied to output noise. OPAMP we use in our setup, PSRR of OPA657 is 70$\sim$90 dB, PSRR of PA88 is $\sim$ 100 dB, and PSRR of LF356 is $\sim$ 100 dB. So, the required RMS noise level in the given bandwidth in our controller is a few tens of μV.

The power spectrum of DC supply is shown in figure 3.3.(a), (b). The red solid line is measured without a low pass filter (LPF), and the black solid line

is measured with LPF ($f_c = 13$ Hz). We use 1st order passive low pass filter. In figure 3.3.(c), time series signal with 3.6 kHz sampling rate is shown. Without LPF, $V_{\text{pp}} \sim 540\mu V$ and spike signal is also observed. With LPF, $V_{\text{pp}} \sim 60\mu V$ and there is no spike signal observed. We also add an additional shielding to attenuate 60 Hz noise not reduced by LPF. DC supply is placed inside an aluminum container. Power lines are wired not to overlap signal lines. And all signal lines are configured with twisted wires. As a result, 60 Hz noise is 20% attenuated.

High voltage amplifier

In general, a hard piezo-electric transducer (PZT) is used in AFM because hard PZT is not easily affected by external environmental change. So, the high voltage amplifier (HVA) is needed to drive such a hard PZT. We use PA88 (Apex microtechnology) for the high voltage amplifier with a gain of $\sim$ -22 and use LF356 (Texas instruments) for its buffer.

Figure 3.4 shows the specification of the HVA. The Gain of HVA is -22.06, -21.82, and -22.03 for channel 1, 2, and 3, respectively. In figure 3.4.(b), the output signal of HVA of the 1-bit square wave input is presented. Because our LabVIEW DAQ is 16-bit, the minimum voltage step (1-bit) from the DAC channel is 20V / 65536 = 0.305 mV. After being amplified by HVA, it is - 6.72 mV which is consistent with the experimental result. ($n_{\text{rms}} = 1.01$ mV)

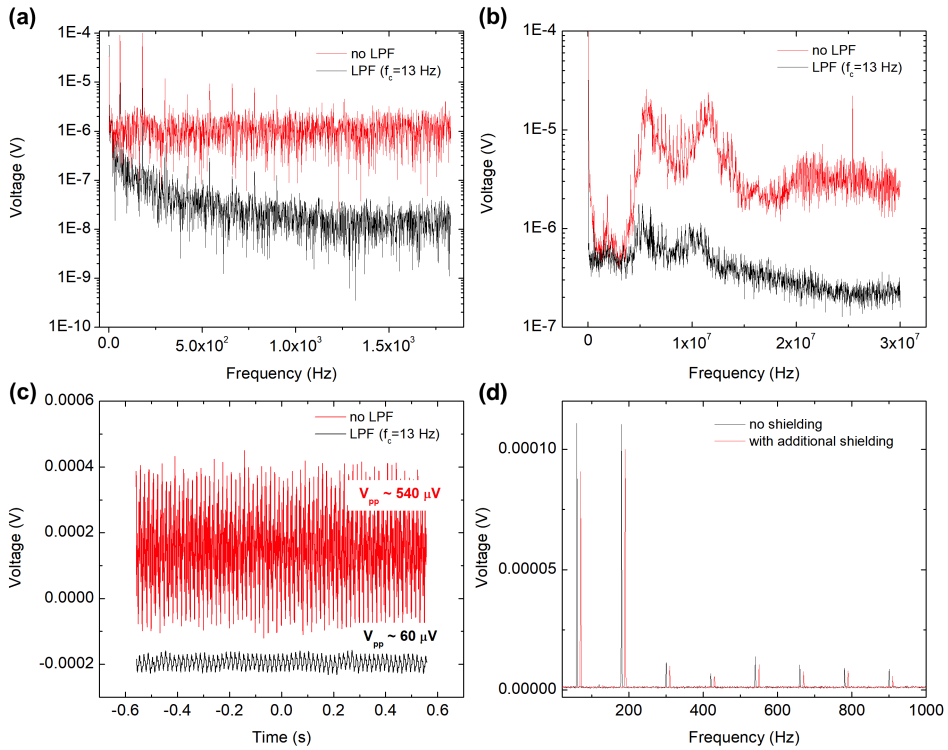

Figure 3.3: (a) power spectrum of DC supply without LPF (red) and with LPF (black) at low-frequency range (< 2 kHz). (b) power spectrum of DC supply without LPF (red) and with LPF (black) at a high-frequency range (< 30 MHz). (c) Time series signal of DC supply without LPF (red) and with LPF (black). (d) The effect of extra shielding around DC supply.

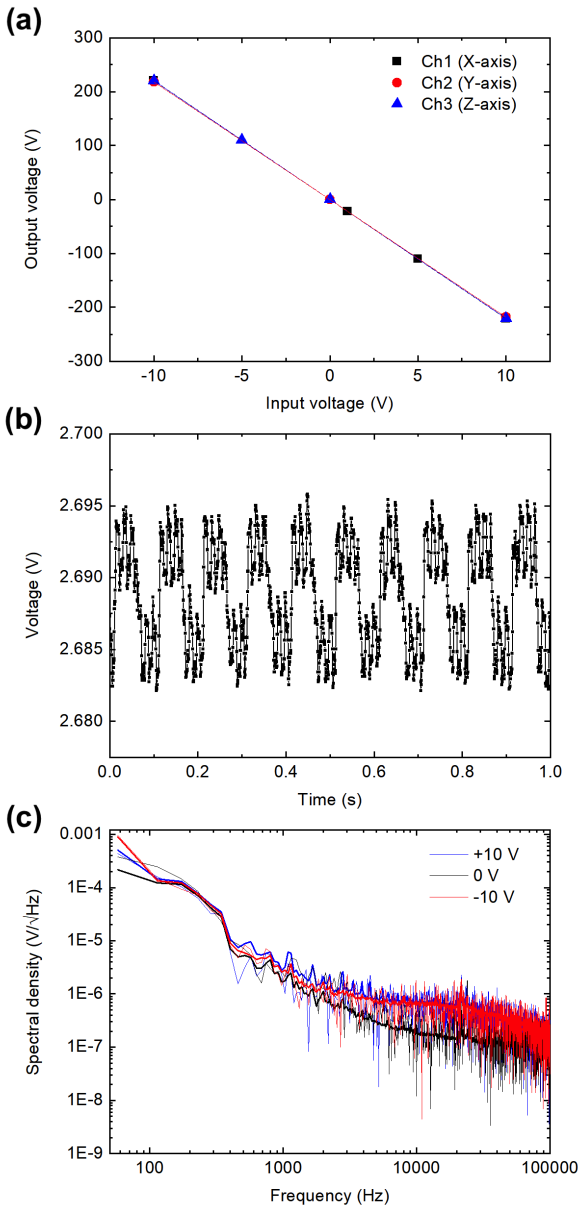

Figure 3.4: High voltage amplifier specification. (a) linearity of three channels in HVA (b) an output signal of channel 3 of the 1-bit square wave input (c) Spectral density of channel 3 at three different input voltages.

3.2.2 Preamplifier for QTF

When the QTF oscillates, a periodic charge difference is generated between electrodes attached to the surface of QTF, and an alternating deflection current flows. In small amplitude applications in various SPM, the deflection current is typically less than a few nano-amperes. It is known that such a low current flow in a bare wire is dissipated within a few tens of centimeters. So, the current of QTF is fed into a current-to-voltage amplifier (an IV converter or a transimpedance amplifier) to transmit a deflection signal of QTF further with less loss. Several types of TIA circuits for QTF pre-amplifier are shown in figure 3.5. For the differential amplifier form in figure 3.5.(b), the signal-to-noise ratio (SNR) is $\sqrt{2}$ higher than the single input amplifier because the current input signal of the differential form amplifier is 2 times higher than the single input amplifier. However, notice that the differential amplifier can only be used with mechanical driving input as shown in figure 3.5.(b).

In SPM applications, Johnson noise from resistors cannot be ignored because a high gain of $10^6 \sim 10^9$ V/A is required in this application. The root-mean-square value of Johnson noise is given by

$$n_{\mathrm{rms}} = \sqrt{4k_{\mathrm{B}}TR\Delta f} \tag{3.1}$$

where k_{B} is Boltzmann constant, T is temperature, R is a resistor, and Δf is bandwidth. It is not easy to reduce Johnson noise in a high-gain IV converter operating at room temperature because Johnson noise depends on T and R at a given bandwidth. But, in some applications, only the feedback resistor is maintained at a low temperature to minimize Johnson noise. [85] Meanwhile

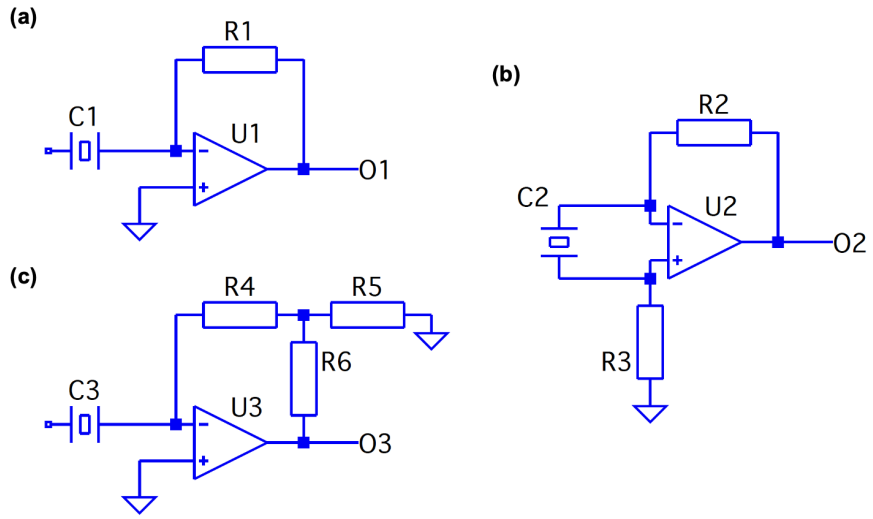

Figure 3.5: Various types of IV converter. C_i is a crystal resonator (QTF), R_i is a resistor, U_i is an OPAMP, and O_i is an output. (a) a basic form of the preamplifier with single input (b) a differential preamplifier with two inputs (c) a T-network TIA.

because the Johnson noise is dominated by the largest resistor in TIA, there is one more advantage to using T-network TIA, it has a large effective gain while having a relatively small resistance.

Gain of preamplifier

Figure 3.5.(a) shows the schematics of our preamplifier. We use OPA657 OPAMP which has a high GBWP of 1.66 GHz to extend the bandwidth of the preamplifier. To measure the frequency response of the gain, the 10pF capacitor is connected to the input C1, and the function generator is connected to the other input of the capacitor to drive. Then, the output voltage is $V_{\mathrm{out}}(f) = G(f)2\pi f C_0 V_{\mathrm{dri}}$, where G($f$) is the gain, C_0 is the capacitance of the input capacitor, and V_{dri} is the amplitude of the driving voltage. Therefore, the gain G(f) is

$$G(f) = \frac{V_{\mathrm{out}}(f)}{2\pi f C_0 V_{\mathrm{dri}}} \tag{3.2}$$

The measured gain versus frequency with various feedback resistors is shown in figure 3.6. The vertical dashed line indicates 32.7 kHz the resonance frequency of QTF. At higher feedback resistor, the gain is more rapidly reduced meaning the bandwidth is shortened. As mentioned earlier, the Johnson noise is proportional to $\sqrt{R}$, but the gain is increased slower than that. So, we use 100 MΩ as a feedback resistor to get the best SNR.

T-network tranimpedance amplifier

The bandwidth of an IV converter of gain G with OPAMP having GBWP as its gain-bandwidth product is roughly GBWP/G. So, the design of the IV

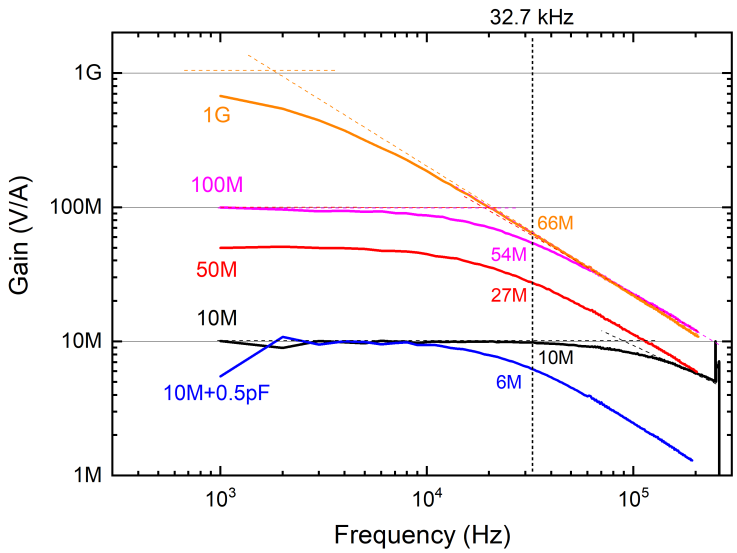

Figure 3.6: Frequency response of preamplifier with various feedback resistors. The left numbers are feedback resistor values and the right numbers are reduced gain at 32.7 kHz. The solid blue line is the preamplifier with a 0.5 pF feedback capacitor. The bandwidth is much reduced due to the feedback capacitor.

converter having a high gain ($> 10^9$ V/A) with a wide bandwidth (> 100 kHz) is a non-trivial problem because of the OPAMP nature, and there are many attempts to overcome this limitation. [52,86–90] One of the simplest solution is T-network TIA. In T-network TIA, three resistors with relatively low resistance consist of a T-shape network, resulting in TIA having high effective gain with less loss in bandwidth. Effective gain of T-network TIA is derived as follows.

$$I_6 = I_4 - I_5 = I_4(1 + \frac{R_4}{R_5}) \tag{3.3}$$

$$V_{O3} = I_4 R_4(1 + \frac{R_6}{R_4} + \frac{R_6}{R_5}) \tag{3.4}$$

$$\therefore G = R_4(1 + \frac{R_6}{R_4} + \frac{R_6}{R_5}) \tag{3.5}$$

The schematic of T-network TIA is shown in 3.5.(c). The gain is measured in the same way as above. The results are shown in figure 3.7. The bandwidth of the T-network TIA with an effective gain of 1 GV/A ($f_c \sim 9.7$ kHz) is much wider than the bandwidth of the ordinary type preamplifier ($f_c \sim 0.9$ kHz) with 1GΩ feedback resistor. Notice that the gain of T-network TIA at 32.7 kHz is 277 MV/A. This is much higher than the gain of the ordinary type preamplifier with 10MΩ feedback resistor which has the same resistor value with T-network TIA.

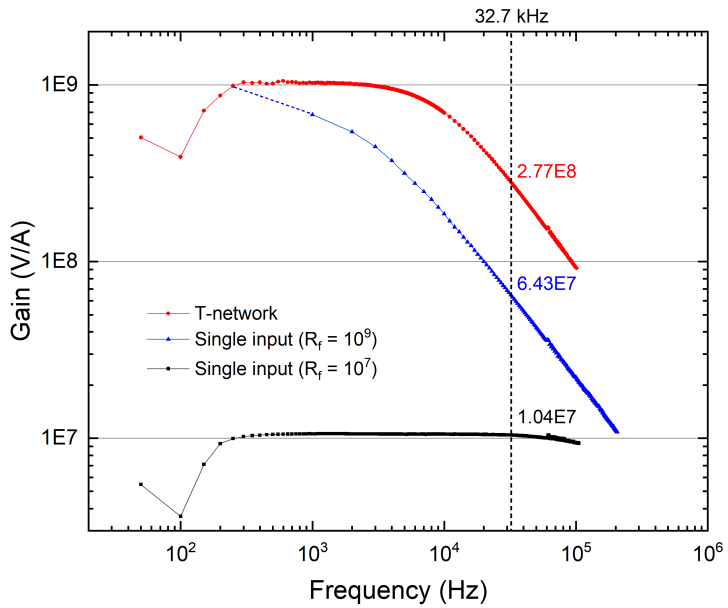

Figure 3.7: Frequency response three IV converters. (red) T-network TIA with $R_4 = 10$ MΩ, $R_5 = 1$ kΩ, and $R_6 = 100$ kΩ. The cut-off frequency $f_c \sim 9.7$ kHz. (blue) The single input IV converter with $R_f = R_1 = 1$ GΩ. The cut-off frequency $f_c \sim 0.9$ kHz. (black) The single input IV converter with $R_f = R_1 = 10$ MΩ. The cut-off frequency $f_c \sim 0.7$ GHz.

3.2.3 Mechanical modes of QTF

QTF has its fundamental mode as an in-plane (out-of-phase) bending mode at $\sim$ 32768 Hz. Besides that, QTF has other mechanical modes such as out-of-plane bending mode, torsional mode, and so on. [91] In general, the response of QTF is electrically recorded through a lock-in amplifier after passing the preamplifier. During this process, non-mechanical or purely electrical modes are also added to the power spectrum.

To identify the position of the mechanical modes of QTF, we measure the power spectrum of QTF at different conditions. (figure 3.8) To extract pure electrical signals in the power spectrum, the 12 pF capacitor, the glued QTF, and nothing is connected to the input of the preamplifier and the power spectrum is measured. We notice that some of the peaks only appeared at the bare QTF spectrum, marked as three black arrows in figure 3.8. The left peak at 32.7 kHz is obviously the fundamental mode of QTF. The middle peak at 47 kHz is expected as one of the in-phase mechanical vibration modes. The right peak at 189.3 kHz is expected as a torsional mode of QTF based on the COMSOL simulation.

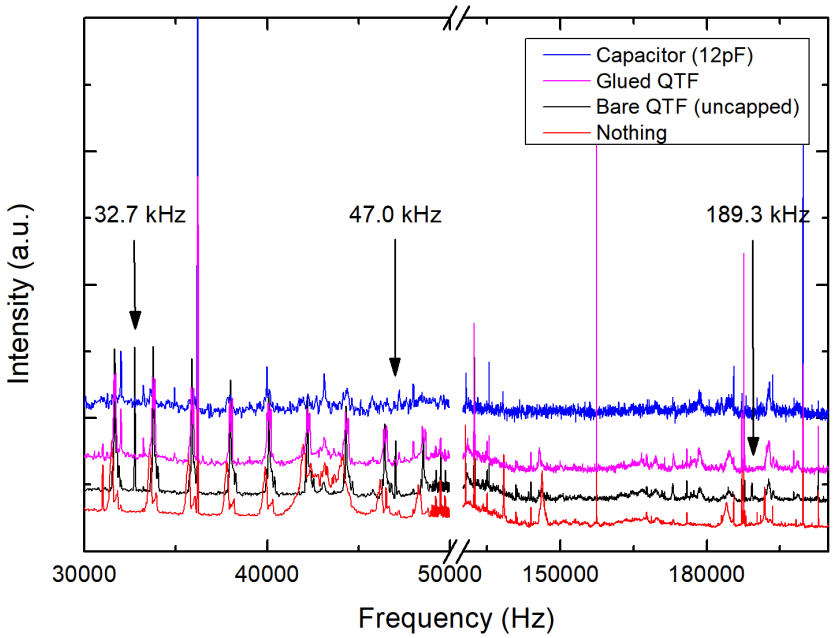

Figure 3.8: power spectrum at four different conditions. Each component is connected to an input. (blue) spectrum for a 12 pF capacitor. (pink) spectrum for a glued QTF, two prongs of QTF are tightly glued using epoxy resin. (black) spectrum for a bare QTF that is uncapped. Three black arrows indicate the mechanical modes of QTF. (red) spectrum with nothing connected.

3.2.4 Mechanical amplitude calibration

To quantitative analyze AFM data, mechanical amplitude calibration is needed. Here, the energy balance method is adopted to calibrate the mechanical amplitude of QTF [92]. The dissipated energy per cycle of QTF is

$$E_{\text{dissipation}} = \frac{2\pi}{Q} E_{\text{mech}} \tag{3.6}$$

$$= \frac{2\pi}{Q} k A_{\text{osc}}^2 \tag{3.7}$$

Q is the quality factor, k is a spring constant of the probe, and A_{osc} is mechanical oscillation amplitude. The electrically supplied power to the oscillator is

$$P = \frac{1}{2} V_{\text{drive}} I_m \cos\phi \tag{3.8}$$

V_{drive} is excitation voltage, I_m is current induced by the oscillator, ϕ is relative phase of I_m with respect to V_{drive} and ϕ become zero at resonance frequency. To maintain constant amplitude, dissipated energy per unit time should be equal to supplied power. Hence,

$$A_{\text{osc}} = \sqrt{\frac{V_{\text{drive}} I_m Q}{2\pi f_0 k}} \tag{3.9}$$

f_0 is resonance frequency. All parameters in equation (3.9) can be experimentally or numerically determined. Q, f_0 can be extracted from the resonance curves of QTF. and k can be calculated using finite element methods or experimentally measured [93]. However when QTF is electrically self-excited, measured current from lock-in amplifier I_e should be transformed to the I_m because electrically induced current I_e passes through the stray capacitance in

the crystal resonator [49, 50]. This transform is achieved by the following analytical formula from the crystal resonator equivalent circuit including the stray capacitance [50].

$$I_{e(m)} = A_{e(m)} \sin \omega t + \theta_{e(m)} \tag{3.10}$$

$$A_m = \sqrt{A_e^2 - 2\left(\frac{\omega}{\omega_0}\frac{C_0 I_0}{CQ}\right) A_e \sin\theta_e + \left(\frac{\omega}{\omega_0}\frac{C_0 I_0}{CQ}\right)^2} \tag{3.11}$$

$$\theta_m = arg\left[A_e \cos\theta_e + i\left(A_e \sin\theta_e - \frac{\omega}{\omega_0}\frac{C_0 I_0}{CQ}\right)\right] \tag{3.12}$$

The total current after passing the preamplifier is measured by the lock-in amplifier as the voltage, which is expressed as $V_{\text{out}} = I_{\text{out}} G$ with the gain G of the pre-amplifier. Finally, the following relation is derived.

$$A_{\text{osc}} = \alpha \times V_{\text{drive}} \tag{3.13}$$

$$\text{where}, \alpha = \sqrt{\frac{I_{\text{mech}} Q}{2\pi f_0 k V_{\text{drive}}}} \tag{3.14}$$

To calibrate our electrically driven QTF (LFXTAL002995, IQD frequency products), we measure the resonance curves at the fundamental mode (left figure in figure 3.9) and convert it to mechanically driven amplitude (right figure in figure 3.9) using the relation between them (equation (3.11)). The electrically driven resonance curves have an anti-resonance peak because of the stray capacitance effect. This can be decoupled by solving an equivalent circuit of the crystal resonator [50, 94]. There are four parameters in this equation, I_0 is the initial current, Q is the quality factor, f_0 is the resonance frequency, and C_0/C is the ratio of stray capacitance and crystal capacitance. As a result, the calibration factor between the mechanical amplitude and electrical signal is α = 31.1687 Å/mV.

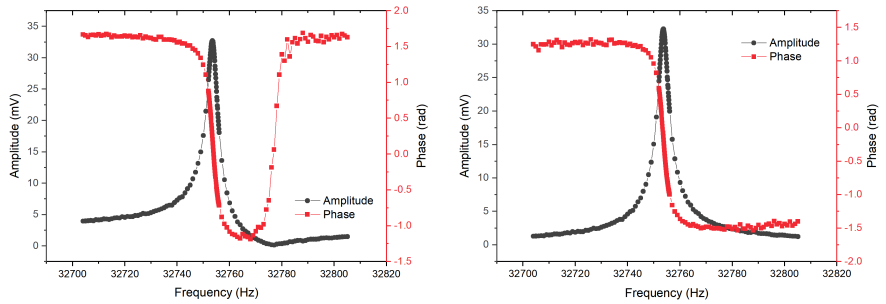

Figure 3.9: The resonance curve near the fundamental mode. (left) measured electrically driven resonance curve. (right) mechanically driven resonance curve converted from an electrically driven curve. The four fitting parameters are I_0 = 32.484, Q = 8456.479, f_0 = 32753.657 Hz, C_0/C = 703.859.

3.3 Raman spectroscopy

SPM is usually mounted on a vibration isolator. Therefore, we place our Raman spectroscopy on the same vibration isolator. If the Raman spectroscopy and the SPM are mounted on different isolators, the optical alignment will be distorted due to the position difference between the two isolators. The Raman optics are placed on a passive vibration isolator (BM-8, minus-k technology) on an optical table (Jinsung laser). A 532nm CW excitation laser and a spectrometer (UHTS 300 VIS, 600lines/mm, Witec) are placed on the optical table and fiber coupled with the Raman optics.

The excitation laser is expanded to a 12 mm diameter beam using two lenses after collimation. A collimated beam of 2 mm diameter is expanded to fully cover the back side of the objective lens. Additionally, after beam expansion, a metal thin film mask is placed to block the small NA excitation beam of NA

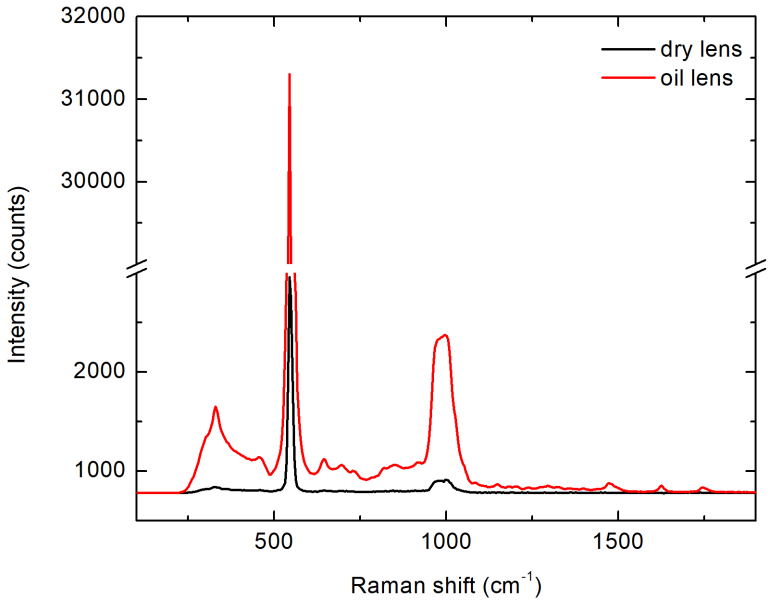

Figure 3.10: The silicon wafer signal with a dry objective lens of NA 0.9 (black) and with an oil objective lens of NA 1.45 (red). laser power is 2.5 mW with 1 second integration time.

$<$ 1. As is well known, a large NA light can maximize the lightning-rod effect, while a low NA light may responsible for unwanted background signals [84].

large NA oil objective lens is used as the objective lens (PlanApo, 60×, 1.45NA, Olympus), and its intensity is compared with a dry objective lens (Zeiss) of NA 0.9 in figure 3.10.

Raman signal is collected by the same objective lens for excitation, and it passes through a cut-off filter (Semrock) to block the Rayleigh scattered light and focused into fiber-coupled spectrometer (UHTS 300 VIS, 600lines/mm,

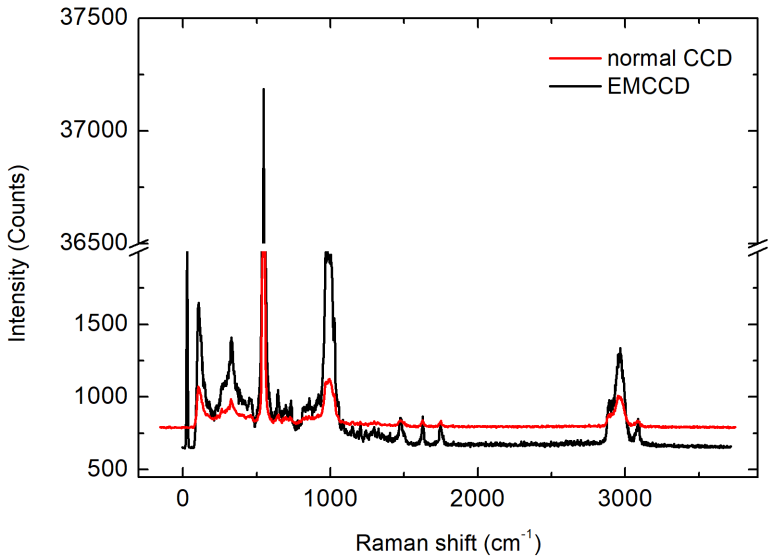

Figure 3.11: Raman measurement for calibration and to test CCD performance. The silicon wafer is measured with normal CCD (red) with SNR of 10^4 and EMCCD (black) with SNR of 2.3×10^4 with respect to peak at 520 cm^{-1}. laser power is 1 mW with 1 second integration time.

Witec) with an EMCCD camera (DU970P, Andor).

Raman spectroscopy is calibrated with a silicon wafer and butanol. In addition, an additional SNR increase is observed by using the electron multiplying (EM) mode of EMCCD. (see figure 3.11) notice that the background signal due to thermal noise in EMCCD is lower than normal CCD. However, the efficiency of EMCCD compared to normal CCD is lowered for the long integration time, and the efficiency of normal CCD and EMCCD become eventually similar at integration time longer than a few minutes.

3.4 Tip fabrication

Enhancement of the Raman signal of molecules within 'hotspot' is affected by many factors, but among them, the tip is the most important factor. For the TERS tip, materials, methods of fabrication, cone angle, and diameter of tip apex are the main factors [95–100]. We use silver as a tip material since a 532 nm green solid-state laser is used in our setup. And, we tested three different fabrication methods, etching, E-beam evaporation coating, and sputter coating. For the coating methods, three types of cantilevers are examined with respect to their aspect ratio. The diameter of the tip is not solely controlled, for example, the coating thickness determines the diameter of the tip apex. For the etching tip, each parameter can not be solely controlled since the cone angle, the diameter of the apex, and the shape are intricately correlated in the etching process.

The fabricated tip is glued using UV adhesive (NOA88, Norland) to one

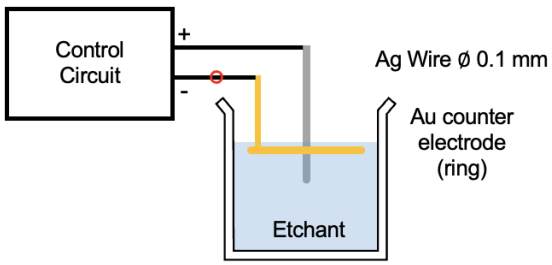

Figure 3.12: Schematics of the etching setup.

prong of the QTF immediately after fabrication. The experiment is conducted within 3 hours after tip fabrication to minimize oxidation of the silver surface which caused a reduction of the enhancement factor.

Etching

The schematic of the etching setup is shown in figure 3.12. The electrochemical etching of the 0.1 mm diameter Ag wire (99.99%, Goodfellow) is conducted for the etching tips. 0.1 mm diameter Au wire (99.9%, Sigma Aldrich) is made in a circular form with a diameter of 1 cm and used as a counter electrode. A 1:4 mixture of perchloric acid (70%, Sigma Aldrich) and ethanol (99.9%, Daejung) is used as an etchant. A 6 V of dc voltage is applied between the Ag wire and counter electrode after they are immersed in the etchant (5 mm and 0.2 mm from the surface, respectively). The fabricated tip is washed with deionized water (Arioso Power I, Human corporation).

An etching process is monitored by the Labview and controlled by the etching circuit [101]. (figure 3.13) In our experimental setup, the control circuit was necessary to prevent overetching of the Ag tips. The overetching occurs because

of the time delay between the termination time and the actual termination time at the fast etching process. For example, when Ag etching is only controlled with slow Labview software, the time delay between the zero voltage command and the actual time to be zero voltage is a few milliseconds. This is enough time for silver to be etched hundreds of nanometers more. The comparator in the control circuit compares the reference voltage and the voltage drop after etching (red dot in figure 3.12). When the two input voltages are equal, the etching process is terminated by the MOSFETs in the control circuit. Then, the time delay is reduced to the order of the response time of the MOSFET, which is $\sim 3\ \mu s$.

A small bump at 17 seconds in the black curve in figure 3.14 indicates the overetching at the last stage of the etching process. As shown in the red curve in figure 3.14, the overetching disappeared with the control circuit with a proper reference voltage. The images of the typical etching tip of the diameter of $\sim$ 100 nm at the optimized etching condition are shown in figure 3.15.

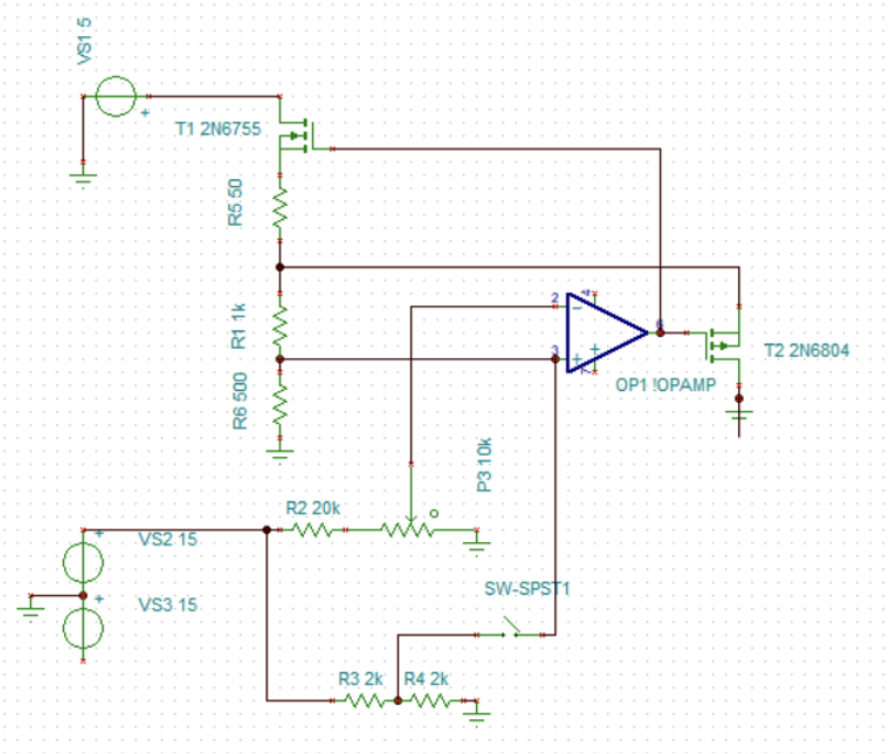

Figure 3.13: Circuit diagram of the etching control circuit. This circuit is designed to prevent overetching of the fast etching process using comparator and MOSFETs. R1 is the etching parts. OP1 is the comparator. T1 and T2 are the MOSFETs.

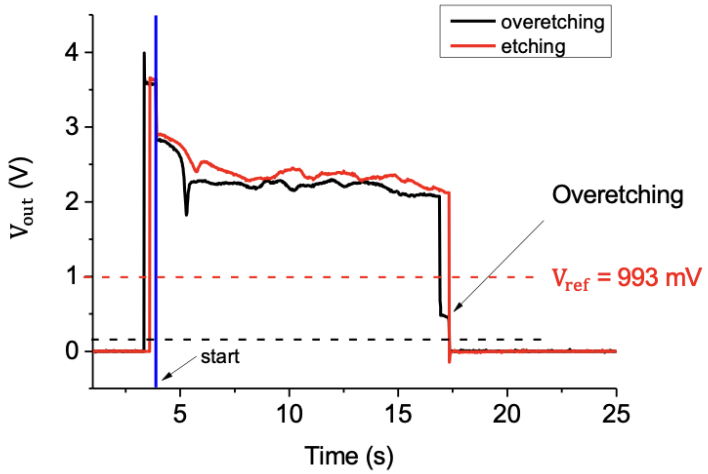

Figure 3.14: The typical etching curves without the control circuit (black) and with the control circuit (red). The etching process starts at $\sim$ 3.7 seconds (The vertical blue line). The horizontal dashed lines are the reference voltage.

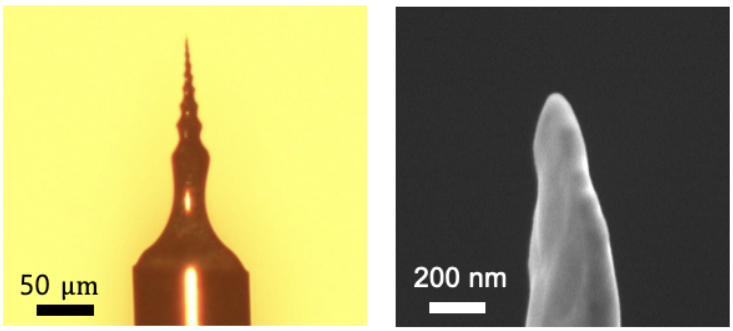

Figure 3.15: The typical SEM images of etching tips with an average diameter of 100 nm.

E-beam evaporation coating

For the coating methods, we tested three types of commercial cantilever probes depending on their aspect ratio, commonly used cantilever probe with 2 $\sim$ 3 aspect ratio (PPP-NCHR, Nanosensors), top visible type cantilever probe with 5 $\sim$ 6 aspect ratio (ATEC-CONT, Nanosensors), and high aspect ratio probe with $>$ 10 aspect ratio (AR-NCHR, Nanosensors). We decide to use a cantilever probe with a medium aspect ratio. (See Appendix.C and Appendix.A for details)

Ag film is coated by the E-beam evaporator on the commercial AFM cantilever tips (ATEC-CONT, Nanosensors). The cantilever is placed in a UV Ozone cleaner (UVC-150, Omniscience) for 30 min before metal coating to remove organic contamination from the surface. Without the UV Ozone treatment, a strong signal from contaminants is observed during experiments, while the contaminants also affected the Ag-coating adhesion strength to the surface [102]. The tips are coated using an E-beam evaporator (KVE-E4006L, Korea vacuum tech) at 10^{-6} Torr. 3 nm thick chromium (Cr) is coated at a rate of 0.35 Å/s as an adhesive layer, and then 30 nm thick Ag is coated at a rate of 4.5 Å/s on the Cr layer without breaking vacuum. The average diameter of the TERS tip is about 70 nm. The SEM image of the typical E-beam coated TERS tip is shown in figure 3.16.

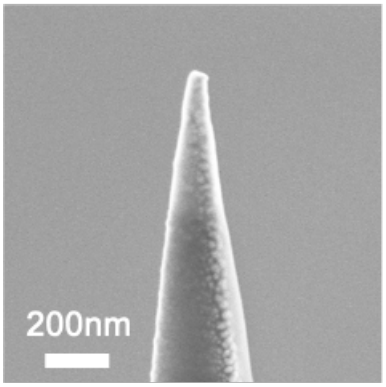

Figure 3.16: The typical SEM image of the E-beam evaporation coating tip with an average diameter of 70 nm.

Sputter coating

After 30 min of UV Ozone cleaning (UVC-150, Omniscience), 35 nm thick Ag is sputtered (SPT-20, Coxem) on the cantilever (ATEC-CONT, Nanosensors) at 6 mA current flow. The coating process is conducted at the pressure of 10^{-2} Torr. The average diameter of the tip is about 80 nm. The SEM image of the typical E-beam coated TERS tip is shown in figure 3.17.

3.4.1 Enhancement factor

We calculate the enhancement factor (EF) to quantify the performance of the tip fabricated by three tip fabrication methods. The enhancement factor for the TERS is defined as equation (3.15). Where, $I_{\text{tip-in}}$ is the intensity of the tip-enhanced Raman signal, $I_{\text{tip-out}}$ is the intensity of the micro-Raman signal, A_{FF} is the far-field beam spot, and A_{NF} is the near-field beam spot.

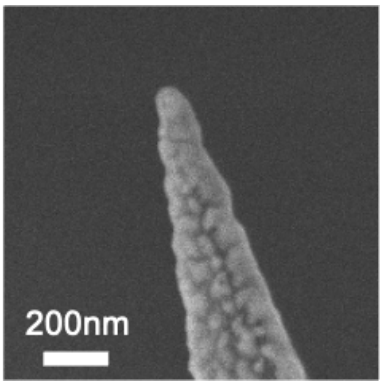

Figure 3.17: The typical SEM image of the sputter coating tip with an average diameter of 80 nm.

$$\mathrm{EF} \cong \frac{I_{\text{tip-in}} - I_{\text{tip-out}}}{I_{\text{tip-out}}} \cdot \frac{A_{\mathrm{FF}}}{A_{\mathrm{NF}}} \tag{3.15}$$

Thin silver film is used as a substrate in enhancement factor measurement. 4-mercaptophenol (4-mph) is coated on the metal film as an enhancement indicator. $I_{\text{tip-out}}$ is measured at $d \sim 5\mu m$, $I_{\text{tip-in}}$ is measured at the set-point of $> 99\%$ of the free amplitude. Both signals are measured at the same conditions except d. A_{FF} is $\sim \pi/4\mu m^2$, and the diameter of the far-field beam spot ($\sim 1\mu m$) is measured using an edge-scan method by scanning edge shape half-covered thin metal film. A_{NF} is calculated using FDTD simulation. The scheme and data for the E-beam evaporation tip are shown in figure 3.18.

As a result, $\mathrm{EF}_{\text{etching}} = 2.93 \times 10^4$, $\mathrm{EF}_{\text{sputter}} = 1.9 \times 10^5$, and $\mathrm{EF}_{\text{E-beam}} = 2.51 \times 10^5$ for the peak at 1100 cm^{-1} (left red arrow in figure 3.18). The enhancement factor is averaged for three different tips at least. Though $\mathrm{EF}_{\text{sputter}}$ and $\mathrm{EF}_{\text{E-beam}}$ are not much different, the E-beam evaporation tip is used in

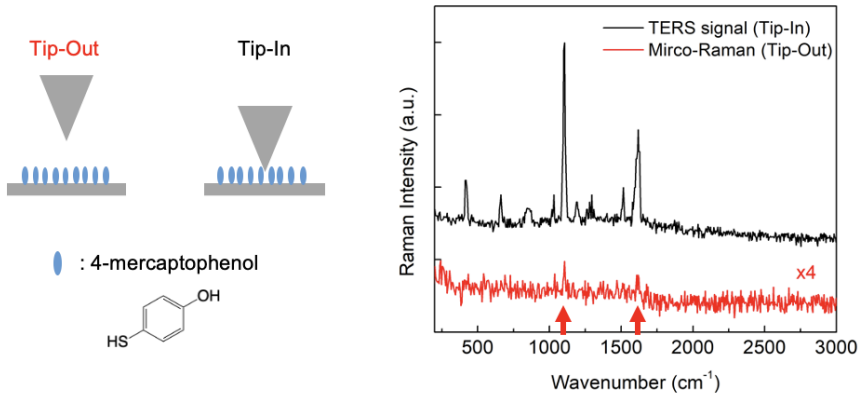

Figure 3.18: Measurement of the enhancement factor. (left) The tip-out signal and the tip-in signal are measured on the substrate coated with the self-assembled monolayer (SAM) (right) Measured TERS signal (tip-in) (black) and Micro-Raman signal (tip-out) (red) of the E-beam evaporation tip.

the main experiment because the impurity signal of the sputter tip is much higher than the E-beam tip. It is because sputter coating is conducted at a lower vacuum condition of 10^{-2} Torr than the vacuum condition of the E-beam evaporator of about 10^{-6} Torr.

3.5 Sample preparation

Mica

The muscovite mica (SPI supply) is glued to the cover glass with the adhesive (Loctite 420). And the upper mica sheets are removed by tape cleaving to make a thin and transparent substrate. The Raman signal of the adhesive and the substrate are measured to confirm that there is no overlap in the Raman

signal between the substrate and the sample (water) in the range of 3000 cm^{-1} $\sim$ 3600 cm^{-1}, where the OH-stretching band signal of water is observed. (figure 3.19) The thickness of the cover glass, the adhesive, and the mica are 170 μm, $\sim$ 10μm, and 50 $\sim$ 90μm, respectively. Though there is a small peak from adhesive at 2950 cm^{-1}, and a broad bump from 3000 cm^{-1} to 3400 cm^{-1} in the blue curve in figure 3.19, the intensity of the Raman signal of the OH-stretching band of water is not affected because the blue curve in figure 3.19 is measured at the interface between mica and adhesive with much higher laser power of 5 mW.

Freshly cleaved mica has a very high surface potential of -10 V or less due to the surface-charge imbalance. However, the surface charge is rapidly neutralized within a few minutes after the cleaved mica is exposed to air. Therefore, this charging effect is negligible in our experiment because we discharged the mica by stabilizing it in a closed chamber in ambient conditions for at least 3 hours before experiments.

To check the surface roughness of the mica, the scanning image of the mica sample obtained by a commercial AFM (NX-10, Park Systems) is shown in figure 3.20. The measured root-mean-square roughness is 0.041 nm.

Silver substrate

A thin noble metal coating less than a few tens of nanometers on the substrate has an island form rather than a uniform metal film. The adhesion layer is needed to prevent forming of metallic island film in thin film coating. Chromium (Cr) is one of the most widely used adhesion layer materials.

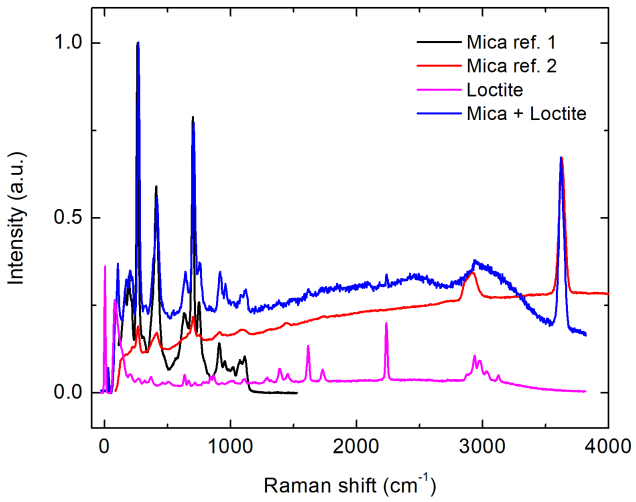

Figure 3.19: Raman spectrum of Mica substrate. The black and red spectra are the short-range Mica reference data and the broad-range Mica reference data, respectively. The two reference spectra are downloaded from https://rruff.info/Muscovite/R040108. The violet spectrum is the Raman signal of cured Loctite. The blue spectrum is the Raman signal of the Mica at the Mica-Loctite interface.

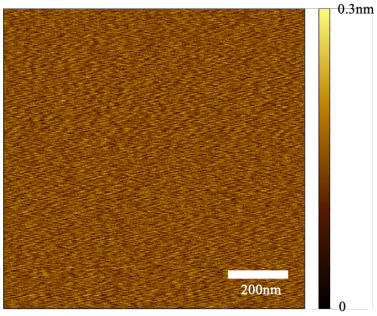

Figure 3.20: Mica height image measured by the commercial AFM.

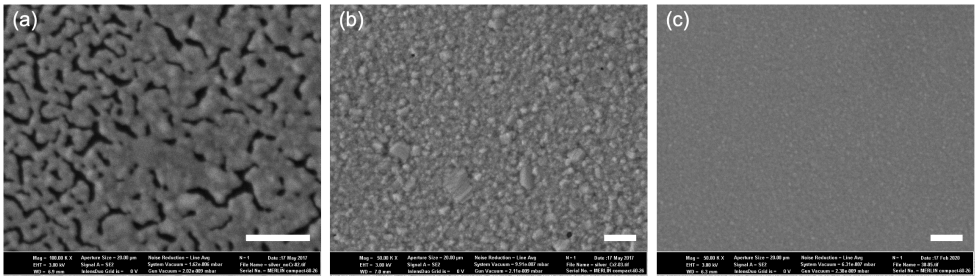

Figure 3.21: SEM images of metal films. (a) bare silver coating of 30 nm thickness. (b) 30 nm thickness silver coating with 2 nm Cr adhesion layer. (c) 30 nm silver coating with 2 nm Ge adhesion layer. All scale bar is 200 nm.

Germanium (Ge), Aluminium (Al), Titanium (Ti), and Tungsten (W) are also widely used for various purposes [103–106]. For the glass or silicone substrate, 3-mercaptopropyltrimethoxysilane (MPTMS) coating can be used instead of a metallic adhesion layer [107].

We have tested two materials for the adhesion layer, Cr and Ge, on the SiO_2 substrate. The substrate is rinsed with ethanol, acetone, and isopropanol in order. And the substrate is UV-Ozone cleaned for 30 min (UVC-150, Omniscience) before metal coating. The adhesion layer of $\sim$ 2 nm thickness is coated with the E-beam evaporator at 10^{-6} Torr at the rate of (value) nm/s. And the silver film of $\sim$ 30 nm thickness is coated with the same equipment without breaking the vacuum conditions. The coating rate and the thickness of the metal films are monitored with the quartz crystal microbalance (QCM).

The SEM images of coated metal films are shown in figure 3.21. The island configurations in the thin bare silver film are clearly shown. At the same thickness, the island film is disappeared with the adhesion layer. However, the

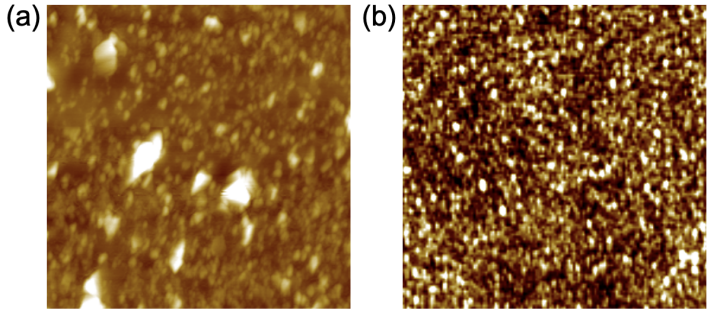

Figure 3.22: AFM height images of thin silver film with an adhesion layer. (a) a silver film with a Cr adhesion layer. (b) a silver film with a Ge adhesion layer. Scanning image size is both $1\mu m \times 1\mu m$.

surface roughness of metal film with different adhesion layers is obviously different, thin silver film with a Ge adhesion layer has a smoother surface. The scanning image of the thin silver film is shown in figure 3.22 to measure the surface roughness of films. The measured root-mean-square roughness of silver film with Cr adhesion layer and silver film with Ge adhesion layer are 0.639 nm and 0.091 nm, respectively.

Chapter 4

Hydrogen bond network of nano-confined water

Some of the figures and texts in this chapter are adapted from:

Hwang, J., Shin, D., Lee, M., Deveney, B. T., Zhang, X., & Jhe, W. Origin of ice nucleation: A quantified nano-confinement study at room temperature (2022) *Science* - Under review

4.1 Introduction

As mentioned in Chapter 1, the ordered structure of water within the confinement has been reported in various experiments and simulations. In tip-based experiments [18–21], ordered structure within confinement is confirmed by observing molecular layered structure in terms of force or viscosity oscillation. Unlike a confined simple liquid which shows a phase transition through very sharply increased viscosity [108, 109], the viscosity of confined water shows a

relatively slow increase in viscosity. This experimental observation may indicate the structure of confined water is not fully ordered structure. But because of the instrumental limitations, the exact hydrogen bond structure of confined water has not been identified in tip-based experiments such as AFM and SFA.

Meanwhile, spectroscopy-based experiments [24–27] also study the structure of confined water in various conditions. However, the spectroscopic experiments alone are also insufficient to obtain a holistic understanding of the hydrogen bond structure of confined water due to the difficulties of precise system control in spectroscopy-based experiments. Hence, we establish tip-enhanced Raman spectroscopy (TERS) which combines atomic force microscopy with confocal Raman spectroscopy for simultaneous measurement of the hydrogen bond network information and the mechanical properties of confined water.

This chapter is structured as follows. Our attempt to investigate the hydrogen bond network of confined water using SERS is introduced. The limitations of SERS-based experiments are explained, and we design our experiment to overcome limitations using TERS. Then our results are presented after introducing the experimental procedure. The Raman spectrum of the OH-stretching band signal of confined water is assigned in two different perspectives, the spectral assignment, and the spatial assignment. The meaning of the fitted Gaussian curves of the Raman spectrum is clarified from the peak assignment. Based on the peak assignment, the behavior of peaks in the OH-stretching band is discussed. After that, the experimental technique for precise measurement is explained such as the determination of the contact point, the volume of the nanomeniscus with respect to the 'hotspot' size, the relative humidity (RH)

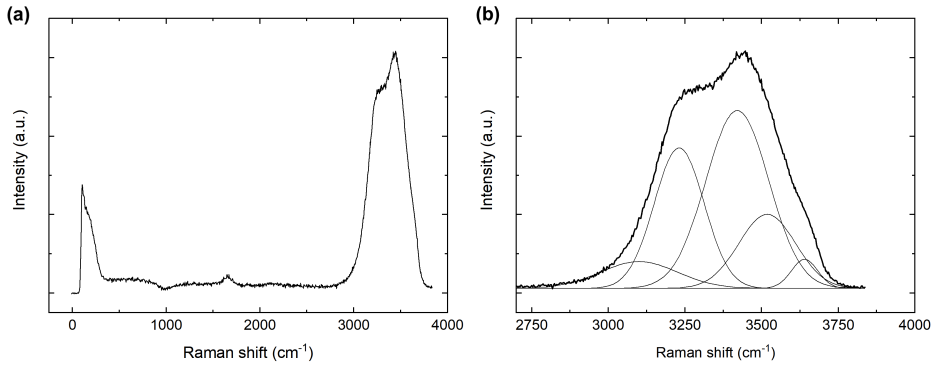

Figure 4.1: (a) The full spectrum of bulk water at room temperature. (b) The OH-stretching band signal of bulk water. The spectrum is fitted with five Gaussian curves, DAA, DDAA, DA, DDA, and free-OH water, respectively.

dependent behavior of the nanomeniscus, the tip dependence of the Raman spectrum, and data analysis methods.

Raman signal of bulk water

The Raman signal of water can be separated into three parts [110], the translational band including the lattice vibrational band at less than 500 cm^{-1}, the OH-bending band near 1600 cm^{-1}, and the OH-stretching band at 3000 $\sim$ 3600 cm^{-1}. (see figure 4.1) There are 5 or 6 small peaks in the translational band at room temperature or at a higher temperature. The signal intensity near 250 cm^{-1} in this band becomes larger and their bandwidth becomes narrower at a lower temperature, which is called the lattice vibrational band. The OH-stretching band consists of five main peaks, DAA ($\sim$ 3090 cm^{-1}), DDAA ($\sim$ 3240 cm^{-1}), DA ($\sim$ 3420 cm^{-1}), DDA ($\sim$ 3510 cm^{-1}), and free-OH water ($\sim$

3620 cm^{-1}), where D is a donor and A is an acceptor of the hydrogen bond. At a lower temperature, the OH-stretching band is red-shifted with a narrower, larger DDAA peak and a smaller DA peak.

4.2 Previous works on HB network of confined water

We conducted a preceding experiment using SERS before measuring the hydrogen bond network of single confined water using TERS. In general, the enhancement factor of SERS is much higher than TERS because the number of 'hotspot' in SERS is much more than in TERS. In addition, since the number of water molecules within the SERS substrate is higher than within the tip-substrate gap in TERS, the hydrogen bond network can be more easily measured. We created the SERS substrate through silver islands film through a thin silver film coating. The thin film SERS substrate is coated with two different self-assembled monolayer (SAM) molecules, 4-methylbenzenethiol which is a hydrophobic SAM, and 4-mercaptophenol which is a hydrophilic SAM. The Raman signal is measured in the dry state and measured again within the water. By lowering the focal point sufficiently near the surface and lowering the power, the OH-stretching band of the interfacial water was measured and it was confirmed that the signal changed from that of bulk water. (figure 4.2) Although it clearly shows a substantially different signal from the Raman signal of the bulk water, it was hard to say a distinct HB network due to a low SNR of the signal.

Therefore, we used aggregated silver nanoparticles as a SERS substrate

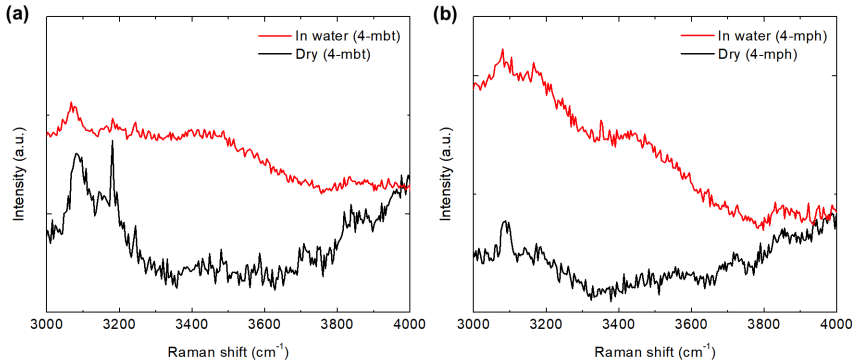

Figure 4.2: The OH-stretching band signal of water on SAM-coated silver island SERS substrate. (a) 4-methylbenzenethiol (4-mbt) is coated on the SERS substrate. (b) 4-mercaptophenol (4-mph) is coated on the SERS substrate.

to further increase the enhancement factor. To form nano-confined water in the NPs aggregated substrates, the water droplet with dense NPs is deposited and evaporated on the glass substrate. However, the initial results obtained were similar to the signals obtained from the metal island SERS substrate. We solved this problem by ultra-purifying the NPs solution to eliminate impurities such as nitrate anion, sodium cation, and citrate anion. After purifying several times to remove impurities inside the solution, we observe two clear peaks in the OH-stretching band at room temperature [25].

The two peaks are located at 3340 cm^{-1} and 3493 cm^{-1} and compared to the Raman signals of bulk water, their peak positions are similar to those of DDAA and DA peak in bulk water, respectively. The overall OH-stretching band signal of nano-confined water is blue-shifted and has a narrower bandwidth than the bulk water. In addition, when the NPs sample is heated to 393 K, the first

peak (3340 cm^{-1}) disappeared and no peak shift was observed in temperature change. Through this, the 3340 cm^{-1} peak is assigned to DDAA water forming a meniscus, and the 3493 cm^{-1} peak to DA water, which is strongly surface bounded water. By comparing the DDAA peak position of all the other known ice phases, we also found that the hydrogen bond network of confined water is very similar to the Ice-VII, known as a high-pressure ice phase at room temperature. A similar Raman signal is observed in NPs samples with thin coatings with the self-assembled monolayer (SAM), Pt, and Au. Therefore, it is suggested that the unique HB network of ice-VII in nano-confinement can be the general behavior of confined water under strong confinement.

In another previous study, the hydrogen bond network of water inside CNT was measured [6]. The infrared spectroscopy is performed using a mixed diameter of SWCNTs samples of 0.7 to 2.1 nm while changing the relative humidity (RH) from the dry state to RH 100%. The degree of confinement is indirectly manipulated by controlling environmental RH, from the fact that the probability to occur capillary condensation is higher at smaller diameter CNTs. As a result, at a low humidity of about 30%, an ice-like signal is observed at a similar peak position of DDAA water, but at a high humidity of about 100%, a liquid-like signal is observed at the same peak position. Strangely, the free-OH signal intensity is always larger than other signals regardless of the RH. This is a unique characteristic of the CNTs, the strong free-OH signal appears because the wall of CNT does not have bonding with water molecules. Since confined water has a very high surface-to-volume ratio, the nature of the surface is very important in determining the hydrogen bond network of confined water.

limitations

In general, most spectroscopy studies have a common disadvantage in that the control of the degree of confinement of the system with nanoscale precision is very difficult [6, 24, 25, 111, 112], while the most important in experiments about confined water is to control confinement. For example, in the case of the aggregated nanoparticle sample, the distance between the nanoparticles cannot be adjusted and information about the exact distance between them cannot be measured because there are numerous particles. Since there are no criteria for the degree of confinement in such experimental methods, it is impossible to know whether the degree of confinement changes with external parameter changes such as temperature, electric field, and surface properties. In addition, the spectroscopic method alone cannot measure physical quantities related to changes in the hydrogen bond network. So, we decided to introduce TERS to overcome these limitations. In SPM-based experimental equipment, there is not only a criterion for the degree of confinement, but also precise control is possible. And, the physical and chemical properties of the system can be measured with a probe.

4.3 Experimental procedure

Laser alignment procedure

In TERS experiment, the tip and the laser have to be aligned. When the low magnification objectives are used, the laser alignment is quite simple [113]. However, we align the tip and the laser in two steps, the coarse alignment, and

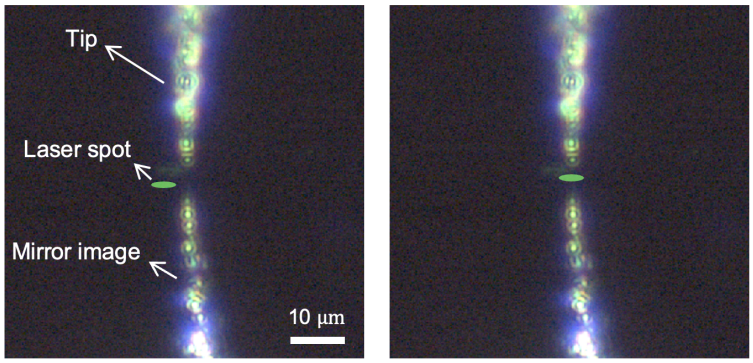

Figure 4.3: Manual coarse laser alignment. the diameter of the laser spot is 1 μm. The laser spot in the figure is for the understanding of laser alignment.

the fine alignment. For the coarse alignment, as shown in figure 4.3, after the tip approached the substrate in a few μm, the laser spot is manually aligned by moving the objective lens using a picomotor in x-, y-, and z-axis, respectively. Typically, after the coarse alignment, the distance between the tip and the laser spot is less than 5 μm, which is still much larger than the beam diameter of 1 μm. In the fine alignment process, as shown in figure 4.4, the laser scanning image of about $5 \times 5\,\mu m^2$ is obtained to find the exact tip position. During the scanning, the laser power is reduced to a few $\sim$ nW scale because the scanning image doesn't have to be the Raman signal imaging. The contrast of the reflected laser image is enough to recognize the tip position due to the high reflectance of the metal tip. Notice that the tip is located in the red area in figure 4.4.

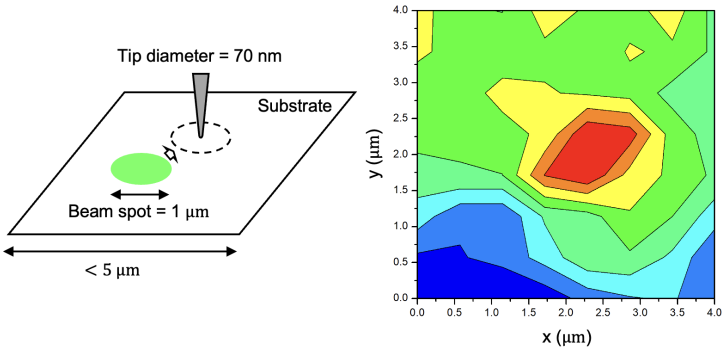

Figure 4.4: Fine laser alignment. (left) The tip and the laser spot are still misaligned within a few m after the manual alignment. (right) laser scanning image. The tip is located in the red area.

Experimental procedure

The experimental schematic is shown in figure 4.5. We study the structural behavior of water confined between a sharp silver tip and a substrate. We use a mica substrate, which serves as an atomically flat and hydrophilic surface on which a meniscus can be easily formed by capillary condensation when the tip-substrate distance, d, is in the nanoscale. To probe the mechanical properties, we employed the quartz tuning-fork (QTF) as a sensitive piezoelectric force sensor having a high quality factor ($\sim 10^4$) and a high stiffness ($\sim 10^4$ N/m), which also allows precise control of confinement in terms of d. The QTF is operated in shear mode at its resonance frequency ($\sim$ 32745 Hz) with 0.29 nm oscillation amplitude and at low relative humidity ($\sim$ 1 %) and room temperature (see Section 4.5 for RH dependence force-distance curves). We measure the changes in the amplitude and phase induced by the confined water [51], which are con-

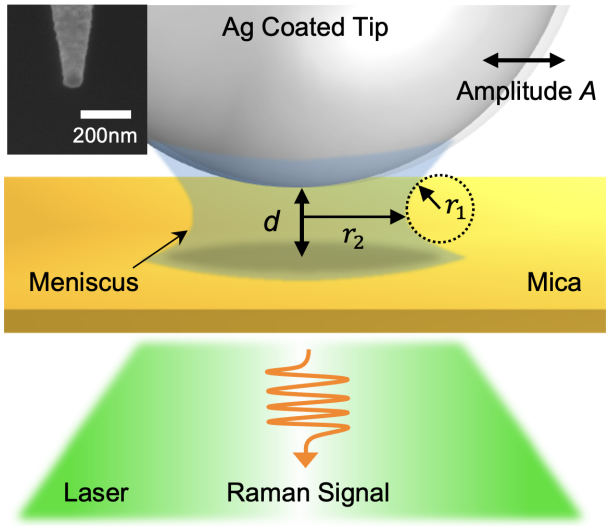

Figure 4.5: Schematic of a water nano-meniscus capillary-condensed in the tip-mica gap. The tip oscillates with amplitude A. r_1 and r_2 are the two principal radii-of-curvature of the meniscus. The inset shows the SEM image of a typical 80 nm-diameter silver-evaporated cantilever tip.

verted to the elastic (k_{int}) and damping (b_{int}) interaction response of water, as well as the corresponding mechanical relaxation time [20,114], $\tau_r = k_{\text{int}}/b_{\text{int}}\omega^2$, an indicator of the solid-like property.

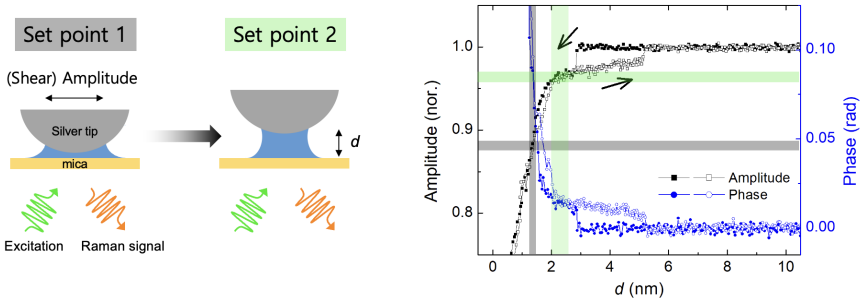

Figure 4.6: Description of the experimental procedure. Obtain approach curve, operated at its resonance frequency ($\sim$ 32745 Hz). Measure the Raman signal while maintaining the tip-substrate distance through PID in amplitude modulation mode at a certain set-point. Change to the next set-point and measure Raman signal again.

4.4 Zero-point determination

The zero-point ($d = 0$) is defined with reference to the contact point or the point of maximum energy dissipation. The energy dissipation, the integration of the non-conservative force over one period, is a characteristic mechanical parameter in the dynamic AFM. The energy dissipation per cycle is given by [51],

$$\frac{E_{\text{dis}}}{kA_0^2} = -\frac{\pi}{Q}\left[\frac{A}{A_0}\cos\theta - \frac{\omega}{\omega_0}\left(\frac{A}{A_0}\right)^2\right] \tag{4.1}$$

where A and θ are the amplitude and phase of the probe, respectively, A_0 is the peak amplitude at resonance, ω_0 the resonance angular frequency, ω the operating angular frequency, Q the quality factor of the probe, and k the stiffness of the probe. For our QTF, $A_0 \sim 0.29$ nm at $\omega/2\pi \sim 32745$ Hz, $Q \sim 9000$, $k \sim 43000$ N/m. The typical data of the approach curve and the corresponding dissipation energy are shown in figure 4.7. Though the absolute standard for measurement of a contact point in AFM still lacks [115], we have defined the contact point as the position of maximum energy dissipation (or maximum non-conservative interaction), which is one of the important criteria to identify the surface properties using AFM [116].

Then, because of the tightly bounded monolayer thickness of water on the hydrophilic surfaces, the zero-point d_{zero} can be defined as $d_{\text{zero}} = d_{\text{contact}}$ - 0.6 nm although there can be slightly different definitions of the zero-point [117, 118]. In addition, there are inevitable experimental uncertainties in determining the zero-point such as the elasticity of the materials and the meaning

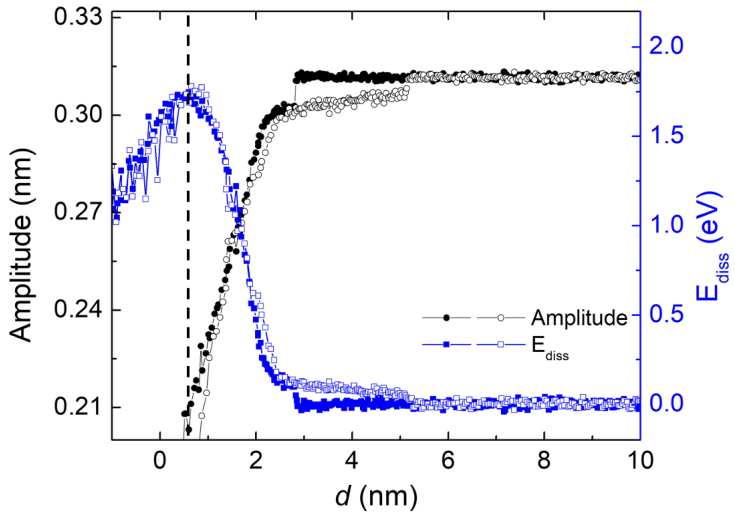

Figure 4.7: Energy dissipation and tip-oscillation amplitude versus d. The contact-point is determined as the point of maximum energy dissipation, from which the zero-point ($d = 0$) is defined with reference to the contact-point as $d_{\text{zero}} = d_{\text{contact}}$ - 0.6 nm.

of 'contact' at the molecular scale. Nonetheless, by comparison to the previous studies [117, 118], we estimated there can be at most a maximum error of $\pm$ 0.5 nm. Moreover, the specific choice of the zero-point affects only the values of d_{bound} since it has the same amount of error as d_{zero}. Therefore, our interpretation of the simultaneously measured Raman signal of the nano-meniscus and the relaxation time is not altered regardless of how the zero-point is defined within experimental error.

4.5 RH dependent force-distance curves

We systematically confirm the effect of coalescence caused by a thin film of water on the surface. We assume the pre-adsorbed water film on mica is a monolayer thick ($\sim$ 0.3 nm) as is confirmed in the previous experiment [118]. However, it has been also known that the thickness of water film on silver is thicker than that on mica [119]. The thick pre-adsorbed water film causes two problems in precise distance control. First, if the size of the nano-meniscus is larger than the 'hotspot' size, the interpretation of the Raman signal would become abstruse because the signal would come only from a part of the meniscus. Second, QTF could be easily saturated, due to its high Q-factor nature, even by a small force from the thick pre-adsorbed water film. In order to avoid such problems, we had to create a nano-meniscus as small as possible by reducing the relative humidity (RH).

The typical approach curves obtained at different RH, the measured critical distance d_c where the tip-oscillation amplitude drop occurs, and the corresponding amplitude magnitude at d_c are shown in figure 4.8. All the amplitudes are normalized by their free oscillation amplitude. At high RH, all parameters such as the amplitude drop, the measured d_c, and the rupture distance also increased, obviously indicating the increase of the thickness of pre-adsorbed water film. Constructing a quartz-mica (tip-mica) system [118] for comparison, the results are very different because the measured d_c and the rupture distance are approximately 1.2 nm and 2.2 nm, respectively at 10% RH. This difference shows that the pre-adsorbed water film developed on the silver surface is thicker than

that on mica.

Additionally, the calculated d_c (< 0.6 nm) from the Kelvin equation at 1 $\sim$ 10 % RH is much shorter than the measured d_c (see figure 4.8). This is because the nucleation effect and the coalescence effect are combined in the measured d_c, but even with reference to the previously reported thickness of water film ($\sim$ 1 nm) on silver [119] at given RH, there is still a large discrepancy between the calculated d_c and the measured one above 5 % RH. There are several possibilities, but not clarified, causes such as the uncertainty of zero-point determination, the laser trapping effect [120] and the interfacial tension effect, that may contribute to such discrepancy. In our experiments, we conduct all the experiments at 1.2 $\pm$ 0.5 % RH because (i) it is confirmed there is no significant change in the measured d_c below 2 % RH, and (ii) the volume of the meniscus calculated by the Young-Laplace equation at 2 % RH does not exceed the 'hotspot' size (See figure 4.9).

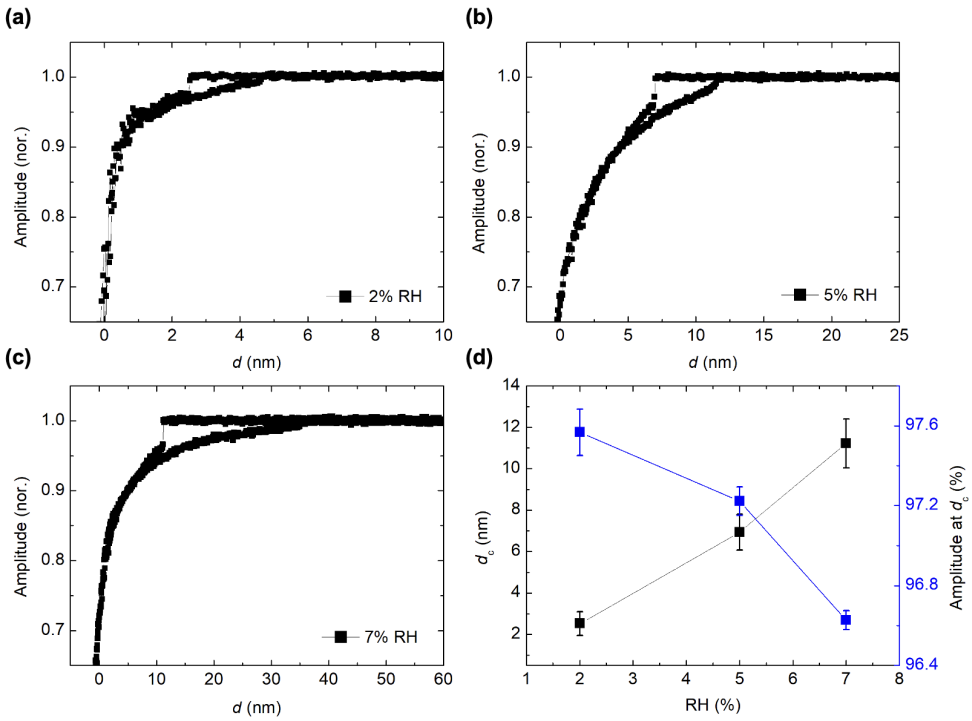

Figure 4.8: (a)-(c). Normalized approach curves at three different relative humidity (2%, 5%, and 7%, respectively). Both the distance at which water vapor condenses upon the approach of the tip to the substrate and the distance at which the water bridging the tip and the substrate ruptures upon retraction of the tip t become longer as RH increases. (d) The measured critical distance d_c (i.e. distance where a sudden drop of the tip-oscillation amplitude occurs) and the oscillation amplitude at d_c (i.e. amplitude drop measured at d_c) against the relative humidity. The error bars are estimated from measurements with three different tips.

4.6 Comparison of 'hotspot' size to nanomeniscus

Meniscus profile

The meniscus profile is calculated by solving the Young-Laplace equation under the given conditions [31]. The contact angle between mica and water and the contact angle between silver and water are both assumed to be 0 degrees. This assumption is achieved based on the contact angle measurements. Mica is a well-known hydrophilic surface, and a flat silver surface is also a hydrophilic surface immediately after metal film coating. However, the hydrophobicity of silver surface increases over time because of the growth of the silver oxide after exposed to the air. The contact angle of bare flat silver surface immediately after coating is less than 10 degrees, and it is increased and saturated up to 35 degrees after about 3 hours. The results are shown in figure 4.9 with electric field simulation results.

FDTD simulation

We calculate the electric-field distribution at the apex of the tip using the COMSOL Multiphysics simulation. The sharp tip under proper conditions produces an enhanced local electric field due to the plasmonic resonance, which results in high signal-to-noise ratio compared to traditional Raman spectroscopy. In our experiments, the silver tip we use provides the enhancement factor (EF) of over 2.5×10^5. We also derive the water-meniscus profile between two solid surfaces using the Young-Laplace equation, which describe the pressure difference across the non-planer liquid interface [31], at the same conditions with

COMSOL simulation. The calculated size of the optical 'hotspot' is comparable to the water-meniscus size itself (figure 4.9). This indicates that the Raman spectra that we obtain cover the entire spatial profile of water confined in the tip-substrate gap.

The finite-difference time-domain (FDTD) method is used to calculate the 'hotspot' size near the TERS probe using the COMSOL Multiphysics. The probe model has a cone-shaped Si core of a 1:4 aspect ratio with a tip radius of 10 nm, and 30 nm thick Ag coating is applied on the outside. We set the fused quartz as a substrate and performed the simulation while varying d from 0.05 nm to 4.5 nm. As a background initial wave, the plane wave at 532 nm wavelength with its wave vector parallel to the substrate is employed. The refractive index of Si [121], Ag [122], and fused quartz [123] are referred from each reference.

4.7 OH-stretching band signal of confined water

The typical force-distance curve and the corresponding OH-stretching band signal of confined water are shown in figure 4.10 and figure 4.11, respectively. We characterize three distinct regimes of d. The first is the non-contact regime [i]; no condensed water is formed in the nano-gap, the amplitude and phase signals remain constant, and thus no Raman signal from confined water is observed. The next is the weak confinement regime [ii]; a sudden drop appears in the amplitude signal at $d \sim 3$ nm due to the capillary condensation of water in the gap. Note that water remains condensed between the tip and the substrate

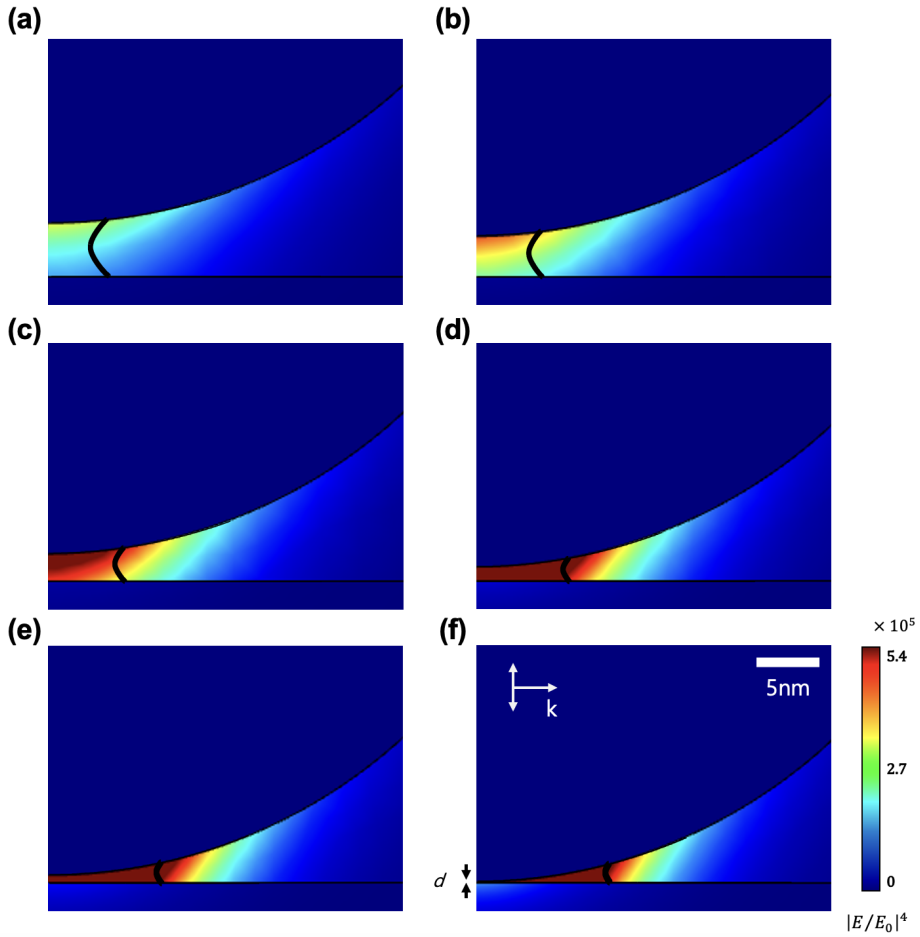

Figure 4.9: FDTD simulation results of the electric field distribution at the apex of a silver coated tip and the respective nano-meniscus geometry (thick black solid line) calculated by the Young-Laplace equation. The tip-substrate distances are 4, 3, 2, 1, 0.5, and 0.05 nm, respectively, in (a)-(f).

even when the tip is retracted to ~ 4.5 nm. That is why we measure the Raman signal at each d during stepwise retraction in this regime. The last is the strong-confinement regime within ~ 2 nm from the surface [iii]; as the tip approaches the substrate, there are considerable changes in the amplitude-phase signals and the corresponding Raman spectra even at a small change of d until contact with the mica. In each spectrum, the presence of free-OH signal at ~ 3610 cm^{-1} is confounded by the free-OH signal of the mica. There is also a CH_n peak at ~ 2900 cm^{-1}, reflecting the unwanted impurity molecules which may originate from contamination during the tip-fabrication process or during the chamber-purging process. Each of the spectra we obtain is fitted with seven Gaussian curves, while only five of them are attributed to the confined water as shown in figure 4.11. The free-OH signals and the CH_n signals are subtracted out and omitted from the figures in the text for a clear view.

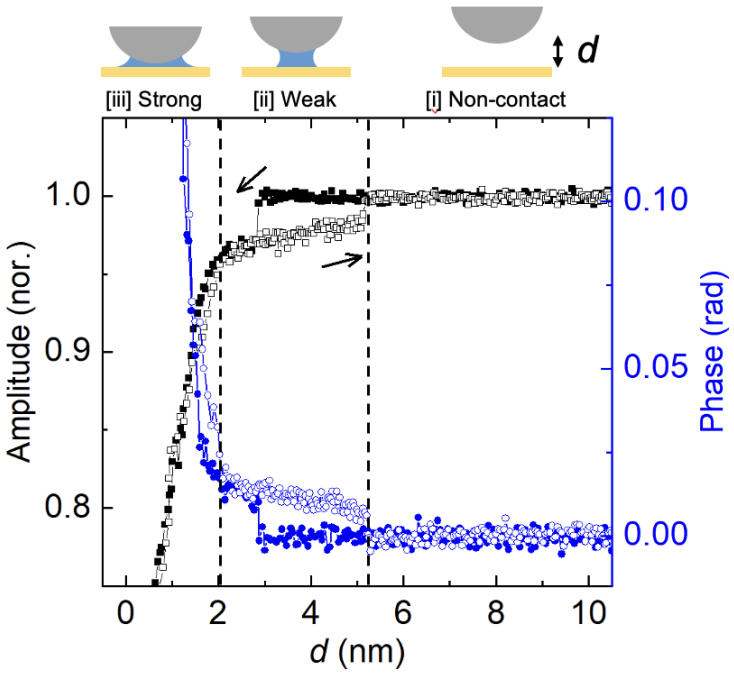

Figure 4.10: Typical amplitude and phase response of QTF during tip approach (filled symbols) and retraction (open symbols). Nanomeniscus is formed when a sudden amplitude drop occurs at 2.7 nm by capillary condensation. The confinement condition is separated into three regimes according to d, non-contact regime, weakly confined regime, and strongly confined regime.

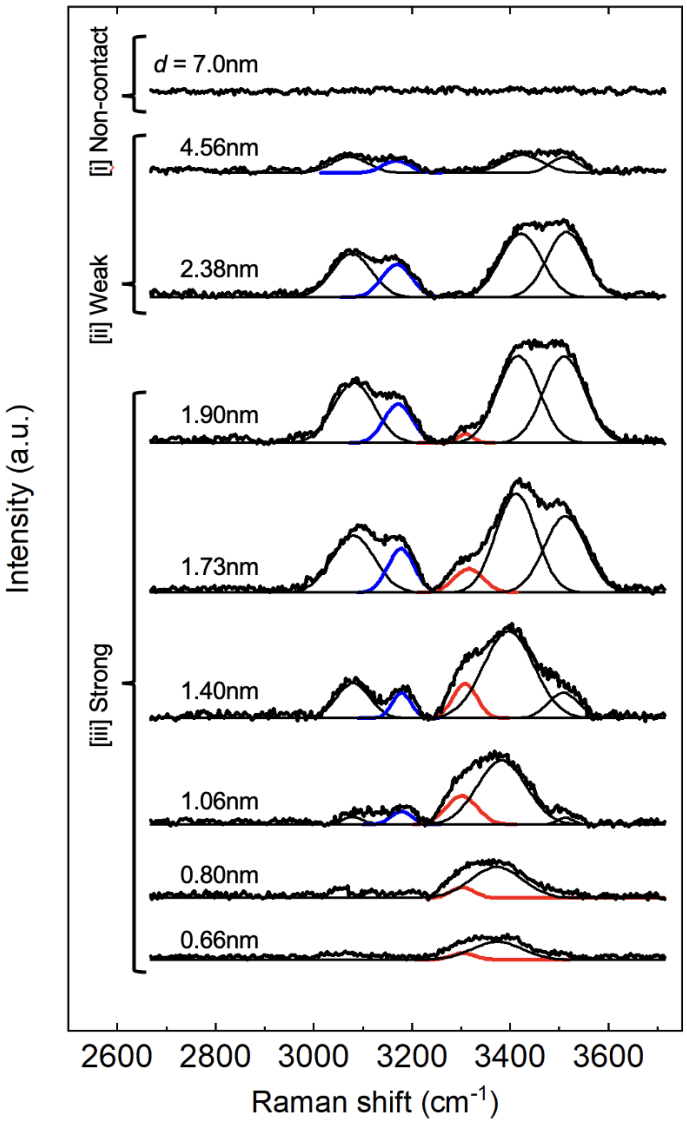

Figure 4.11: The Raman spectra of the OH-stretching band are measured at each d. The error bar of each d is omitted for a clear view. Each spectrum is fitted with 7 Gaussian curves including the OH-stretching band signal of confined water, CH_n signal at 2900 cm^{-1}, and free-OH signal at 3600 cm^{-1}. The CH_n signal and the free-OH signal are omitted for clarity and only 5 fitted curves are shown.

4.7.1 Full spectrum

QTF is calibrated using the energy-balance methods [92] ($\alpha = 0.66$ Å/mV, amplitude = 0.29 nm at $\omega/2\pi$ = 32,745 Hz). The chamber is purged with dehumidified nitrogen gas (RH $<$ 1 ppm) before experiments. Deionized water is used to set the relative humidity by controlling the flow rate of two gases, pure nitrogen gas and water-saturated gas. Raman measurements are conducted with 50 μW laser power to minimize photo-induced reactions. Relatively high power (5 mW) is only used to measure the bulk-water Raman signal. Each spectrum is measured for 3 min while the distance d is kept by AFM-PID control. Raman signals are baseline-corrected by the improved asymmetric least squares (IAsLS) method. OH-stretching band signal is fitted with 7 Gaussian curves with Origin Pro. Two fitted curves of free-OH signal and CH_n signal is omitted in main figure by subtracting their Gaussian curves from raw data.

The full spectrum of the OH-stretching band including two signals, CH_n at $\sim$ 2900 cm^{-1} and free-OH at $\sim$ 3630 cm^{-1} (figure 4.12), which are omitted in the main text. The arrow indicates the direction of the tip approach. It is easily noticed that there are both CH_n and free-OH signals in the uppermost spectrum of figure 4.12 which are measured in the non-contact regime. Because of the strong free-OH signal from mica, it is not possible to distinguish it from the free-OH signal from confined water. And the source of the CH_n peak is the unwantedly captured impurity from the air during the experiment. Examples of organic compounds in the air include propane, methane, cyclohexane, benzene, 1,2,4-trimethylbenzene, trichloroethylene, 1,2-Dichloroethane,

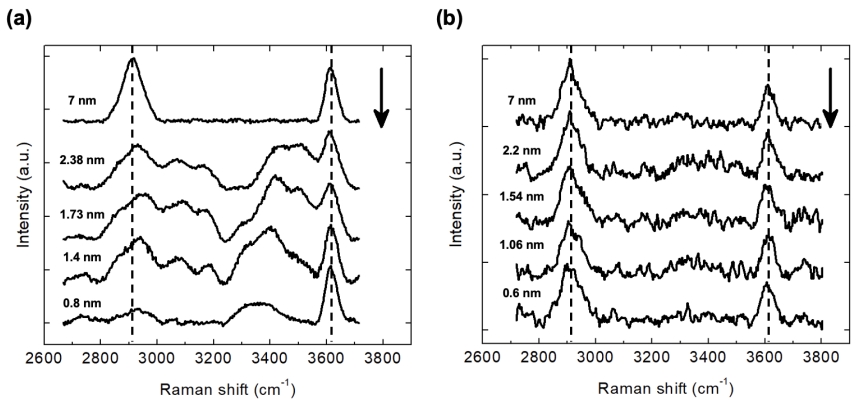

Figure 4.12: Full spectrum of the OH-stretching band signal including the CH_n and free-OH signals. (a) The Raman signal obtained by the high ($\sim 10^5$) EF tip. The peak position and the intensity of the CHn signal are changed due to the photobleaching effect. (b) The signal from the low ($10^2 \sim 10^4$) EF tip. The positions of both CH_n and free-OH signals are not changed versus d

and 1,2-Dichloropropane. These molecules are the possible sources of the impurity signal since there are no molecules that are intentionally injected into the chamber. The ratio of the effective Raman cross-section of the impurity signal [124] (CH_n) and the water OH-stretching band, Ω_{CH}/Ω_{OH}, is 1.28 12.33.

The number of impurity molecules is determined as follows. The measured spectra are separated into three parts, CH_n signal, OH group signal, and free-OH signal. The ratio of the spectral area of CH_n signal and that of the OH group signal A_{CH}/A_{OH} is multiplied by $2/n_{CH}$, where 2 is the number of OH hydrogens per water molecule and n_{CH} is the number of CH hydrogens per impurity molecule. We set n_{CH} as 12, the number of CH hydrogens of cyclohexane which has the highest Raman cross section among impurity molecules, because the exact impurity molecule is not determined. Then, the number of impurity molecules in the 'hotspot' is $N_{CH} = N_{OH}(\Omega_{OH}/\Omega_{CH})(A_{CH}/A_{OH})(2/n_{CH})$, where N_{OH} is the number of water molecules. The number of water molecules that consists of the nano-meniscus is determined by the rupture distance of the AFM force curve [114]. The volume of nano-meniscus is $\sim d_{Rup}^3$, where d_{Rup} is the rupture distance of nanomeniscus. The resulting estimate of the number of impurity molecules is $N_{CH} = 11 \sim 170$. Then surface density of impurity molecule on the tip surface is $\rho_A = 0.058 \sim 0.9$ molecule/nm^2.

We measured the Raman signals using both the high EF tip ($\sim 10^5$, figure 4.12.(a)) and low EF tip ($10^3 \sim 10^4$, figure 4.12.(b)). The enhancement factor is measured by comparing the TERS signal with the micro-Raman signal of bulk water. Notice that the CH_n signals in figure 4.12.(a) changed while the CH_n signals in figure 4.12.(b) did not, indicating that such a peak shift is caused by

the photoinduced effect on the tip [125].

4.7.2 Tip dependence

We have conducted the same experiment to check the tip dependence in Raman observation of the bcc structure using the tips fabricated by different methods; sputter coating and etching. The results are shown in figure 4.13. Similar to the main figures in the text, the CH_n signal and the free-OH signal are not shown. Although similar OH-stretching band signal is obtained using the sputter tip, it is difficult to obtain reliable results because it is fabricated in a low-vacuum condition. In particular, the bcc-structure signal of ice-VII is not obtained reproducibly with such a tip. It is because the proper confinement conditions are not made between tip and mica due to the large size of the silver chuck in the sputtering process and the resulting large tip roughness.

Notice that the fact that the peak at 3200 cm^{-1} did not decrease at small d indicated that the proper confinement is not established by the sputter tip. On the other hand, the bcc-structure signal is measured using the etching tip. As can be seen from the SEM image, this is considered as due to the corrugations of rough surface. Although the exact peak positions are not same as those obtained by the e-beam evaporation tip, it showed similar behaviours, implying that the HB structure of confined water is highly dependent on the confinement environment.

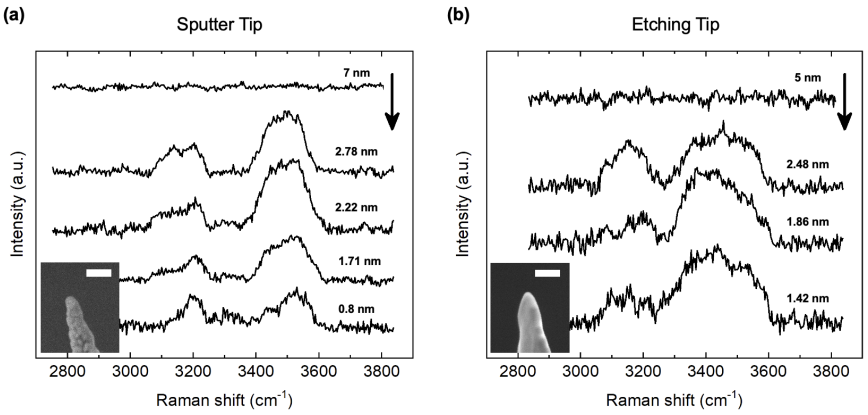

Figure 4.13: Typical Raman signal of confined water obtained by sputter tip and etching tip. The CH_n and free-OH signals are omitted for clear comparison. The arrow indicates the direction of tip approach. (a) The signal obtained by the Ag-coated tip using sputter. (b) The signal by the Ag-wire etched tip. Each inset shows the SEM image of the tip where the scale bar is 200 nm.

4.8 Peak assignment

4.8.1 Spectral assignment

As a reference, the Raman signal of bulk water is decomposed into five different water structures: DAA, DDAA, DA, DDA and free-OH, where D (A) stands for the HB donor (accepter). In the case of weakly confined water, we find a close agreement between the positions of the fitted Gaussian peaks and those of bulk water, and can identify clearly the four different water structures: DAA, DDAA, DA, and DDA. Here, the DDAA component corresponds to the tetrahedral DDAA, which is the unit structure of ice-I_h. Notice that the DDAA signal at 3178 cm^{-1} (blue peak in the lower panel of figure 4.14) is red-shifted with a bandwidth narrower than bulk water, indicating confined water exhibits the more ordered HB structure because its bandwidth and bond strength are closer to ice than liquid water. In fact, this behavior, which we observe at room temperature, is similar to that of supercooled water [126]. Comparing the specific DDAA peak at 3178 cm^{-1} and the corresponding bulk DDAA, we estimate the effective temperature of confined water is about 269 K (figure 4.15). This lowered effective temperature also supports the observation that confined water may have the ordered DDAA structure.

4.8.2 Spatial assignment

Interestingly, a new Raman peak begins to emerge near 3316 cm^{-1} as d decreases further and the water enters the strong confinement regime. This is shown in red in the lower panel of figure 4.14. Such a signal cannot be read-

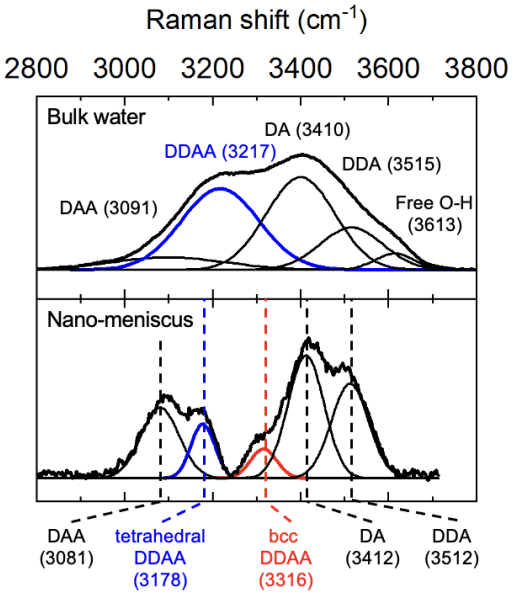

Figure 4.14: Comparison of the Raman spectrum taken at $d = 1.73 \pm 0.09$ nm and the normal Raman signal of bulk water taken at 300K.

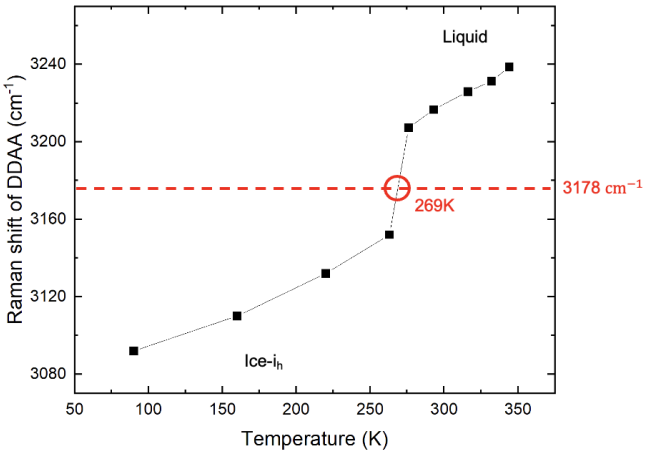

Figure 4.15: DDAA peak position of bulk water with respect to temperature [127, 128]. The red dashed line is the peak position of the tetrahedral DDAA in figure 4.11

ily matched with any of the known Raman components of bulk water. However, from the close correlation between the unassigned signal and the lattice-vibration band that is the low-frequency signal commonly observed in the ice phases as shown in figure 4.16, the unknown signal can be uniquely attributed to another ordered DDAA structure. To identify the exact structure, we compare our data with the DDAA peak positions of various ice phases (figure 4.17) since the DDAA is commonly used as a structural indicator of solid phase. Most of ice show the DDAA peaks located below 3250 cm^{-1}; however, ice-VII at high pressure and at room temperature shows a peak near 3310 cm^{-1} which is close to that of our new signal at 3316 cm^{-1}. Notice that although ice-VIII peak can also locate above 3250 cm^{-1}, it does not match with our experimental condition since ice-VIII exists in a much lower temperature range than ice-VII [129].

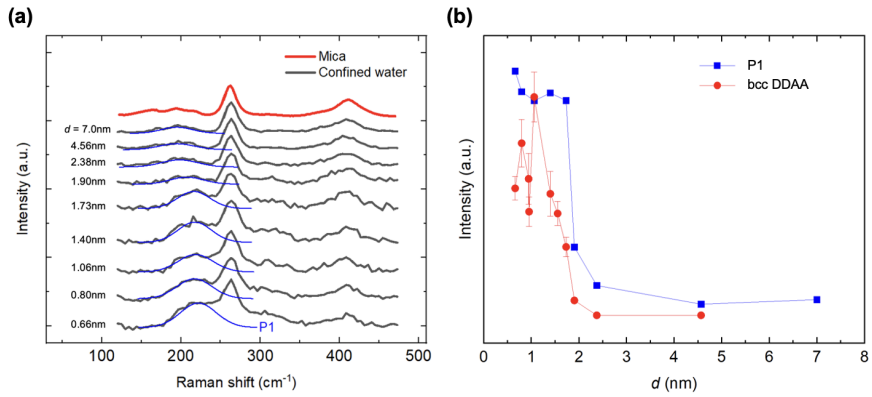

Figure 4.16: (a) Low-frequency signal versus d. The peaks near 265 and 410 cm^{-1} are attributed to mica [131] (red solid line). The peak attributed to the ice-VII structure near 210 cm^{-1} starts to emerge from 1.9 nm distance, indicating the solidity of confined water is enhanced. This peak is fitted with a Gaussian curve (P1, blue curve). (b) The intensity of P1 and bcc DDAA with respect to d.

Another high-pressure ice, ice-X, is excluded since the OH-stretching band is absent therein [130]. We therefore assign our new DDAA signal to the unit structure of ice-VII, i.e., bcc DDAA.

In bulk water, it is generally believed that different HB structures are uniformly distributed therein. However, confined water can compose of two separate spatial parts, an interface and an interior, as similarly discussed in previous studies such as CNT [6], Ice cluster [143], and Ag nanoparticle [25] experiments. Both simulations and experiments agree that the DDAA water occupies the interior of the confined water, while other kinds of water lie at the interface. In our confined water model, we subdivide the interfacial region to air/water in-

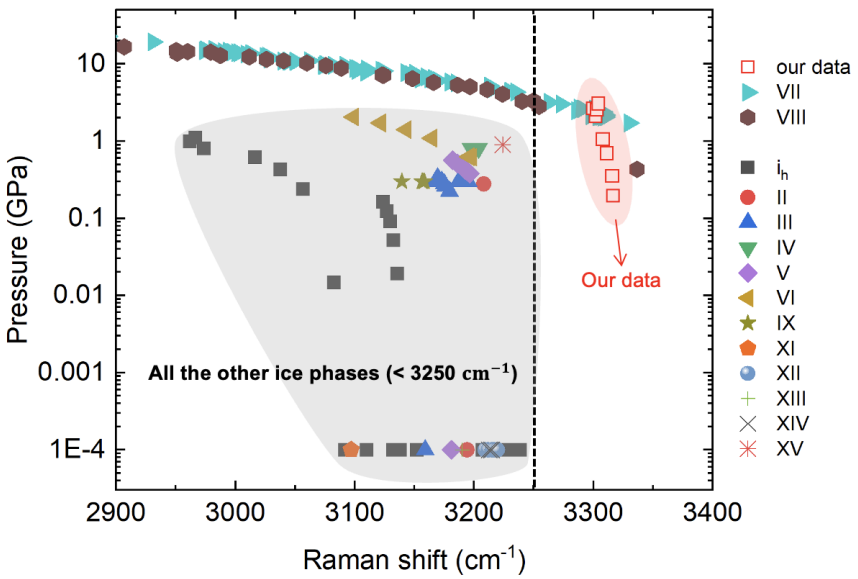

Figure 4.17: DDAA peak position of various ice phases (ice-Ih [132, 133], II [132, 134], III [132, 134, 135], IV [136], V [132, 134], VI [132], VII [137, 138], VIII [129, 130], IX [135], XI [139], XII [140], XIII [141], XIV [140], XV [142]) versus pressure. Our experimental data of bcc DDAA are also plotted (red open squares).

terface and solid/water interface. Therefore, we can divide the confined water into three parts as shown in figure 4.18; air/water interface (blue), solid/water interface (green), and interior water (red), where $t_{\mathrm{a/w}}$ denotes the thickness of air/water interface while $t_{\mathrm{s/w}}$ that of solid/water interface. To match three spatial parts with each HB structure, we fit our experimental data to our model by comparing the integrated Raman intensity of the OH-stretching band with that calculated using the meniscus profile and the EF calculation (see figure 4.9). The best fitting results are shown in figure 4.19.(a). According to our identification, the air/water interface consists of DDA and DAA water, the solid/water interface contains DA water, and the meniscus interior is occupied by tetrahedral DDAA and bcc DDAA. Note that $t_{\mathrm{s/w}}$ is independent of d and is about 0.32 nm, the monolayer thickness of water, in agreement with the results of the pre-adsorbed water layer on mica [18, 19, 118], whereas $t_{\mathrm{a/w}}$ is $2 \sim 3$ molecular thickness when $d > 1$ nm and of monolayer thickness when $d < 1$ nm.

4.9 Peak Behavior

4.9.1 Transition between two DDAAs

We observe the evidence of the structural transition between tetrahedral DDAA and bcc DDAA as shown in figure 4.20 and figure 4.21. The Raman shift and the normalized Raman intensity of each spectrum are presented in figure 4.20.(a) and (b), respectively, which show similar transition of molecular structure versus d. Here, the gray-coloured transition region lies between d of 1.06 ± 0.16 nm and 1.90 ± 0.12 nm. We find that the bcc structure domi-

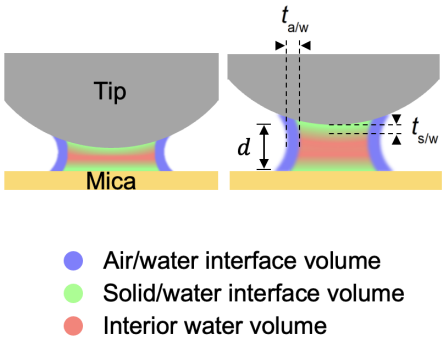

Figure 4.18: Spatio-spectral distribution for the nano-meniscus. The blue, green, and red areas indicate the regions of air/water interface, solid/water interface, and interior, respectively.

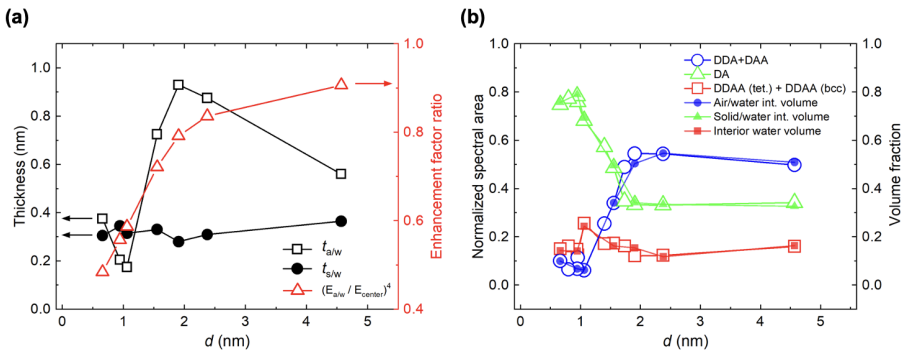

Figure 4.19: (a) $t_{\mathrm{a/w}}$, $t_{\mathrm{s/w}}$ and the ratio of enhancement factor between at the center and at the air/water interface are plotted versus d. (b) Comparison of the normalized Raman signal of fitted peaks (open symbols) and the calculated volume of nano-meniscus based on our model versus d (filled symbols). The calculated volume is corrected by considering the local electric-field intensity (red triangle in a) to compare with the Raman signal

nates under strong confinement below d_{bound}, where the mechanical relaxation time τ_{r} also increases as in figure 4.21. The increase of τ_{r} below d_{bound} shows that the newly assigned HB structure (bcc DDAA) is responsible for the enhanced mechanical solidity, which is consistent with the previous result that the ordered structure of strongly confined water near the substrate accompanies the enhanced τ_{r} [20]. Meanwhile, the increase of τ_{r} above d_{bound} can be attributed to the change of the HB structure at the air/water interface as the elongation of the nano-meniscus proceeds further [114]. We emphasize again that the ordered structure of strongly confined water that appears below d_{bound} is found as due to the dominant bcc DDAA structure of ice-VII. We also observe the transition from the more ordered structure of bcc DDAA to the tetrahedral DDAA as d increases, or as the confinement becomes lesser. This suggests that ice-VII that forms initially in an extremely small space can grow to the regular bulk ice-$\mathrm{I_h}$ at lower temperature. Notice that in our room-temperature experiment, the tetrahedral DDAA structure above d_{bound} consists of the liquid nano-meniscus of water. Moreover, our observation of the confinement-induced structural exchange between two DDAA structures can be considered as a general phenomenon for the confined interior water based on our confined water model.

4.9.2 Other peak behavior

The Raman shift and the spectral area of DAA and DDA signals are shown in figure 4.22.(a) and (b). The spectral area of both DAA and DDA signals show an abrupt decrease near d_{bound}. According to our meniscus model (figure

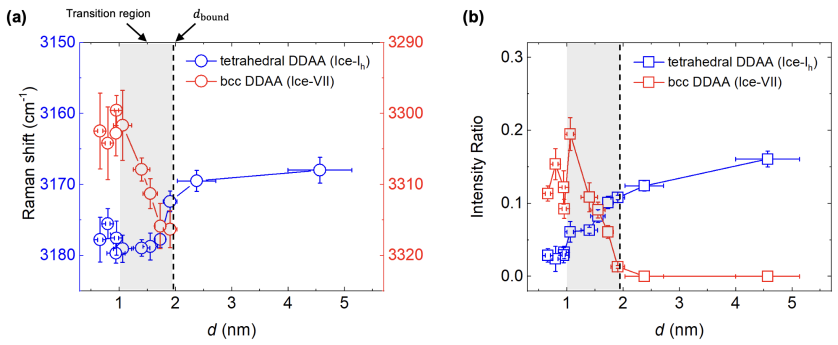

Figure 4.20: (a) The Raman shifts versus d show structural transition between tetrahedral DDAA (ice-Ih) and bcc DDAA (ice-VII). d_{bound} (2.05 ± 0.17 nm) is defined at the point where the relaxation time has its minimum value. The grey area represents the transition region where the two DDAA structures interchange. (b) The spectral area versus d for the tetrahedral DDAA and bcc DDAA, which are normalized since the volume of confined water remains constant during experiments.

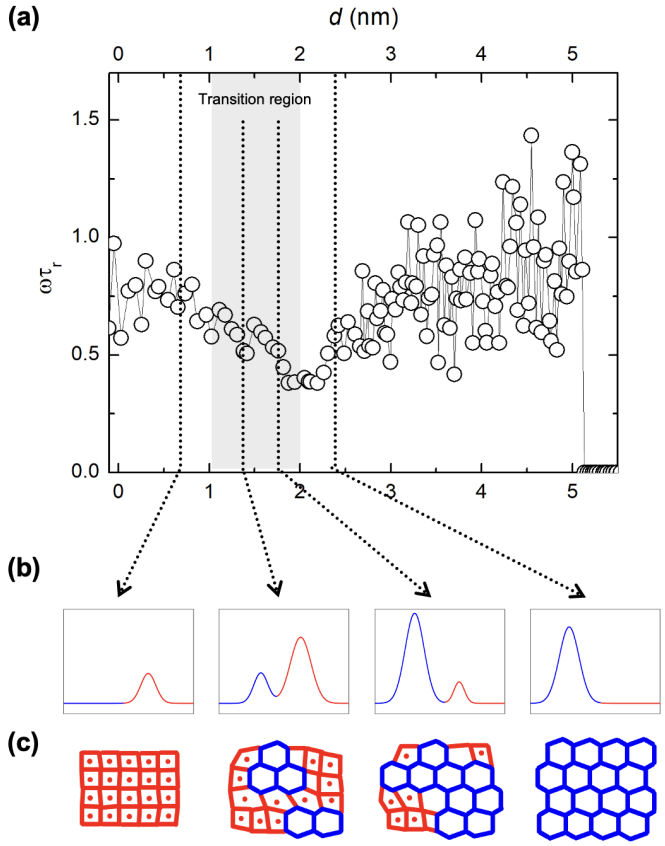

Figure 4.21: (a) Dimensionless mechanical relaxation time of confined water versus d observed during tip retraction. (b) The fitted curves for the two DDAA Raman signals (red; bcc DDAA, blue; tetrahedral DDAA) at specific values of d, and (c) the corresponding schematics of molecular structure.

4.18), we attribute the decrease of spectral area to the air/water interfacial volume that change with d. It is interesting to note that the intensity of DAA is comparable to other kinds of water, despite it being reported that a portion of the DAA water is very low in many systems [110, 144, 145] including air/water interface [26]. From the result of the hydrogen-bond measurement at the flat air/water interface obtained by the sum-frequency generation spectroscopy, it is confirmed that DAA water merely exists at the air/water interface. But it has been also reported that the DAA water can be abundant in a high curvature environment. [146]

The Raman frequency and the spectral area of the DA signal with respect to d are shown in figure 4.22.(c) and (d). As the confinement gets stronger, the DA water binds more strongly to the surface while the portion of DA signal in the meniscus increases. The increase in the portion of the DA signal can be seen as an increase in the solid/water interfacial volume that occurs as d decreases. In particular, the intensity of DAA and DDA water starts to decrease at d_{bound} while the intensity of DA water starts to increase at d_{bound}, which indicates that the DAA and DDA water at the air/water interface close to the tip and the mica change to the DA water at the solid/water interface through the hydrogen-bond rearrangement. It is consistent with this interpretation that the increasing amount of DA water and the decreasing amount of DAA and DDA water are almost the same.

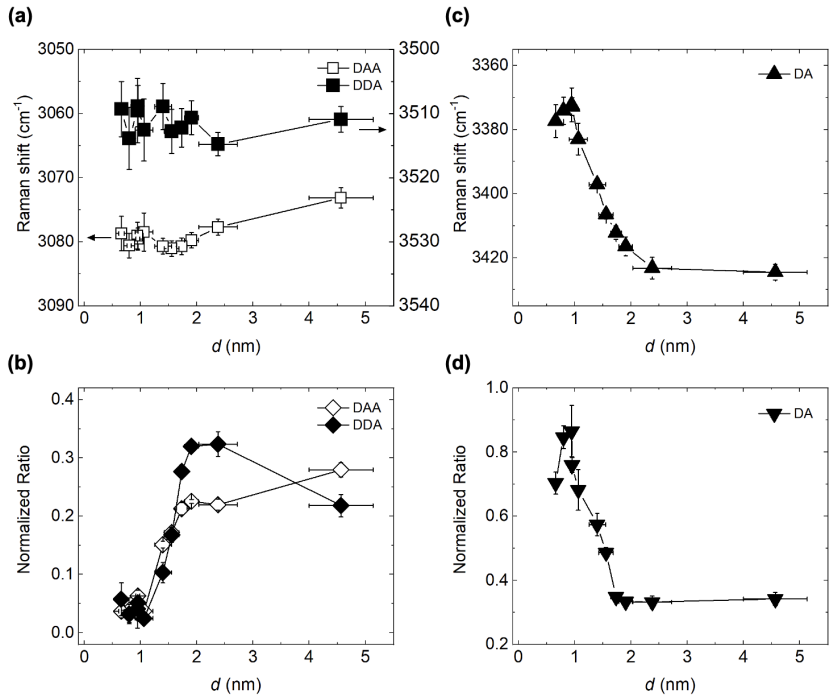

Figure 4.22: Plots of the spectral peak shift versus d of (a) DAA and DDA, and (c) DA. The normalized spectral area versus d of (b) DAA and DDA, and (d) DA are plotted.

4.10 Origin of the ice-VII

We now address the confinement-induced shift of the phase-transition boundary of ice-VII to the lower pressure region (red dots and red-dashed segment in figure 4.23). Such a shift is associated with the fact that nano-confined geometry substantially reduces the entropy of the molecules within, resulting in the limited degrees of freedom and structure of the HB network [147]. The recent *ab initio* MD simulation [22] reported similar results consistent to ours, where the liquid-solid phase boundary for monolayer water is shifted relative to that of bulk water due to confinement (black-dotted line in figure 4.23). To quantitatively characterize the effect of confinement (or the d-dependency) in terms of pressure, we estimate the normal-direction pressures exerted on the confined water and compare with those of the stable bulk ice-VII (see figure 4.24 and figure 4.17). The normal pressure is calculated from the measured shear-direction stiffness (figure 4.25) using the normal- and shear-hydration force relations through the Poisson ratio [148]. Notice that the confined water is supposed not to squeeze out due to its stiffness and thus starts being pressurized below the capillary-condensation point ($\sim$ 2.7 nm). As shown in figure 4.24, the Laplace pressure dominates in the weak confinement regime, while the hydration pressure dominates in the strong confinement regime. Comparing the Raman shifts of bcc DDAA with those of bulk ice-VII (figure 4.17), we immediately find that the minimum pressure required to form the bulk ice-VII is 2.02 GPa while the normal pressure exerted on the confined water is calculated as only about 0.19 GPa at the weakest confinement condition for bcc DDAA (i.e.,

$d \approx d_{\text{bound}}$). Thus, the threshold pressure for the formation of bcc DDAA in confined water is about 10 times lower than that of the bulk ice-VII due to the confinement effect. Such a promoted formation of bcc DDAA at much lower pressure facilitates the confinement-induced ice formation at room temperature by lowering the phase boundary, in comparison with the bulk-phase boundary (red-solid segment in figure 4.23). Notice that the electrofreezing effect is not responsible such a phase-boundary change since the electric field induced by static charge is not strong enough to cause crystallization (see Supplementary S8).

Electrofreezing effect

Solidification of water by the electric field is known as the electrofreezing phenomenon. The required electric field for electrofreezing of bulk water at room temperature is about 1 V/nm. Freshly cleaved mica has a very high surface potential of - 10 V or less due to the surface-charge imbalance. However, when cleaved mica is exposed to air, the surface charge is neutralized within a few hours [149] and the stabilized surface potential increases to - 50 $\sim$ -20 mV. In our experiment, the surface charge is neutralized by stabilizing for several hours before performing measurements. Therefore, the surface charge of mica is not considered as the cause of solidification because it is 40 $\sim$ 100 times lower for electrofreezing to occur.

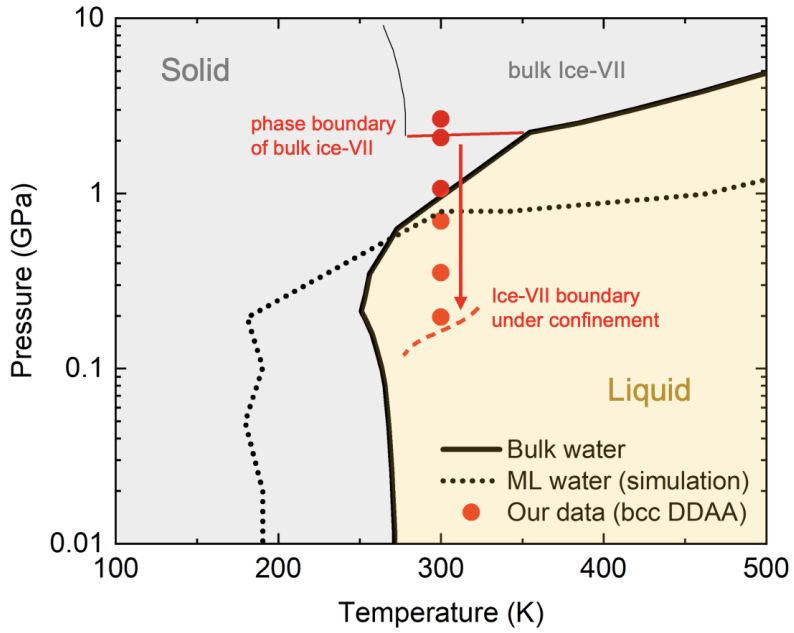

Figure 4.23: The thick black-solid line is the liquid-solid phase boundary of bulk water. The black-dotted line shows the simulated liquid-solid phase boundary for confined monolayer water [22]. The red-dashed segment represents the local phase boundary of ice-VII expected from our data (red dots) under weak confinement at 0.19 GPa pressure, which is shifted down in pressure from the bulk-Ice VII phase boundary (red-solid segment).

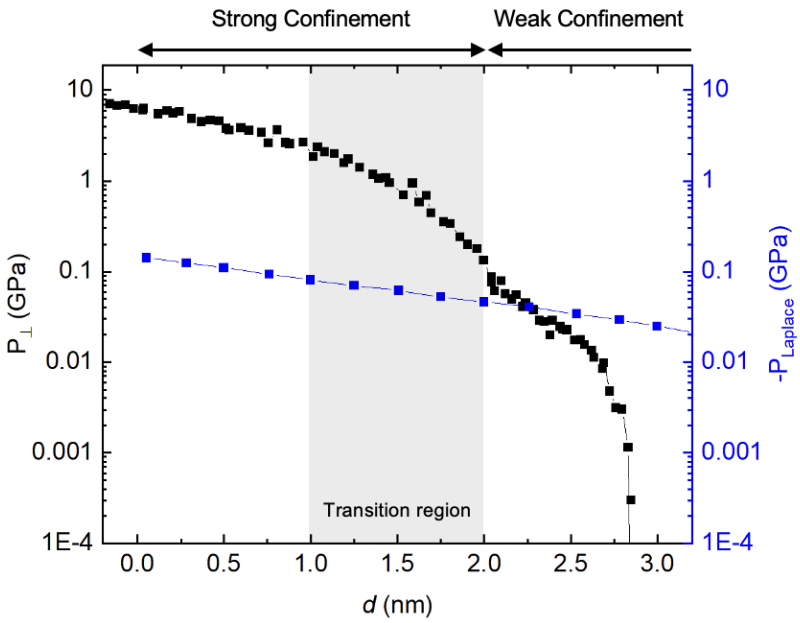

Figure 4.24: The calculated normal pressure (black) obtained from measured shear stiffness of confined water (figure 4.25) and the calculated negative Laplace pressure (blue) versus d. The grey region represents the transition region where the two DDAA signals are exchanged. The confinement below 2 nm distance is defined as the strong confinement where the bcc DDAA is observed.

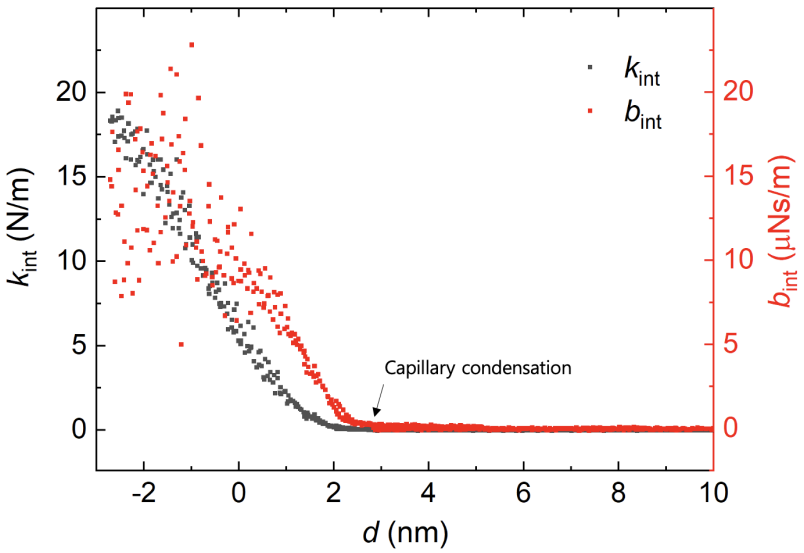

Figure 4.25: Elastic stiffness coefficient k_{int} (black) and damping coefficient b_{int} (red) due to the meniscus that are obtained from the amplitude and phase signal of QTF in the shear-mode AFM operation. The arrow indicates the position of capillary condensation of the meniscus where the strong elastic and damping coefficient emerge with respect to bulk water.

Chapter 5

Conclusion

We investigate confined water by measuring mechanical response time using AFM and Raman spectrum of OH-stretching band signal. From our experimental results, we confirm the correlation between the hydrogen bonding network and mechanical properties, so-called the structure-property relation. Also, we suggest the molecular origin of the peculiar properties of confined water from the unique hydrogen bond network under strong confinement observed in our experiment.

We establish Tip-enhanced Raman spectroscopy (TERS) by combining our homebulit quartz tuning fork (QTF) based atomic force microscopy (AFM) and homebulit confocal Raman spectroscopy to measure a very small ($\sim$ 10 yocto-liter) amount of nano-confined water which is notoriously difficult to observe. Tip fabrication methods are also developed, because tip is the most important part of TERS and reliable, reproducible, fresh tip is crucial to realize TERS.

Three tip fabrication methods are examined, etching, E-beam evaporation coating, and sputter coating. The average tip diameter is achieved at about $70 \sim 100$ nm regardless of fabrication methods at their optimized conditions, but E-beam evaporation tip shows the best performance among them. The performance of the tip is quantitatively estimated by measuring the enhancement factor (EF) of the tip. The average EF of the E-beam evaporation tip is 2.51×10^5.

A small amount of stable confined water is created by capillary condensation. When the hydrophilic tip and the hydrophilic substrate are closed enough (< 2 nm), a water cluster is formed as a meniscus shape between two surfaces. The tip is attached to QTF which has a high stiffness ($k \sim 10^4$ N/m) and a high quality factor of $\sim 10^4$. Thanks to the high stiffness of QTF, a strong adhesion force of the nano-meniscus is overcome and jump-to-contact instability is also prevented. And because of the high quality factor of QTF, precise tip-substrate distance control is possible while nano-meniscus are formed between tip and sample which is necessary for our experiments because tip-substrate distance should stay constant via PID feedback during Raman measurement.

Before analyzing the main experimental results, the size of the nano-meniscus is compared to the size of the optical 'hotspot', which is the volume of the enhanced field due to plasmonic resonance. It is important because the size of the nano-meniscus should be the same or smaller than the size of the 'hotspot' to reveal full hydrogen bond network of confined water including air/water interface. We calculate the 'hotspot' size between tip and substrate using finite difference time domain (FDTD) simulation. Then, the profile of nano-meniscus is calculated by numerically solving Young-Laplace equation. By comparison these

two volumes, one can find maximum volume of the meniscus $V_M \geq V \sim r_{\mathrm{rup}}^3$, where r_{rup} is the rupture distance of nano-meniscus. To match meniscus volume to 'hotspot' volume, the rupture distance of the meniscus is manipulated by controlling relative humidity in air-tight chamber.

Measured OH-stretching band signal is assigned in two ways, the spectral assignment and the spatial assignment. The OH-stretching band signal in weak confinement regime is fitted with four Gaussian curves, while signal in strong confinement regime is fitted with five Gaussian curves. And, four of them except one only appear in strong confinement regime are assigned with respect to the OH-stretching band signal of bulk water. To assign remain peak, we compare our data to all known ice phase DDAA peaks. As a result, the remain peak is assigned as a bcc DDAA, a unit structure of ice-VII. So, there are two DDAAs in confined water, tetrahedral DDAA and bcc DDAA. In the weak confinement condition, the tetrahedral DDAA dominates overall hydrogen bond network and its effective temperature is about 269K even we conduct our experiment at room temperature. In the strong confinement condition, the bcc DDAA dominates overall hydrogen bond network. We also observe a transition between two DDAAs depends on the degrees of confinement. The existence of the ice-VII in strong confinement may implies that the molecular origin of peculiar properties of confined water closely related to the unique structure of bcc DAAA.

Not like bulk water, each kind of hydrogen bonded water (DA, DDA, DAA, DDAA) is non-uniformly distributed in confined space. So, We introduce menisscus model for the spatial assignment. With the consideration of the electric field correction to the calculated volume of the meniscus, our experimental data is fit-

ted to the meniscus model. As a result, DA water is assigned to the solid/water interfaical water, DDA water and DAA water is assigned to the air/water interfacial water, and DDAA water is assigned to the interior water.

We attribute the origin of ice-VII to the confinement effect. To figure out effect of the direct pressure from tip, normal pressure exerted to the confined water is calculated. As expected, the Laplace pressure only dominates weak confinement regime. At the weakest confinement condition with ice-VII, $\sim$ 2 nm, calculated normal pressure is only 0.19 GPa. However, the minimum stable pressure condition of bulk ice-VII is 1.83 GPa. This pressure difference means that pressure threshold of the liquid-solid phase transition for the nano-confined ice-VII is much lowered due to the confinement. The consistent results is also reported in the very recent quantum molecular dynamics simulation study.

In summary, We have quantified the TERS study to address the HB-structure change of confined water using a single water nano-meniscus at room temperature. We demonstrate the confinement-induced formation of the bcc DDAA, the unit structure of ice VII, occurs at strong confinement ($d < d_{\mathrm{bound}} \approx 2$ nm) while the tetrahedral DDAA, the unit structure of ice-I_h, dominates at weak confinement. Moreover, we observe the so-far unexplored confinement-dependent structural transition between two DDAA structures within the transition region of 1 nm width. This suggests ice may nucleate as the bcc-DDAA structure (i.e., ice-VII) that is preferentially formed under strong confinement where the threshold pressure is lower, and then the ice-VII nucleus grows to the typical bulk ice-I_h or remains as the bulk liquid water depending on the ambient temperature. Furthermore, by comparing experimental data and our meniscus

model, we show the spatio-spectral correlation of the confined water that is consistent with previous studies. Our quantitative findings may provide novel insights into the role of confinement in the structure-property relation of the nano-bio materials and help address the origin of the anomalous behaviours of low-dimensional water via a better understanding of the confinement-dependent change of the complex HB network.

Appendix A

Probe aspect ratio dependent approach curve

Approach curves are measured for cantilevers with various aspect ratios (or cone angles) as well as at different relative humidity. In figure A.1, The three cantilever types we examine are shown. (a) is a common type of cantilever, and its aspect ratio is $2 \sim 3$ (cone angle $= 37 \sim 53°$). (b) is a top visible type cantilever, and its aspect ratio is $5 \sim 6$ (cone angle $= 18 \sim 23°$). (c) is a needle type high aspect ratio cantilever, its aspect ratio is higher than 10 (cone angle $< 11.5°$).

The approach curves for small and large aspect ratio are shown in figure A.2 and figure A.3, respectively. See Section 4.5 for the result of the medium aspect ratio cantilever. Relatively large amplitude drop at the capillary condensation point and relatively large hysteresis with respect to the medium aspect ratio probe are observed in the small aspect ratio probe even though their radius of

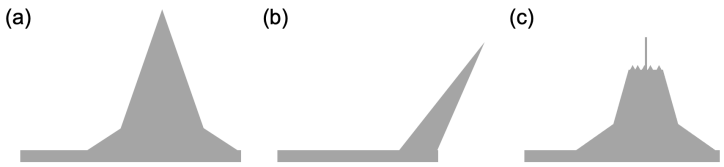

Figure A.1: The schematics of the side view of the three types of cantilever probes with different aspect ratio, (a) the aspect ratio of $2 \sim 3$ (PPP-NCHR, Nanosensors), (b) the aspect ratio of $5 \sim 6$ (ATEC-CONT, Nanosensors), (c) the aspect ratio higher than 10 (AR-NCHR, Nanosensors).

curvature at the probe apex is the same. This is because the nano-meniscus grows along the surface of the probe for the small aspect ratio probe.

For the large aspect ratio probe, no such hysteresis is observed after a capillary condensation point because of the small cone angle of $< 11.5°$. But, notice that saturated amplitudes are only 0.97 at RH 2.5% and 0.93 at RH 10%, unlike any other cantilever. This is because of the thin needle (figure A.1.(c)) The needle is too thin and soft to endure the strong interaction between tip and substrate.

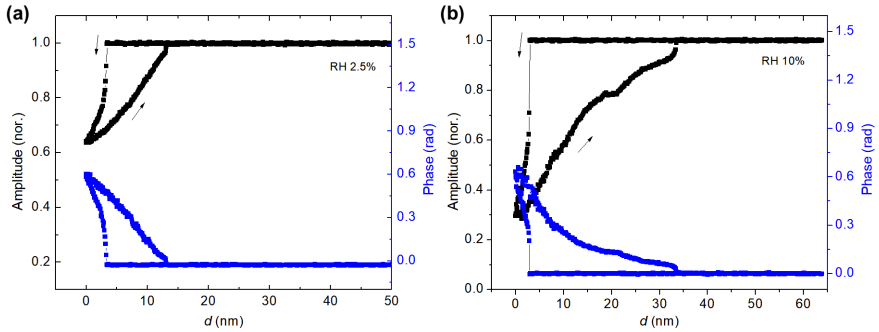

Figure A.2: Approach curves with small aspect ratio cantilever (figure A.1.(a)) (a) at RH 2.5 % and (b) at RH 10 %.

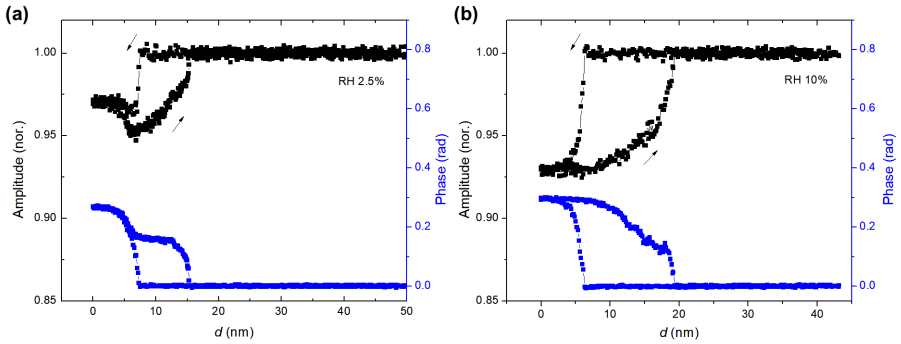

Figure A.3: Approach curves with large aspect ratio cantilever (figure A.1.(c) (a) at RH 2.5 % and (b) at RH 10 %.

Appendix B

Tip shape vs etching voltage

We fabricated etching tips under various voltage and etchant conditions. Basically, we use an etchant as a 1:4 ratio mixture solution of perchloric acid and ethanol. The etching curves are shown in figure B.1 in different etchants with different mixture ratio of 1:4, 1:10, and 1:20.

Each etch process proceeds with a given initial dc voltage. The etching voltage is the voltage across the resistor R1 in Fig. 3.13, which has the same tendency as the resistance of the etched part (R1). And the tendency of resistance to increase can be found when the etching process is almost finished due to the decreasing of the neck radius at the contact point of the etched wire and the etchant. In addition, the overetching is prevented by the appropriate cut-off voltage in each etching process.

The shape of the etched wire can be categorized into three types. The pencil-like shape, as shown in figure B.2.(a), usually fabricated from low initial volt-

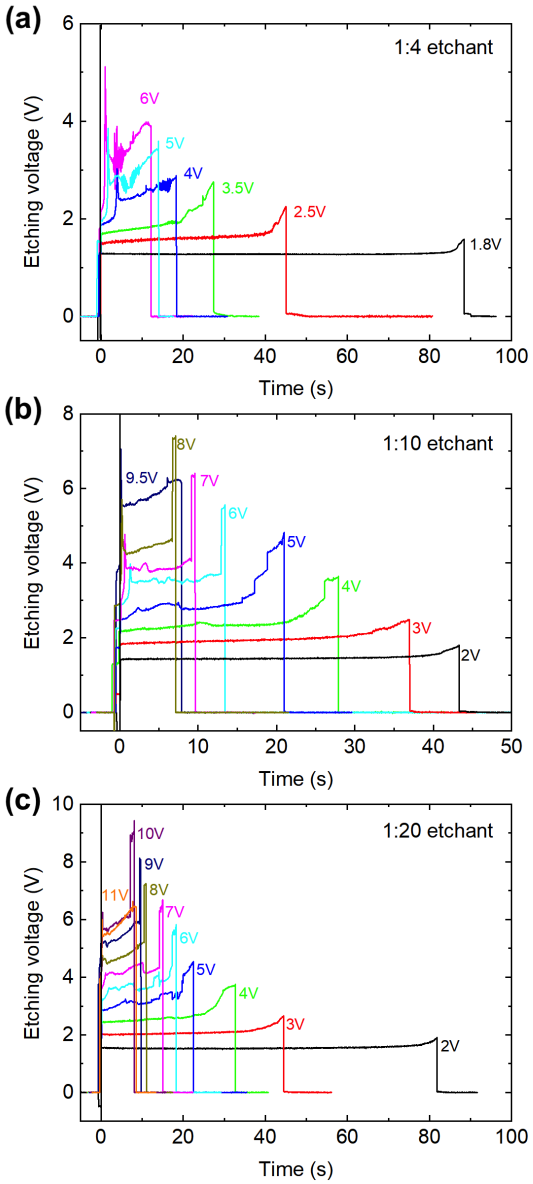

Figure B.1: Etching curves at different etchants and at various initial etching voltage. (a) 1:4 etchant, (b) 1:10 etchant, (c) 1:20 etchant.

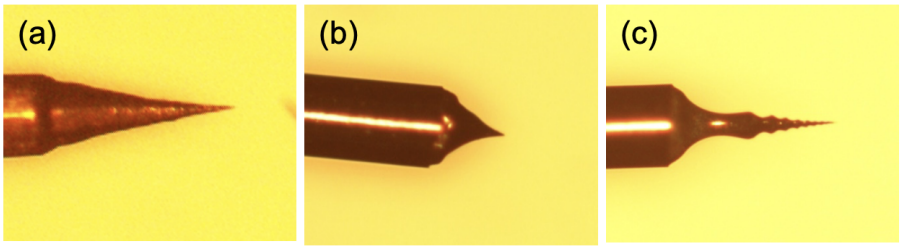

Figure B.2: Etching tip shapes. Wire diameter is 100 μm. (a) low etching voltage shape. (b) medium voltage shape. (c) high voltage shape.

ages. These types of results are obtained at initial voltages of $0 \sim 3$ V for 1:4 etchant, $0 \sim 5$ V for 1:10 etchant, and $0 \sim 6.5$ V for 1:20 etchant. However, the residue is not washed away in many cases and the diameter of the fabricated tip is quite large of ~ 1 μm. The fabricated tips with the shape of figure B.2.(b) are seen at moderate initial voltages. This shape didn't appear in the 1:4 etchant, but it appeared at the initial voltage of $6 \sim 8$ V in the 1:10 etchant and $7 \sim 10$ V in the 1:20 etchant. The yield was better than the result of the pencil-like shape tip, but it is still less than 50 %. The fabricated tip with a shape like the Buddhist temple tower, as shown in figure B.2.(c), is only fabricated under relatively high initial voltages. These types of results are obtained at initial voltages of > 4 V for 1:4 etchant, > 9 V for 1:10 etchant, and > 11 V for 1:20 etchant. It gives the highest yield of $80 \sim 90$ %, and the diameter is less than 100 nm. Tower-like shapes appear in all etchants regardless of the mixture ratio, but the best yield is acquired in 1:4 etchant (~ 90 %).

Appendix C

Tip quality table

The SNR table of the nano-water Raman signal calculated based on the peak near 3400 cm^{-1} is shown in table C.1. To measure the enhancement factor or the TERS contrast, both a tip-out signal (micro Raman signal) and a tip-in signal (TER signal) are needed. However, in our experiment, the tip-out signal of confined water cannot be obtained because the Raman cross-section of a water molecule is very small and the tiny number of water molecules (164 $\sim$ 5000) consists of nano-meniscus [114]. Therefore, we marked 'N' in the table in which condition without the Raman signal of confined water, marked 'Y' in which condition with the Raman signal of confined water and wrote down the approximate SNR in parentheses. The sputter coating tip is not used in our experiment because it contains many impurities. In spite of the high aspect ratio of the AR cantilever, the SNR of the Raman signal of confined water is lower than the expected value. We thought the high aspect ratio of the probe

Thickness (nm)	Coating type	Aspect ratio		
		Small (PPP)	Medium (ATEC)	Large (AR)
20	Sputter	Y ($\sim$ 2)	Y ($\sim$ 2)	N
30	Sputter	Y ($\sim$ 2)	Y ($\sim$ 10)	N
50	Sputter	N	N	N
50	E-beam	N	Y ($<$ 2)	N
75	E-beam	N	Y ($\sim$ 3)	Y ($\sim$ 4)
100	E-beam	N	Y ($\sim$ 15)	Y ($\sim$ 3)
125	E-beam	N	Y ($<$ 2)	N

Table C.1: Table of the average SNR of the Raman signal of confined water in OH-stretching band. SNR is measured with the highest peak. The meaningful data is only observed in squares marked with Y. The number in parenthesis is the approximate SNR.

prevent metal coating at the very end of the probe.

Appendix D

Airtight metal chamber specification

The result of the temperature and relative humidity stability test of the airtight metal chamber is described in this chapter. Figure D.1 shows the result of changing the RH. After lowering the RH to 0 % by dry nitrogen gas purging, keep purging for 1 hour to give sufficient time to diffuse impurities that may be attached to the surface of the chamber. An hour later, the humidity is raised to RH 18 %, and all valves are closed. The humidity inside the chamber is increased by about 0.12 % after 3 hours. Notice that the red line is the linear fitting result of the data after 2 hours. The RH changing rate per hour is 0.0397 %/h, and the outside humidity is 45 %. A digital sensor (SHT85, Sensirion) is used for temperature and humidity measurement, and humidity is controlled through a gas mixture of dry nitrogen gas and wet nitrogen gas.

The performance of the chamber was tested in another way. After the hu-

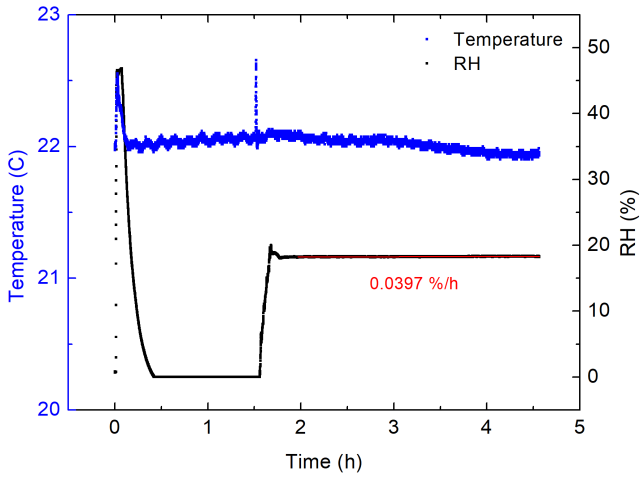

Figure D.1: Temperature and RH in the chamber with time. The red line is the linear fitting of RH after 2 hours.

midity is lowered to 0 % through dry nitrogen gas purging, the purging is continued for about an hour. After that, all valves are closed, and the time is recorded when the humidity displayed on the sensor was out of 0 %. (figure D.2) First, the time was 10.7 h without any treatment for the chamber. We thought the biggest leakage is caused by the rubber ring on the door of the chamber, so a very thin layer of vacuum grease is spread on the rubber ring. After vacuum grease treatment, the time at which the RH becomes greater than RH 0% is 29.5 h.

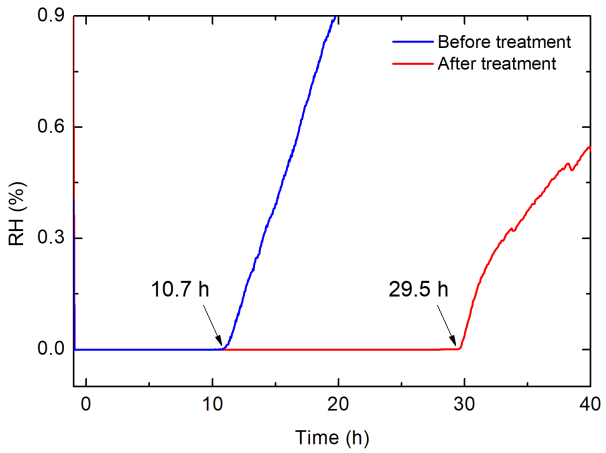

Figure D.2: The zero-RH maintaining time before (blue) and after (red) vacuum grease treatment.

Bibliography

[1] D. Wang, Y. Tian and L. Jiang, *Abnormal Properties of Low-Dimensional Confined Water*, *Small* **17** (2021) 1.

[2] M. Urbakh, J. Klafter, D. Gourdon and J. Israelachvili, *The nonlinear nature of friction*, *Nature* **430** (2004) 525.

[3] S. Granick, *Motions and relaxations of confined liquids*, *Science* **253** (1991) 1374.

[4] E. Secchi, S. Marbach, A. Niguès, D. Stein, A. Siria and L. Bocquet, *Massive radius-dependent flow slippage in carbon nanotubes*, *Nature* **537** (2016) 210.

[5] M. Ma, F. Grey, L. Shen, M. Urbakh, S. Wu and J. Z. Liu, *Water transport inside carbon nanotubes mediated by phonon-induced oscillating friction*, *Nature Nanotechnology* **10** (2015) 692.

[6] S. Dalla Bernardina, E. Paineau, J. B. Brubach, P. Judeinstein, S. Rouziere, P. Launois et al., *Water in Carbon Nanotubes: The Peculiar*

Hydrogen Bond Network Revealed by Infrared Spectroscopy, *Journal of the American Chemical Society* **138** (2016) 10437.

[7] L. Fumagalli, A. Esfandiar, R. Fabregas, S. Hu, P. Ares, A. Janardanan et al., *Anomalously low dielectric constant of confined water*, *Science* **360** (2018) 1339.

[8] C. Zhang, F. Gygi and G. Galli, *Strongly anisotropic dielectric relaxation of water at the nanoscale*, *Journal of Physical Chemistry Letters* **4** (2013) 2477.

[9] A. Schlaich, E. W. Knapp and R. R. Netz, *Water Dielectric Effects in Planar Confinement*, *Physical Review Letters* **117** (2016) 1.

[10] Y. Leng and P. T. Cummings, *Fluidity of hydration layers nanoconfined between mica surfaces*, *Physical Review Letters* **94** (2005) 19.

[11] D. Ortiz-Young, H.-C. Chiu, S. Kim, K. Voitchovsky and E. Riedo, *The interplay between apparent viscosity and wettability in nanoconfined water*, *Nature Communications* **4** (2013) .

[12] M. Neek-Amal, F. M. Peeters, I. V. Grigorieva and A. K. Geim, *Commensurability Effects in Viscosity of Nanoconfined Water*, *ACS Nano* **10** (2016) 3685.

[13] S. H. Chong and S. Ham, *Anomalous Dynamics of Water Confined in Protein-Protein and Protein-DNA Interfaces*, *Journal of Physical Chemistry Letters* **7** (2016) 3967.

[14] H. Wei, E. P. Vejerano, W. Leng, Q. Huang, M. R. Willner, L. C. Marr et al., *Aerosol microdroplets exhibit a stable pH gradient*, *Proceedings of the National Academy of Sciences* (2018) 1.

[15] D. Muñoz-Santiburcio and D. Marx, *Nanoconfinement in Slit Pores Enhances Water Self-Dissociation*, *Physical Review Letters* **119** (2017) 1.

[16] C. E. Talley, L. Jusinski, C. W. Hollars, S. M. Lane and T. Huser, *Intracellular pH sensors based on surface-enhanced raman scattering*, *Analytical Chemistry* **76** (2005) 7064.

[17] J. Kneipp, H. Kneipp, B. Wittig and K. Kneipp, *Following the dynamics of pH in endosomes of live cells with SERS nanosensors*, *Journal of Physical Chemistry C* **114** (2010) 7421.

[18] M. R. Uhlig and R. Garcia, *In Situ Atomic-Scale Imaging of Interfacial Water under 3D Nanoscale Confinement*, *Nano Letters* **21** (2021) 5593.

[19] T. D. Li, H. C. Chiu, D. Ortiz-Young and E. Riedo, *Nanorheology by atomic force microscopy*, *Review of Scientific Instruments* **85** (2014) 123707.

[20] S. H. Khan, G. Matei, S. Patil and P. M. Hoffmann, *Dynamic solidification in nanoconfined water films*, *Physical Review Letters* **105** (2010) 106101.

[21] J. Israelachvili and R. Pashley, *Molecular layering of water at surfaces and origin of repulsive hydration forces*, *Nature* **306** (1983) 2.

[22] V. Kapil, C. Schran, A. Zen, J. Chen, C. J. Pickard and A. Michaelides, *The first-principles phase diagram of monolayer nanoconfined water*, *Nature* **609** (2022) 512.

[23] J. Jiang, Y. Gao, W. Zhu, Y. Liu, C. Zhu, J. S. Francisco et al., *First-Principles Molecular Dynamics Simulations of the Spontaneous Freezing Transition of 2D Water in a Nanoslit*, *Journal of the American Chemical Society* **143** (2021) 8177.

[24] Y. H. Wang, S. Zheng, W. M. Yang, R. Y. Zhou, Q. F. He, P. Radjenovic et al., *In situ Raman spectroscopy reveals the structure and dissociation of interfacial water*, *Nature* **600** (2021) 81.

[25] D. Shin, J. Hwang and W. Jhe, *Ice-VII-like molecular structure of ambient water nanomeniscus*, *Nature Communications* **10** (2019) 286.

[26] G. R. Medders and F. Paesani, *Dissecting the Molecular Structure of the Air/Water Interface from Quantum Simulations of the Sum-Frequency Generation Spectrum*, *Journal of the American Chemical Society* **138** (2016) 3912.

[27] J. J. Velasco-Velez, C. H. Wu, T. A. Pascal, L. F. Wan, J. Guo, D. Prendergast et al., *The structure of interfacial water on gold electrodes studied by x-ray absorption spectroscopy*, *Science* **346** (2014) 831.

[28] A. Hakimian, M. Mohebinia, M. Nazari, A. Davoodabadi, S. Nazifi, Z. Huang et al., *Freezing of few nanometers water droplets*, *Nature Communications* **12** (2021) 1.

[29] N. Tallarida, J. Lee and V. A. Apkarian, *Tip-Enhanced Raman Spectromicroscopy on the Angstrom Scale: Bare and CO-Terminated Ag Tips*, *ACS Nano* **11** (2017) 11393.

[30] D. Roy, J. Wang and C. Williams, *Novel methodology for estimating the enhancement factor for tip-enhanced Raman spectroscopy*, *Journal of Applied Physics* **105** (2009) 013530.

[31] F. M. Orr, L. E. Scriven and A. P. Rivas, *Pendular rings between solids: Meniscus properties and capillary force*, *Journal of Fluid Mechanics* **67** (1975) 723.

[32] E. Riedo, F. Lévy and H. Brune, *Kinetics of Capillary Condensation in Nanoscopic Sliding Friction*, *Physical Review Letters* **88** (2002) 4.

[33] J. W. Van Honschoten, N. Brunets and N. R. Tas, *Capillarity at the nanoscale*, *Chemical Society Reviews* **39** (2010) 1096.

[34] E. Barsotti, S. P. Tan, S. Saraji, M. Piri and J. H. Chen, *A review on capillary condensation in nanoporous media: Implications for hydrocarbon recovery from tight reservoirs*, *Fuel* **184** (2016) 344.

[35] G. Binnig, C. F. Quate and C. Gerber, *Atomic force microscopy*, *Physical review letters* **56** (1986) .

[36] M. Krieg, G. Fläschner, D. Alsteens, B. M. Gaub, W. H. Roos, G. J. Wuite et al., *Atomic force microscopy-based mechanobiology*, *Nature Reviews Physics* **1** (2019) 41.

[37] D. Alsteens, H. E. Gaub, R. Newton, M. Pfreundschuh, C. Gerber and D. J. Müller, *Atomic force microscopy-based characterization and design of biointerfaces*, *Nature Reviews Materials* **2** (2017) .

[38] S. Chen, Y. Itoh, T. Masuda, S. Shimizu, J. Zhao, J. Ma et al., *Subnanoscale hydrophobic modulation of salt bridges in aqueous media*, *Science* **348** (2015) 555.

[39] M. Nonnenmacher, M. P. O'Boyle and H. K. Wickramasinghe, *Kelvin probe force microscopy*, *Applied Physics Letters* **58** (1991) 2921.

[40] W. Melitz, J. Shen, A. C. Kummel and S. Lee, *Kelvin probe force microscopy and its application*, *Surface Science Reports* **66** (2011) 1.

[41] J. R. Matey and J. Blanc, *Scanning capacitance microscopy*, *Journal of Applied Physics* **57** (1985) 1437.

[42] K. B. Holt, A. J. Bard, Y. Show and G. M. Swain, *Scanning electrochemical microscopy and conductive probe atomic force microscopy studies of hydrogen-terminated boron-doped diamond electrodes with different doping levels*, *Journal of Physical Chemistry B* **108** (2004) 15117.

[43] W. Frammelsberger, G. Benstetter, J. Kiely and R. Stamp, *C-AFM-based thickness determination of thin and ultra-thin SiO 2 films*

by use of different conductive-coated probe tips, *Applied Surface Science* **253** (2007) 3615.

[44] P. Girard, *Electrostatic force microscopy: Principles and some applications to semiconductors*, *Nanotechnology* **12** (2001) 485.

[45] U. Hartmann, *Magnetic force microscopy*, *Annual Review of Materials Science* **29** (1999) 53.

[46] O. Kazakova, R. Puttock, C. Barton, H. Corte-León, M. Jaafar, V. Neu et al., *Frontiers of magnetic force microscopy*, *Journal of Applied Physics* **125** (2019) .

[47] A. J. Weymouth, T. Hofmann and F. J. Giessibl, *Quantifying molecular stiffness and interaction with lateral force microscopy*, *Science* **343** (2014) 1120.

[48] F. J. Giessibl, *Advances in atomic force microscopy*, *Reviews of Modern Physics* **75** (2003) 949.

[49] K. Karrai, *Lecture notes on shear and friction force detection with quartz tuning forks*, *Proc.'Ecole Thematique de CNRS'on near-field optics (La Londe les Maures, France)* (2000) .

[50] M. Lee, J. Jahng, K. Kim and W. Jhe, *Quantitative atomic force measurement with a quartz tuning fork*, *Applied Physics Letters* **91** (2007) 2.

[51] M. Lee and W. Jhe, *General theory of amplitude-modulation atomic force microscopy*, *Physical Review Letters* **97** (2006) 036104.

[52] F. J. Giessibl, *The qPlus sensor, a powerful core for the atomic force microscope*, *Review of Scientific Instruments* **90** (2019) 011101.

[53] F. J. Giessibl, *High-speed force sensor for force microscopy and profilometry utilizing a quartz tuning fork High-speed force sensor for force microscopy and profilometry utilizing a quartz tuning fork*, *Applied Physics Letters* **73** (1998) 3956.

[54] H. Hertz, *Über die Berührung fester elastischer Körper*, *J Reine Angew. Math.* (1882) 156.

[55] B. V. Derjaguin, V. M. Muller and Y. P. Toporov, *Effect of contact deformation on the adhesion of particles*, *Journal of Colloid and Interface Science* **53** (1975) 314.

[56] K. L. Johnson, K. Kendall and A. D. Roberts, *Surface energy and the contact of elastic solids*, *Proceedings of the Royal Society of London. A. Mathematical and Physical Sciences* **324** (1971) 301.

[57] Y. Martin, C. C. Williams and H. K. Wickramasinghe, *Atomic force microscope-force mapping and profiling on a sub 100-Å scale*, *Journal of Applied Physics* **61** (1987) 4723.

[58] Q. Zhong, D. Inniss, K. Kjoller and V. B. Elings, *Fractured polymer/silica fiber surface studied by tapping mode atomic force microscopy*, *Surface Science* **290** (1993) .

[59] T. R. Albrecht, P. Grütter, D. Horne and D. Rugar, *Frequency modulation detection using high-Q cantilevers for enhanced force microscope sensitivity*, *Journal of Applied Physics* **69** (1991) 668.

[60] R. García and R. Perez, *Dynamic atomic force microscopy methods*, *Surface Science Reports* **47** (2002) 197.

[61] G. R. Heath, E. Kots, J. L. Robertson, S. Lansky, G. Khelashvili, H. Weinstein et al., *Localization atomic force microscopy*, *Nature* **594** (2021) 385.

[62] K. Umeda, C. Okamoto, M. Shimizu, S. Watanabe, T. Ando and N. Kodera, *Architecture of zero-latency ultrafast amplitude detector for high-speed atomic force microscopy*, *Applied Physics Letters* **119** (2021) .

[63] C. V. Raman and K. S. Krishnan, *A New Type of Secondary Radiation*, *Nature* (1928) 501.

[64] L. D. Landau and E. M. Lifshitz, *The classical theory of fields*. Elsevier, 4th ed., 1980.

[65] J. Rychlewski, *Frequency dependent polarizabilities for the ground state of H2, HD, and D2*, *Journal of Chemical Physics* **78** (1983) .

[66] M. Fleischmann, P. J. Hendra and A. J. Mcquillan, *Raman spectra of pyridine adsorbed at a silver electrode*, *chemical physics letters* **26** (1974) 163.

[67] J. Langer, D. J. de Aberasturi, J. Aizpurua, R. A. Alvarez-Puebla, B. Auguié, J. J. Baumberg et al., *Present and future of surface-enhanced Raman scattering*, *ACS Nano* **14** (2020) 28.

[68] S. Y. Ding, J. Yi, J. F. Li, B. Ren, D. Y. Wu, R. Panneerselvam et al., *Nanostructure-based plasmon-enhanced Raman spectroscopy for surface analysis of materials*, *Nature Reviews Materials* **1** (2016) 1.

[69] K. Hering, D. Cialla, K. Ackermann, T. Dörfer, R. Möller, H. Schneidewind et al., *SERS: A versatile tool in chemical and biochemical diagnostics*, *Analytical and Bioanalytical Chemistry* **390** (2008) 113.

[70] E. C. Le Ru, E. Blackie, M. Meyer and P. G. Etchegoint, *Surface enhanced raman scattering enhancement factors: A comprehensive study*, *Journal of Physical Chemistry C* **111** (2007) 13794.

[71] A. B. Zrimsek, N. Chiang, M. Mattei, S. Zaleski, M. O. McAnally, C. T. Chapman et al., *Single-Molecule Chemistry with Surface- and Tip-Enhanced Raman Spectroscopy*, *Chemical Reviews* (2016) A.

[72] J. R. Lombardi and R. L. Birke, *A unified approach to surface-enhanced raman spectroscopy*, *Journal of Physical Chemistry C* **112** (2008) 5605.

[73] A. Otto, *The 'chemical' (electronic) contribution to surface-enhanced Raman scattering*, *Journal of Raman Spectroscopy* **36** (2005) 497.

[74] Y. Kim and E. Kazuma, *Mechanistic studies of plasmon chemistry on metal catalysts*, *Angewandte Chemie International Edition* (2018) 10.1002/ange.201811234.

[75] S. Kawata, T. Ichimura, A. Taguchi and Y. Kumamoto, *Nano-Raman scattering microscopy: Resolution and enhancement*, *Chemical Reviews* **117** (2017) 4983.

[76] M. M. Sartin, H. S. Su, X. Wang and B. Ren, *Tip-enhanced Raman spectroscopy for nanoscale probing of dynamic chemical systems*, *Journal of Chemical Physics* **153** (2020) 170901.

[77] F. Shao and R. Zenobi, *Tip-enhanced Raman spectroscopy: principles, practice, and applications to nanospectroscopic imaging of 2D materials*, *Analytical and Bioanalytical Chemistry* **411** (2019) 37.

[78] J. Wessel, *Surface-enhanced optical microscopy*, *Journal of the Optical Society of America B* **2** (1985) 1538.

[79] R. M. Stöckle, Y. D. Suh, V. Deckert and R. Zenobi, *Nanoscale chemical analysis by tip-enhanced Raman spectroscopy*, *Chemical Physics Letters* **318** (2000) 131.

[80] N. Hayazawa, Y. Inouye, Z. Sekkat and S. Kawata, *Metallized tip amplification of near-field Raman scattering*, *Optics Communications* **183** (2000) 333.

[81] M. S. Anderson, *Locally enhanced Raman spectroscopy with an atomic force microscope*, *Applied Physics Letters* **76** (2000) 3130.

[82] B. Pettinger, G. Picardi, R. Schuster and G. Ertl, *Surface Enhanced Raman Spectroscopy : Towards Single Molecule Spectroscopy*, *Electrochemistry* **68** (2000) 942.

[83] J. Lee, K. T. Crampton, N. Tallarida and V. A. Apkarian, *Visualizing vibrational normal modes of a single molecule with atomically confined light*, *Nature* **568** (2019) 78.

[84] N. Hayazawa, Y. Inouye and S. Kawata, *Evanescent field excitation and measurement of dye fluorescence in a metallic probe near-field scanning optical microscope*, *Journal of Microscopy* **194** (1999) 472.

[85] F. Huber and F. J. Giessibl, *Low noise current preamplifier for qPlus sensor deflection signal detection in atomic force microscopy at room and low temperatures*, *Review of Scientific Instruments* **88** (2017) .

[86] B. Su, X. Yang, H. Cui and D. R. Jones, *How to maximize the bandwidth without increasing the noise in op-amp-based transimpedance amplifiers using positive feedback*, *Review of Scientific Instruments* **93** (2022) .

[87] T. Starecki and P. Z. Wieczorek, *A high sensitivity preamplifier for quartz tuning forks in qepas (Quartz enhanced photoacoustic spectroscopy) applications*, *Sensors (Switzerland)* **17** (2017) .

[88] N. C. Pisenti, A. Restelli, B. J. Reschovsky, D. S. Barker and G. K. Campbell, *An ultra-low noise, high-voltage piezo-driver*, *Review of Scientific Instruments* **87** (2016) 1.

[89] E. Kleinbaum and G. A. Csáthy, *Note: A transimpedance amplifier for remotely located quartz tuning forks*, *Review of Scientific Instruments* **83** (2012) 1.

[90] I. Morawski, J. Blicharski and B. Voigtlnder, *Voltage preamplifier for extensional quartz sensors used in scanning force microscopy*, *Review of Scientific Instruments* **82** (2011) .

[91] B. Kim, J. Jahng, R. M. Khan, S. Park and E. O. Potma, *Eigenmodes of a quartz tuning fork and their application to photoinduced force microscopy*, *Physical Review B* **95** (2017) 1.

[92] O. E. Dagdeviren, Y. Miyahara, A. Mascaro and P. Grütter, *Calibration of the oscillation amplitude of electrically excited scanning probe microscopy sensors*, *Review of Scientific Instruments* **90** (2019) 013703.

[93] J. Kim, D. Won, B. Sung, S. An and W. Jhe, *Effective stiffness of qPlus sensor and quartz tuning fork*, *Ultramicroscopy* **141** (2014) 56.

[94] K. S. V. Dyke, *The piezo-electric resonator and its equivalent network*, *Proceedings of the Institute of Radio Engineers* **16** (1928) 742.

[95] A. M. Angulo, C. Noguez and G. C. Schatz, *Electromagnetic Field Enhancement for Wedge-Shaped Metal Nanostructures*, *The Journal of Physical Chemistry Letters* **2** (2011) 1978.

[96] T. X. Huang, S. C. Huang, M. H. Li, Z. C. Zeng, X. Wang and B. Ren, *Tip-enhanced Raman spectroscopy: tip-related issues*, *Analytical and bioanalytical chemistry* **407** (2015) 8177.

[97] A. Taguchi, N. Hayazawa, Y. Saito, H. Ishitobi, A. Tarun and S. Kawata, *Controlling the plasmon resonance wavelength in metal-coated probe using refractive index modification.*, *Optics express* **17** (2009) 6509.

[98] X. Cui, W. Zhang, B.-S. Yeo, R. Zenobi, C. Hafner and D. Erni, *Tuning the resonance frequency of Ag-coated dielectric tips*, *Optics Express* **15** (2007) 8309.

[99] Z. Yang, J. Aizpurua and H. Xu, *Electromagnetic field enhancement in TERS configurations*, *Journal of Raman Spectroscopy* **40** (2009) 1343.

[100] A. L. Demming, F. Festy and D. Richards, *Plasmon resonances on metal tips: Understanding tip-enhanced Raman scattering*, *Journal of Chemical Physics* **122** (2005) 184716.

[101] J. P. Ibe, P. P. Bey, S. L. Brandow, R. A. Brizzolara, N. A. Burnham, D. P. DiLella et al., *On the electrochemical etching of tips for scanning tunneling microscopy*, *Journal of Vacuum Science Technology A: Vacuum, Surfaces, and Films* **8** (1990) 3570.

[102] N. Kumar, Bert M. Weckhuysen, Andrew J. Wain and A. J. Pollard, *Nanoscale Chemical Imaging Using Tip-Enhanced Raman Spectroscopy*, *Nature Protocols* **14** (2019) 1169.

[103] V. J. Logeeswaran, N. P. Kobayashi, M. S. Islam, W. Wu, P. Chaturvedi, N. X. Fang et al., *Ultrasmooth silver thin films deposited with a germanium nucleation layer*, *Nano Letters* **9** (2009) 178.

[104] M. Todeschini, A. Bastos Da Silva Fanta, F. Jensen, J. B. Wagner and A. Han, *Influence of Ti and Cr Adhesion Layers on Ultrathin Au Films*, *ACS Applied Materials and Interfaces* **9** (2017) 37374.

[105] T. G. Habteyes, S. Dhuey, E. Wood, D. Gargas, S. Cabrini, P. J. Schuck et al., *Metallic adhesion layer induced plasmon damping and molecular linker as a nondamping alternative*, *ACS Nano* **6** (2012) 5702.

[106] W. M. Abbott, C. P. Murray, S. Ní Lochlainn, F. Bello, C. Zhong, C. Smith et al., *Comparison of Metal Adhesion Layers for Au Films in Thermoplasmonic Applications*, *ACS Applied Materials and Interfaces* **12** (2020) 13503.

[107] Y. Lee, D. Kim, J. Jeong, J. Kim, V. Shmid, O. Korotchenkov et al., *Enhanced terahertz conductivity in ultra-thin gold film deposited onto (3-mercaptopropyl) trimethoxysilane (MPTMS)-coated Si substrates*, *Scientific Reports* **9** (2019) 5.

[108] J. N. Israelachvili, *Measurement of the viscosity of liquids in very thin films*, *Journal of Colloid And Interface Science* **110** (1986) 263.

[109] J. Klein and E. Kumacheva, *Simple liquids confined to molecularly thin layers. I. Confinement-induced liquid-to-solid phase transitions*, *Journal of Chemical Physics* **108** (1998) 6996.

[110] D. M. Carey and G. M. Korenowski, *Measurement of the Raman spectrum of liquid water*, *J. Chem. Phys.* **108** (1998) 2669.

[111] C. Y. Li, J. B. Le, Y. H. Wang, S. Chen, Z. L. Yang, J. F. Li et al., *In situ probing electrified interfacial water structures at atomically flat surfaces*, *Nature Materials* **18** (2019) 697.

[112] K. V. Agrawal, S. Shimizu, L. W. Drahushuk, D. Kilcoyne and M. S. Strano, *Observation of extreme phase transition temperatures of water confined inside isolated carbon nanotube nanopores*, *Nature nanotechnology* **12** (2016) 267.

[113] B. Pettinger, B. Ren, G. Picardi, R. Schuster and G. Ertl, *Nanoscale probing of adsorbed species by tip-enhanced Raman spectroscopy*, *Physical Review Letters* **92** (2004) 8.

[114] J. Kim, D. Won, B. Sung and W. Jhe, *Observation of universal solidification in the elongated water nanomeniscus*, *Journal of Physical Chemistry Letters* **5** (2014) 737.

[115] S. H. Khan and P. M. Hoffmann, *Squeeze-out dynamics of nanoconfined water: A detailed nanomechanical study*, *Physical Review E - Statistical, Nonlinear, and Soft Matter Physics* **92** (2015) 1.

[116] J. P. Cleveland, B. Anczykowski, A. E. Schmid and V. B. Elings, *Energy dissipation in tapping-mode atomic force microscopy*, *Applied Physics Letters* **72** (1998) 2613.

[117] B. Kim, S. Kwon, M. Lee, Q. Kim, S. An and W. Jhe, *Probing nonlinear rheology layer-by-layer in interfacial hydration water*, *Proceedings of the*

National Academy of Sciences of the United States of America **112** (2015) 15619.

[118] S. Kim, D. Kim, J. Kim, S. An and W. Jhe, *Direct Evidence for Curvature-Dependent Surface Tension in Capillary Condensation: Kelvin Equation at Molecular Scale*, *Physical Review X* **8** (2018) 41046.

[119] T. E. Graedel, *Corrosion Mechanisms for Silver Exposed to the Atmosphere*, *Journal of The Electrochemical Society* **139** (1992) 1963.

[120] S. An, K. Lee, G. Moon, W. Bak, G. Kim and W. Jhe, *Enhanced formation of a confined nano-water meniscus using a 780 nm laser with a quartz tuning fork-atomic force microscope*, *Journal of nanoscience and nanotechnology* **12** (2012) 5754.

[121] D. E. Aspnes and A. A. Studna, *Dielectric functions and optical parameters of Si, Ge, GaP, GaAs, GaSb, InP, InAs, and InSb from 1.5 to 6.0 eV*, *Physical Review B* **27** (1983) 985.

[122] P. B. Johnson and R. W. Christy, *Optical Constants of the Noble Metals*, *Physical Review B* **6** (1972) 4370.

[123] I. H. Malitson, *Interspecimen Comparison of the Refractive Index of Fused Silica*, *Journal of the Optical society of America* **55** (1965) 1205.

[124] T. E. Acosta-Maeda, A. K. Misra, J. N. Porter, D. E. Bates and S. K. Sharma, *Remote Raman Efficiencies and Cross-Sections of Organic and Inorganic Chemicals*, *Applied Spectroscopy* **71** (2017) 1025.

[125] J. Szczerbiński, L. Gyr, J. Kaeslin and R. Zenobi, *Plasmon-Driven Photocatalysis Leads to Products Known from E-beam and X-ray-Induced Surface Chemistry*, *Nano Letters* **18** (2018) 6740.

[126] S. Cerveny, F. Mallamace, J. Swenson, M. Vogel and L. Xu, *Confined Water as Model of Supercooled Water*, *Chemical Reviews* **116** (2016) 7608.

[127] G. E. Walrafen, M. R. Fisher, M. S. Hokmabadi and W. H. Yang, *Temperature dependence of the low- and high-frequency Raman scattering from liquid water*, *The Journal of Chemical Physics* **85** (1986) 6970.

[128] K. Furić and V. Volovšek, *Water ice at low temperatures and pressures: New Raman results*, *Journal of Molecular Structure* **976** (2010) 174.

[129] Y. Yoshimura, S. T. Stewart, M. Somayazulu, H. K. Mao and R. J. Hemley, *High-pressure x-ray diffraction and Raman spectroscopy of ice VIII*, *Journal of Chemical Physics* **124** (2006) 024502.

[130] K. R. Hirsch and W. B. Holzapfel, *Effect of high pressure on the Raman spectra of ice VIII and evidence for ice X*, *The Journal of Chemical Physics* **84** (1985) 2771.

[131] A. Tlili, D. C. Smith, J.-M. Beny and H. Boyer, *A Raman microprobe study of natural micas*, *Mineralogical Magazine* **53** (1989) 165.

[132] B. Minceva-Sukarova, W. F. Sherman and G. R. Wilkinson, *The Raman spectra of ice (Ih, II, III, V, VI and IX) as functions of pressure and temperature*, *Journal of Physics C: Solid State Physics* **17** (1984) 5833.

[133] Y. Yoshimura, S. T. Stewart, M. Somayazulu, H. K. Mao and R. J. Hemley, *Convergent raman features in high density amorphous ice, ice VII, and ice VIII under pressure*, *Journal of Physical Chemistry B* **115** (2011) 3756.

[134] M. J. Taylor and E. Whalley, *Raman spectra of ices Ih, Ic, II, III, and V*, *The Journal of Chemical Physics* **40** (1964) 1660.

[135] B. Minceva-Sukrova, W. F. Sherman and G. R. Wilkinson, *A High Pressure Spectroscopic study on the ice III - ice IX, disordered - ordered transition*, *Journal of Molecular Structure* **115** (1984) 137.

[136] C. G. Salzmann, I. Kohl, T. Loerting, E. Mayer and A. Hallbrucker, *Raman spectroscopic study on hydrogen bonding in recovered ice IV*, *Journal of Physical Chemistry B* **107** (2003) 2802.

[137] G. E. Walrafen, M. Abebe, F. A. Mauer, S. Block, G. J. Piermarini and R. Munro, *Raman and x-ray investigations of ice VII to 36.0 GPa*, *The Journal of Chemical Physics* **77** (1982) 2166.

[138] G. W. Lee, W. J. Evans and C. S. Yoo, *Crystallization of water in a dynamic diamond-anvil cell: Evidence for ice VII-like local order in supercompressed water*, *Physical Review B* **74** (2006) 134112.

[139] T. Shigenari and K. Abe, *Vibrational modes of hydrogens in the proton ordered phase XI of ice: Raman spectra above 400 cm -1*, *Journal of Chemical Physics* **136** (2012) 174504.

[140] C. G. Salzmann, A. Hallbrucker, J. L. Finney and E. Mayer, *Raman spectroscopic features of hydrogen-ordering in ice XII*, *Chemical Physics Letters* **429** (2006) 469.

[141] C. G. Salzmann, A. Hallbrucker, J. L. Finney and E. Mayer, *Raman spectroscopic study of hydrogen ordered ice XIII and of its reversible phase transition to disordered ice V*, *Physical Chemistry Chemical Physics* **8** (2006) 3088.

[142] T. F. Whale, S. J. Clark, J. L. Finney and C. G. Salzmann, *DFT-assisted interpretation of the Raman spectra of hydrogen-ordered ice XV*, *Journal of Raman Spectroscopy* **44** (2013) 290.

[143] C. C. Pradzynski, R. M. Forck, T. Zeuch, P. Slavíček and U. Buck, *A fully size-resolved perspective on the crystallization of water clusters*, *Science* **337** (2012) 1529.

[144] B. M. Auer and J. L. Skinner, *IR and Raman spectra of liquid water: Theory and interpretation*, *Journal of Chemical Physics* **128** (2008) 224511.

[145] Q. Hu, X. Lü, W. Lu, Y. Chen and H. Liu, *An extensive study on Raman spectra of water from 253 to 753 K at 30 MPa: A new insight into structure of water*, *Journal of Molecular Spectroscopy* **292** (2013) 23.

[146] V. Buch and P. Devlin, *Water in Confining Geometries*. Springer, 2003.

[147] S. Chakraborty, H. Kumar, C. Dasgupta and P. K. Maiti, *Confined Water: Structure, Dynamics, and Thermodynamics*, *Accounts of Chemical Research* **50** (2017) 2139.

[148] B. Kim, Q. Kim, S. Kwon, S. An, K. Lee, M. Lee et al., *Unified Stress Tensor of the Hydration Water Layer*, *Physical Review Letters* **111** (2013) 246102.

[149] L. Xu, A. Lio, J. Hu, D. F. Ogletree and M. Salmeron, *Wetting and capillary phenomena of water on mica*, *Journal of Physical Chemistry B* **102** (1998) 540.

초록

컨파인드 상태에서는 자유도가 감소하기 때문에 컨파인먼트 내부 물질의 표면 에너지와 엔트로피 등이 변화하게 된다. 물도 예외는 아니며 컨파인드 물의 탄성 계수, 마찰 계수, 점성, 유전 상수 등과 같은 거시적 성질들이 벌크 물과 비교하여 달라진다고 알려져있다. 물은 수소결합 네트워크를 가지고 있고 물이 가지는 특이한 성질들은 대부분 수소결합과 밀접한 관련이 있다. 따라서 컨파인드 물의 성질변화 또한 수소결합 네트워크 변화와 아주 밀접한 관련이 있을것으로 생각되었고 여러 시뮬레이션과 분광 실험에서도 컨파인드 물이 특이한 수소결합 구조를 가지고 있다는 것을 확인 할 수 있었다. 그러나 시뮬레이션 결과에서 관측한 특이한 수소결합 구조들은 실험적으로 검증되지 않았다. 또한 분광실험에서는 충분히 작은 크기의 컨파인드를 구현하기 어려웠으며 그 결과를 거시적 성질과 동시에 측정시킬 수 없었다. 한편 컨파인드 물의 거시적 성질 변화를 측정하는 실험들은 주로 원자 힘 현미경(Atomic force microscopy) 혹은 표면 힘 측정기(Surface Force Apparatus)를 이용하여 진행되었는데 이러한 힘 측정 장비들에서는 수소결합 네트워크를 측정할 수 없었다.

우리는 컨파인드 물의 수소결합과 그 기계적 특성을 동시에 측정하기 위하여, 수정진동자 기반의 원자 힘 현미경과 공초점 라만 분광장비를 결합하여 팁-증강 라만 분광 장비를 자체 제작하였다. 일반적인 라만분광의 효율로는 약 3000개 미만의 적은 수의 물 분자들의 수소결합을 측정할 수 없기 때문에 금속 팁의 끝에서 국부 전기장의 세기가 증폭되는 팁-증강 라만 분광장비가 필요하였다. 팁도 자체 제작을 하였으며 E-beam evaporation, Sputter coating을 통해 은(Ag)을 코팅하거나 은 와이어를 에칭하여 제작하였다. 팁과 바닥 표면사이에 모세관 응축을 통해 나노

물 기둥을 형성하였으며 팁과 바닥 표면사이의 거리를 조절함으로서 컨파인먼트 정도를 조절하며 라만 신호를 측정 하였다. 그 결과 약한 컨파인먼트 조건에서는 컨파인드 물이 과냉각수 처럼 행동하였으며 강한 컨파인먼트 조건에서는 수소결합 구조가 상온 고압 얼음인 아이스 VII과 유사한 구조를 가진다는 것을 알 수 있었다. 또한 같은 시스템에서 측정한 기계적 이완 시간은 라만신호와 상관관계를 보였으며 강한 컨파인먼트 조건에서 증가하는 양상을 보였다. 이는 컨파인먼트가 강해질 때 내부에 위치한 시료의 고체성이 증가했음을 의미한다. 이러한 점을 통해 강한 컨파인먼트 조건은 표면으로 부터 약 2 나노미터이하의 영역으로 정의할 수 있었다.

물은 지구환경 및 생명활동에서 중요한 역할을 하는 액체이다. 또한 많은 경우에 나노미터 수준으로 갇혀있는 물 환경에서 생명반응이 일어나거나 컨파인드 물의 매개하에 대기 미세입자 들이 형성된다. 따라서 본 연구에서는 컨파인드 물의 성질, 그 중에서도 물의 가장 독특하고 중요한 성질인 수소결합 성질에 대한 연구를 진행하였다. 이 연구 결과는 컨파인드 물이 가지는 여러 독특한 성질들의 기원을 수소결합적인 측면에서 설명할수 있을 것이며, 현재까지는 시뮬레이션 연구 분야였던 초기 얼음핵 구조 연구에 실험적인 증거를 제공한다.

주요어: 팁-증강 라만 분광, 라만 분광, 원자 힘 현미경, 물, 수소결합, 아이스 VII, 컨파인먼트, 상전이

학번: 2014-21349

Acknowledgement

Firstly, I would like to show my gratitude to my supervisor, Prof. Wonho Jhe, for guiding me throughout my Ph.D. course. I appreciate him for his support for my research, insightful comments, meaningful discussions, and help to finish my Ph.D. study.

I also want to show my gratitude to Dr. Sungjin Chang, who introduced me to tip-enhanced Raman spectroscopy. I would not possible to start my research without his help. And I would like to show my gratitude to Prof. Sangmin An and Prof. Dongha Shin for their great help. They generously gave me advice whenever I have stuck during my research, especially Prof. Dongha Shin who teach me a lot of his knowledge about chemistry.

I am also grateful to my seniors and juniors in the Jhelab. Especially to Donghyun Won, who taught me the experimental basics as my mentor in the early days of my Ph.D. course, and to Dr. Qhwan Kim, who gave me a fresh perspective. And I am grateful to Prof. Manhee Lee, Dr. Bongsu Kim, Dr. Soyoung Kwon, Dr. Jongwoo Kim, and Soyoung Shin for their help.

I sincerely appreciate all my colleagues, Dr. Dohyun Kim for numerous

discussions and encouragements, Chungman Kim, Honggi Jeon, Juliana Park, Jaewon Shim, and Sunghoon Hong. I was able to stand during difficult times due to their help. Especially, thanks to Sunghoon Hong for all his effort in making metal coating samples. And also thanks to Joonhyuk Ko, Hansol Song, Sunghoon Kim, Hoyoung Seo, Chanyoung Oh, Hankyul Ko, and Sungwoo Hong.

Special thanks to Dr. Jiyeah Rhie for her help in preparing the thesis defense.

And lastly, I would like to thank my parents and older brother for always supporting me.

Publication list

The contents and figures in this dissertation were published and submitted to the following journals.

1. **Hwang, J.**, Shin, D., Lee, M., Deveney, B. T., Zhang, X., & Jhe, W. Origin of ice nucleation: A quantified nano-confinement study at room temperature (2022) *Science* - Under review

2. Kim, D., Kim, J., **Hwang, J.**, Shin, D., An, S., & Jhe, W. Direct measurement of curvature-dependent surface tension of an alcohol nanomeniscus. *Nanoscale*, 13(14), 6991–6996 (2021).

3. Shin, D., **Hwang, J.**, & Jhe, W. Ice-VII-like molecular structure of ambient water nanomeniscus. *Nature Communications*, 10(1), 286 (2019).

4. Lee, M., **Hwang, J.**, Kim, B., An, S., & Jhe, W. Fluid-induced resonances in vibrational and Brownian dynamics of a shear oscillator. *Current Applied Physics*, 16(11), 1459–1463 (2016).

5. Lee, W., Kim, J., **Hwang, J.**, Noh, H., & Jhe, W. Scaling of thermal hysteretic behavior in a parametrically modulated cold atomic system. *Physical Review E*, 94(3), 1–5 (2016).

6. Lee, M., Kim, B., Kim, Qh., **Hwang, J.**, An, S., & Jhe, W. Viscometry of single nanoliter-volume droplets using dynamic force spectroscopy. *Phys. Chem. Chem. Phys.*, 18(39), 27684–27690 (2016).

7. Lee, M., **Hwang, J.**, Jahng, J., Kim, Qh., Noh, H., An, S., & Jhe, W. Electrical tuning of mechanical characteristics in qPlus sensor: Active Q and resonance frequency control. *Journal of Applied Physics*, 120(7), 074503 (2016).